

## ABSTRACT

Title of Document: CONCENTRATION ENHANCEMENT AND  
DEVICE FABRICATION FOR THE  
IMPROVED PERFORMANCE OF GRADIENT  
ELUTION MOVING BOUNDARY  
ELECTROPHORESIS

Alison A. Sikorsky, Doctor of Philosophy, 2014

Directed By: Professor John T. Fourkas  
Department of Chemistry and Biochemistry

Many recent efforts in the field of microfluidics have been focused on reducing the size and the complexity of devices and on simplifying the methods of analysis performed with them. Gradient elution moving boundary electrophoresis (GEMBE) is a recently described counterflow electrophoresis method that was developed to simplify the analysis of ions in complex matrices. In this thesis, the improvement of the limit of detection of GEMBE and reduction of the GEMBE channel length is investigated.

Integration of simple and robust device components required for the successful adaptation of many analytical methods to multiplexed and field-portable devices often has negative effects on detection sensitivity, such as in the optical detection components in a capillary electrophoresis (CE) system. One of the simplest methods to improve sensitivity in the CE field is known as sample stacking. This method involves preparing the sample in a buffer with a different concentration (and conductivity) than that of the run buffer, such that when an

electric field is applied the analyte concentration is increased at the boundary between the two different buffer concentrations. A method in which the sample is prepared in a buffer at a lower concentration than the run buffer has been implemented. This method achieves a significantly greater signal enhancement than expected for sample stacking. The concentration enhancement ability of this method is demonstrated utilizing GEMBE with channel current detection.

Current GEMBE device construction methods impose limitations on the minimum length of the separation channel. One technique well suited for minimizing the size of the GEMBE separation channel is multiphoton absorption polymerization (MAP). Because MAP is a non-linear optical fabrication method, polymerization is limited to a small region near the focal point of a laser beam. As a result, three-dimensional structures with small feature sizes can be easily created. The 3D capabilities of MAP have been exploited to create channels with circular cross sections and  $\sim 300\ \mu\text{m}$  lengths for GEMBE. The integration of device components fabricated with MAP and molded with PMDS allows visualization of the GEMBE separations, and provides insights into the effect of channel length on GEMBE step width.

CONCENTRATION ENHANCEMENT AND DEVICE FABRICATION FOR THE  
IMPROVED PERFORMANCE OF GRADIENT ELUTION MOVING  
BOUNDARY ELECTROPHORESIS

By

Alison A. Sikorsky

Dissertation submitted to the Faculty of the Graduate School of the  
University of Maryland, College Park, in partial fulfillment  
of the requirements for the degree of  
Doctor of Philosophy  
2014

Advisory Committee:  
Professor John T. Fourkas, Chair  
Professor Don DeVoe  
Professor Sangbok Lee  
Professor Zhihong Nie  
Dr. David Ross

© Copyright by  
Alison A. Sikorsky  
2014

## Acknowledgements

I would like to thank my family for their continuing support and encouragement throughout my academic career, and especially during the ups and downs of graduate school and of life in a new city. I would also like to thank my friends, old and new, for listening to my commentary about being a chemist, and for understanding the unpredictability of research.

I thank my advisor, Professor John Fourkas who has been a seemingly endless source of ideas, suggestions, and encouraging words. I would also like to thank my advisor at NIST, Dr. David Ross, who has also been a source of guidance and encouragement throughout the past few years.

Lastly, I would like to thank all of the members of the Fourkas research group, and all of the researchers who I have had the pleasure of working with at NIST. I would especially like to thank postdoctoral researchers from the Fourkas group, Dr. George Kumi, Dr. Farah Dawood, and Dr. Carlos Toro who were an integral part of my graduate education as post-docs and as friends.

# Table of Contents

Acknowledgements.....	ii
Table of Contents.....	iii
List of Figures.....	vi
Chapter 1: Microfluidics background.....	1
1.1 Introduction.....	1
1.2 Microfluidics.....	1
1.3 Gradient elution moving boundary electrophoresis (GEMBE).....	5
1.4 Concentration enhancement: stacking and focusing methods.....	9
1.5 Reducing separation channel dimensions for GEMBE.....	13
1.6 Conclusion.....	15
Chapter 2: GEMBE: method, device, and data analysis.....	16
2.1 Introduction.....	16
2.2 Materials and methods.....	16
2.2.1 Chemicals and reagents.....	16
2.2.2 GEMBE device assembly.....	17
2.2.3 Device preparation and data collection.....	19
2.2.4 Data analysis.....	21
2.3 Optimization of separation parameters.....	21
2.4 Conclusion.....	28
Chapter 3: GEMBE with concentration enhancement.....	29
3.1 Introduction.....	29

3.2 Experimental.....	29
3.2.1 Analyte system.....	29
3.2.2 Chemicals and reagents.....	30
3.2.3 Procedures and analysis.....	30
3.3 Results.....	32
3.4 Discussion.....	41
3.5 Conclusion.....	45
Chapter 4: MAP fabrication of structures with circular cross-sections.....	46
4.1 Introduction.....	46
4.2 Multiphoton absorption (MPA).....	46
4.3 Multiphoton absorption polymerization (MAP).....	48
4.3.1 Photoresist: composition and preparation.....	49
4.3.2 Sample preparation.....	52
4.3.3 Experimental set-up and fabrication.....	54
4.3.4 Laser table and optics.....	57
4.4 Microfluidic devices: fabrication and molding.....	59
4.5 Conclusion.....	67
Chapter 5: MAP-fabrication of GEMBE devices.....	68
5.1 Introduction.....	68
5.2 Experimental.....	68
5.2.1 Chemicals and reagents.....	68
5.2.2 Device fabrication and set-up.....	69
5.2.3 Device assembly and data collection.....	74

5.3 Results and discussion .....	77
5.4 Conclusion .....	83
Chapter 6: Conclusions and future work .....	84
6.1 Conclusions.....	84
6.2 Future work.....	85
6.2.1 Fluorescence studies .....	85
6.2.2 PDMS composite .....	85
6.2.3 Molding material.....	86
Appendices.....	87
References.....	141

## List of Figures

1.1 Laminar flow illustration	7
1.2 Poiseuille flow	8
1.3 Gradient elution moving boundary electrophoresis schematic	11
1.4 Thermoplastic GEMBE device	12
1.5 GEMBE circuit	14
2.1 GEMBE device diagram	21
2.2 GEMBE separation with air bubble interference	24
2.3 GEMBE separation: two analytes	26
2.4 GEMBE separation: three analytes	27
2.5 GEMBE of low conductivity samples	28
2.6 GEMBE run buffer composition	30
3.1 GEMBE limit of detection for samples prepared in run buffer	36
3.2 GEMBE limit of detection for samples diluted with DI water	38
3.3 Conductivity versus run buffer concentration	39
3.4 FACSI-GEMBE for samples diluted with DI water	40
3.5 FACSI-GEMBE for samples diluted with tap water	42
3.6 FACSI-GEMBE step height versus pressure hold time	44
4.1 Simplified Jablonski diagram	50
4.2 Single photon and two photon absorption	51
4.3 MAP-fabricated structures	52
4.4 Lucirin TPO-L photoinitiator	53
4.5 Components of a negative-tone photoresist	55
4.6 Sample preparation for MAP fabrication	56
4.7 Radical polymerization	57
4.8 Inverted microscope orientation	58
4.9 Upright microscope orientation	59
4.10 Inverted microscope beam path	61
4.11 Upright microscope beam path	62
4.12 Molding a MAP master structure	64
4.13 MAP-fabricated master structures for molding microfluidic devices	66
4.14 MAP-fabricated master structures	67
4.15 Assembly of a microfluidic device from a PDMS mold	69
5.1 GEMBE master structures	73
5.2 PDMS GEMBE device	74
5.3 PDMS molds of MAP-fabricated structures	76
5.4 MAP-fabricated circular structures	77
5.5 T-shaped PDMS-GEMBE orientation	78
5.6 Separations in a PDMS-GEMBE device	81
5.7 step width in a PDMS-GEMBE device	83
5.8 Optical images of a PDMS-GEMBE device during filling	84
5.9 Fluorescence images of a separation in a PDMS-GEMBE device	85

# Chapter 1: Microfluidics background

## 1.1 Introduction

This Chapter introduces the concepts that are integral to the work contained in the following chapters. Where appropriate, a more in-depth discussion of particular topics is reserved for individual Chapters.

## 1.2 Microfluidics

Since their introduction in the 1980s, microfluidic devices have been used to perform a wide variety of functions including chemical analyses, chemical reactions, and material syntheses.<sup>1-5</sup> Microfluidic devices are of micrometer size in one or more dimensions and, as a result, typically involve sample, analysis, and waste volumes that are a few milliliters at most. Many applications of microfluidics take advantage of this small volume requirement to limit the use of expensive and/or hazardous reagents and to minimize the production of similarly hazardous waste. Another well-known benefit of the small volumes involved in performing analyses with microfluidic devices is the behavior of fluids when they are confined to micron-sized channels.

For pressure driven flow in microfluidics, the flow is often characterized using the Reynolds number (Equation 1.1) and the Poiseuille equation (Figure 1.2). The Reynolds number ( $R_e$ ) is defined in equation 1, where  $\rho_m$  is density,  $\eta$  is viscosity,  $L$  is a characteristic dimension for the channel, and  $U$  is a characteristic velocity of the flow.

$$R_e = \frac{\rho_m LU}{\eta} \quad \text{Equation 1.1}$$

The Reynolds number is a dimensionless value that compares the relative importance of inertial forces to viscous forces. When  $R_e$  is less than 1000, the fluid flow is described as laminar. Fluid described as “laminar” flows in streamlines with fluid flowing in layers parallel to the channel walls. In most microfluidic examples  $R_e$  is much less than one, so viscous forces dominate and the flow is laminar. In contrast,  $R_e$  is large in macroscopic systems and the flow of fluid is turbulent with complex mixing. The advantages, and in some applications disadvantages, of laminar flow in microfluidic devices have been widely investigated.<sup>6,7</sup> One advantage can be demonstrated by the ability to introduce two fluids side-by-side without mixing, because mixing in the laminar flow regime is limited to diffusion that occurs at the fluid-fluid interface (Figure 1.1). In some cases, mixing in microfluidic environments is desired, and various types of valves, motors, and fluid obstacles have been integrated into channels to disrupt laminar flow.<sup>8-11</sup>

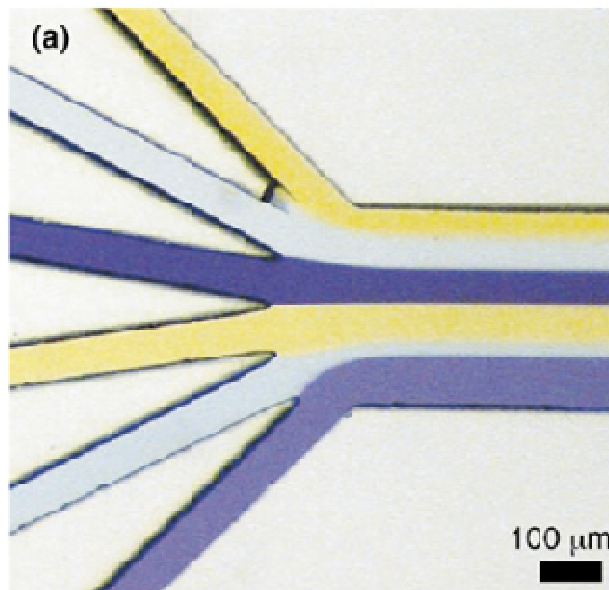
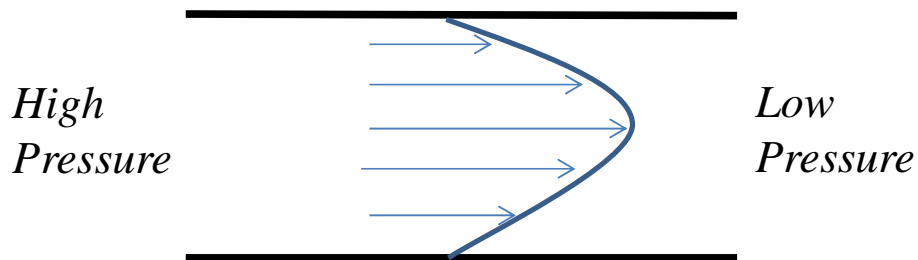


**Figure 1.1:** The three different colored fluids are introduced from isolated channels into one larger channel, but remain separated because the fluid flow is laminar.<sup>11</sup>

Another consequence of the dimensions of microfluidic devices is the flow profile that results from a pressure-driven flow. Such a flow is called Poiseuille flow and is described in Figure 1.2. The fluid in direct contact with the walls of the microfluidic channel is assumed to be stationary (no-slip condition) and the lamina (layers of fluid in the laminar flow regime) move at faster velocities closer to the center of the channel.<sup>12,13</sup> The Poiseuille equation (included in Figure 1.2) can be used to calculate the pressure drop across a channel. In Figure 1.2, a high pressure is applied on the left side of the microfluidic channel to cause the fluid to flow to the right side of the channel.



$$\Delta P = \frac{8\mu LQ}{\pi r^4}$$

**Figure 1.2:** In the case of a pressure driven flow in microfluidic channels, the parabolic flow profile that results is called Poiseuille flow. The characteristic flow profile is a result of the non-uniform velocity of lamina. The Poiseuille equation can be used to calculate the pressure drop across a channel, where  $\Delta P$  is the pressure drop,  $\mu$  is the dynamic viscosity of the fluid,  $L$  is the channel length,  $Q$  is the volumetric flow rate,  $\pi$  is the mathematical constant, and  $r$  is the channel radius.

The Poiseuille equation represents the pressure drop across a channel ( $\Delta P$ ) as it is related to the viscosity ( $\mu$ ), channel length ( $L$ ), volumetric flow rate ( $Q$ ), and channel radius ( $r$ ). This equation is often used to determine experimental parameters for channels of varying dimensions. In many microfluidic separation methods, pressure-driven flow is used to move focused analyte bands to a detection point. Poiseuille flow is important in these systems because the size of the analyte band increases as the velocity difference between lamina increases which can result in a decreased signal.

Some of the most common analysis methods performed with microfluidic devices rely on laminar flow, pressure driven flow, and electrokinetic phenomena such as electroosmosis, electrophoresis, and dielectrophoresis. Electrophoresis is one of the most well known of the electrokinetic separation methods. This method achieves separation by using an electric field to control the velocity of charged molecules. The relationship between the velocity of a charged molecule and the electric field is shown in equation 1.2. The velocity of an analyte ( $v_{ep}$ ) in an electric field depends on the magnitude of the electric field ( $E$ ) and the electrophoretic mobility of the analyte ( $\mu_{ep}$ ). Electrophoretic mobility is determined by the charge and drag of a molecule.

$$v_{ep} = \mu_{ep}E \qquad \text{Equation 1.2}$$

When an electric field is applied, molecules with non-zero charges will migrate in the electric field with a velocity proportional to the electric field strength (in the absence of other forces). Molecules with a larger mobility will migrate faster than molecules with a smaller mobility. The velocity difference that results from differences in electrophoretic mobilities is widely used to separate molecules.

Capillary electrophoresis (CE) is one of the most popular electrophoretic separation methods because of its ability to enable fast, high resolution separations of a variety of analytes, including proteins, DNA, and inorganic ions.<sup>14-17</sup> Many methods of separation have been developed to improve further upon the capabilities of CE. One such technique is capillary zone electrophoresis (CZE), in which sample is typically injected into a capillary as a discrete zone or plug. A voltage is applied across the capillary containing the sample plug (or zone) and analytes are separated, based on their electrophoretic mobilities, and then detected. In CZE, the buffer composition is chosen such that analytes of interest maintain a charge and can be resolved. Other variants of CE, such as capillary isotachopheresis and capillary isoelectric focusing, involve adjusting the buffer composition

(mobility and pH) to improve separation performance. Although these techniques have been successfully applied to the detection of analytes such as small ions, DNA, and proteins, new methods of separation are being developed to decrease the complexity of the analysis methods and of the microfluidic devices.

### 1.3 Gradient elution moving boundary electrophoresis (GEMBE)

The development of electrophoresis devices that are smaller and simpler than the variety of CE derivatives available<sup>1,18,19</sup> has motivated the introduction of many recently described electrophoresis methods. Gradient elution moving boundary electrophoresis (GEMBE), which was developed by Shackman *et al.* in 2007, is one such method.<sup>20</sup> GEMBE is a counterflow electrophoresis method that is ideally suited for the separation and detection of charged molecules in a complex sample matrix such as blood serum or well water. In GEMBE, separation is achieved by applying a counter-flow through the separation capillary (by applying pressure to the run buffer reservoir) that opposes the electrophoretic velocity of charged analytes, thus controlling the entrance of the analytes into the detection capillary. To date, GEMBE has been demonstrated with optical detection,<sup>20</sup> channel current detection,<sup>21,22</sup> and capacitively coupled contactless conductivity detection.<sup>23-25</sup> Details of GEMBE coupled to each of the three detection methods are described in this section. A variety of separation channel lengths have also been employed, from a few millimeters to a few centimeters. Although the detection method and separation channel length have been varied, the basic principles of GEMBE remain the same.

GEMBE is a counter-flow electrophoresis technique that operates under variable pressure and constant voltage (Figure 1.3). A constant voltage is applied at the buffer reservoir to cause analytes to migrate electrophoretically from the sample into the capillary. The counter-flow is a combination

of electroosmotic flow and pressure-driven flow. Initially, the pressure applied to the head space of the buffer reservoir is high so that no analytes enter the capillary (Figure 1.3A). The pressure is then decreased over time. As the pressure is decreased and the electrophoretic velocity of an analyte becomes greater than the counter-flow velocity, the boundary of that analyte will begin to move into the separation capillary (Figure 1.3B), where it is detected as a stepwise increase or decrease in the detector response. As a result, only analytes that have electrophoretic velocities that are greater than the applied pressure are allowed to enter the detection capillary.

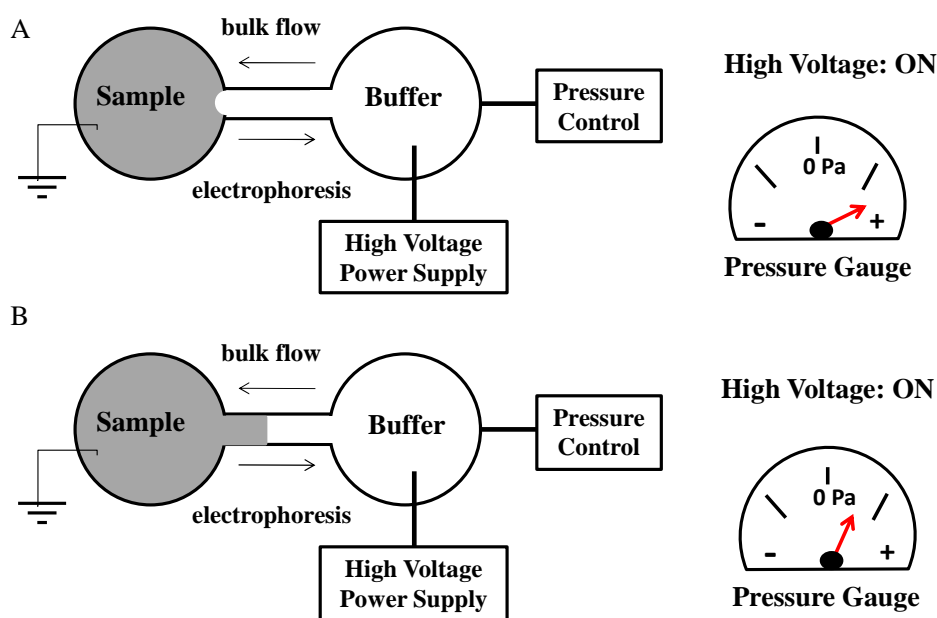


**Figure 1.3:** Schematic of the GEMBE separation mechanism. (A) Initially, the pressure applied to the head space of the buffer reservoir is high enough that no analytes enter the capillary connecting the two reservoirs. (B) As the pressure is decreased, analytes move into the capillary when their electrophoretic velocity is greater than the counter-flow velocity. Analytes are detected as a stepwise increase or decrease in the detector response in the capillary.

In GEMBE, moving analyte boundaries are transported electrophoretically from the sample through the detection capillary. Detection of a moving boundary relies on the distinction between the presence and the absence of a certain analyte in the separation capillary. The initial demonstration of GEMBE used optical detection to detect fluorescent dyes and fluorescein-labeled, single-stranded

DNA.<sup>20</sup> Optical detection was performed by Shackman *et al.* in a silica capillary device as well as in a thermoplastic microfluidic device. Each of the devices was mounted on a microscope and the fluorescence of the solution inside of the channel was monitored. The thermoplastic device is shown in Figure 1.4. Here, the central hole acts as the buffer reservoir for all 8 surrounding sample reservoirs. With this device design, the authors minimized the number of access ports to decrease the device footprint, and could perform 8 analyses simultaneously. The analytes, fluorescein and 6-carboxy-fluorescein, were optically detected as they were driven electrophoretically from the outer sample reservoir to the inner run-buffer reservoir.

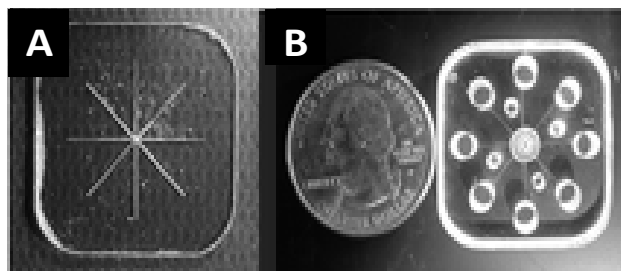


**Figure 1.4:** Thermoplastic microfluidic device used for GEMBE with optical detection of fluorescent analytes. (A) Thermoplastic device before and (B) after reservoirs and screw holes for immobilization were added. The central hole was used as a common buffer reservoir and pressure control port, and the surrounding eight holes were sample reservoirs. Analytes traveled from the outside to the inside of the device when their electrophoretic velocity exceeded the pressure applied at the central buffer reservoir.<sup>20</sup> Detection was performed at a fixed position between the central buffer reservoir and each sample reservoir.

The use of optical detection methods imposes requirements on channel dimensions and on the type of analytes that can be detected. In most cases, channel cross-sections must be large enough to provide a sufficient path length for detection (Beer's law), and analytes must be optically active, or be functionalized with optically active substituents. Methods that eliminate these requirements, such as contactless conductivity detection and channel current detection, have also been demonstrated to work well with GEMBE.<sup>21,22,25</sup> Contactless conductivity detection was demonstrated by Strychalski *et al.* with a 5.5-cm-long separation capillary. The benefits of the counter-flow separation pressure in

GEMBE were highlighted in this work, with the detection of small ions, such as  $\text{Ca}^{2+}$ ,  $\text{Na}^+$ , and  $\text{Mg}^{2+}$ , in samples of whole milk, dirt, leaves, coal fly ash, and blood serum. The high pressure counter-flow excluded large particulates in the various samples, which allowed for analysis with minimal sample preparation. The small ions were detected at micromolar concentrations.

Much shorter (2- to 3-mm) channel lengths were demonstrated when GEMBE was used in conjunction with channel current detection.<sup>21,22</sup> Figure 1.5 shows an electrical circuit diagram depicting the GEMBE separation capillary as a resistor. In the case of channel current detection, when a constant voltage is applied, the current that flows through the capillary is dependent on the concentration of ions in the solution (conductivity) within it. Therefore, the presence or absence of a certain analyte in the separation capillary is monitored by the change in current flowing through the capillary. Generally with channel current detection, the measured step width and resolution are dependent on the channel length.

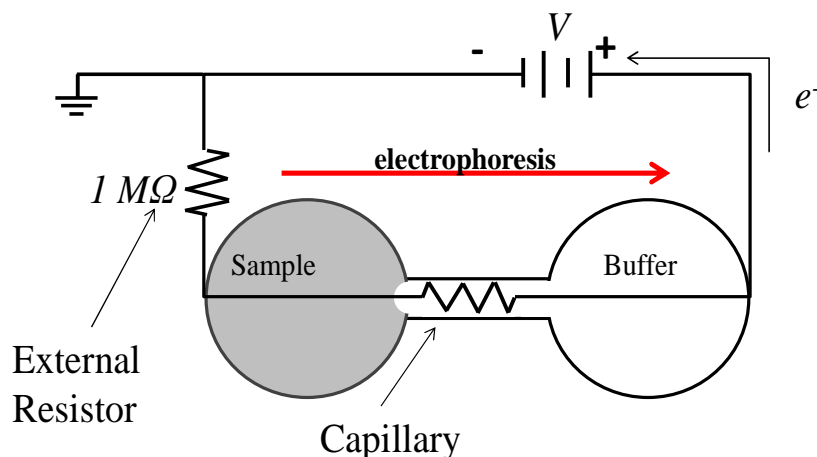


**Figure 1.5:** Equivalent circuit representing GEMBE with channel current detection. The external resistor ( $1\text{ M}\Omega$ ) acts as the detector. Current is applied at the buffer reservoir so that analytes are driven electrophoretically from the sample into the detection capillary. When an analyte enters the detection capillary, the conductivity of the solution inside the detection capillary changes, and a stepwise change in the current is measured. The height of the step corresponds to the concentration of the analyte, and the counter-flow pressure at which it is detected depends on its identity.

Initially, when voltage and high pressure are applied, the moving boundary is stationary at the entrance of the capillary (*i.e.*, at the junction between the sample reservoir and the capillary) so that the current through the capillary is constant. As each analyte boundary moves through (when the pressure is decreased), it changes the conductivity of the solution inside the capillary, which gives rise to a step-wise change in the electrophoresis current. This process is repeated for each boundary so that a series of moving boundaries can be detected. The height of each step is used to determine the concentration of the analyte, and the elution time of each step (or the pressure at which it occurs) is used to determine the identity of the analyte. The magnitude of the change in current, or step height, is directly related to the concentration of analyte in a moving boundary. A boundary with a higher concentration will result in a larger change in current when the boundary enters the capillary. The analysis of anions in water samples using GEMBE with channel current detection is discussed in Chapter 2.

With GEMBE, as with many variants of CE, the use of modes of detection (*i.e.* channel current detection) that eliminate optical components can have a negative impact on the sensitivity of the system. This decrease in sensitivity has motivated work on methods that enhance the analyte concentration before detection. The following section discusses efforts in the CE field to improve detection sensitivity by implementing concentration enhancement methods, and how these efforts relate to the recent development of a concentration enhancement method to improve the LOD of GEMBE with channel current detection.<sup>26</sup>

#### 1.4 Concentration enhancement: stacking and focusing methods

As mentioned above, CE has a number of well-recognized advantages, including small sample and reagent requirements, high selectivity, relatively short analysis times, and applicability to a wide

range of analytical problems. However, among the disadvantages of CE, perhaps the most significant is that it generally provides inferior sensitivity when compared with chromatographic methods such as high-performance liquid chromatography (HPLC). Consequently, improvement of CE sensitivity has been an active area of research since the technique was first introduced.<sup>27-33</sup> Much of this work has been directed toward methods that employ gradients in the electric field to manipulate the velocity of the analytes in such a way that they reach the detection point at a higher concentration than is present in the starting sample. Among the simplest and most commonly used of these methods are the various forms of sample “stacking”. Although this term is often assigned subtly different definitions, here we use the broad definitions used in a series of reviews by Breadmore and co-workers,<sup>28,29,33,34</sup> in which stacking refers to concentration enhancement methods that rely on changes in electrophoretic velocity. In the most commonly used stacking methods, analytes move across a boundary formed between two different solutions. The composition of the solutions is chosen so that the electrophoretic velocity of the analytes is different on either side of the boundary. This difference in velocities is often achieved simply by using two similar buffers prepared at different concentrations (and, therefore, different conductivities). Examples of stacking methods that involve a boundary between buffer solutions of different concentrations include field-amplified sample stacking and field-amplified sample injection.<sup>31,32</sup>

For most stacking methods, when a voltage is applied the analytes migrate at different speeds on either side of the boundary while traveling in the same direction. As they move across the boundary, the analytes slow down and stack up, much like cars approaching a traffic jam. In these types of methods, the maximum degree of concentration enhancement is determined by the ratio of the velocities on either side of the stacking boundary. For conventional stacking methods based

solely on differing buffer concentrations, the improvement in sensitivity is therefore limited by the conductivity ratio of the solutions on either side of the boundary.<sup>35</sup>

A variety of large-volume injection methods have also been described for use with CE, including large-volume sample stacking (LVSS) and large-volume sample stacking with electroosmotic-flow pumping (LVSEP). The sensitivity improvements provided by those methods can often be quite high (100- to 3000-fold sensitivity improvement). However, these methods typically require samples to be injected from very low conductivity solutions, making solid-phase extraction or similar pretreatment methods necessary.<sup>36-39</sup> For example, Zhang and Thormann<sup>39</sup> achieved over 1000-fold sensitivity enhancement with a large-volume sample injection method using samples with conductivity similar to that of bidistilled water (0.2 M $\Omega$ -cm resistivity, 0.005 mS/cm conductivity).

For some types of stacking methods, which are often referred to as “focusing” methods, analytes slow down at the focusing point, and their velocities also change direction (relative to the velocity of the focusing point or boundary if it is not stationary) upon crossing it. Thus, in a focusing method, analytes move toward the focusing point, or boundary, from both directions. The most familiar example of a focusing method is isoelectric focusing (IEF).<sup>40,41</sup> More recent examples include a variety of counter-flow gradient electrofocusing methods<sup>42-46</sup> and the nonlinear focusing of DNA in gel electrophoresis.<sup>47-49</sup>

With all focusing methods, the concentration enhancement is not limited by the conductivity ratio of the solutions used but is instead determined by the steepness of the velocity gradient, the amount of sample injected, and/or by the duration of the applied focusing field. Focusing methods can often achieve greater concentration enhancement than the simplest stacking methods because focusing is not constrained by an upper limit related to the conductivity ratio. However, focusing

methods can be more complex to implement. For example, in the simplest case of CE with field-amplified sample stacking, the only change relative to a nonstacking CE method is that the sample is prepared at a lower buffer concentration than the run buffer used to fill the capillary during the separation.

Consider, for comparison, the various focusing methods described in the reviews by Ivory, Wang et al., and Kelly and Woolley.<sup>44-46</sup> The techniques described therein include the use of semipermeable membranes enclosed in chambers with variable cross-sectional area, microfabricated devices with semipermeable polymer sections, diffusion of buffer ions through dialysis tubing to generate a conductivity gradient, embedding an array of electrodes into the side of an electrophoresis channel, or application of a temperature gradient along the length of the channel. Although these techniques achieve performance (concentration enhancement) far in excess of what is possible with conventional field-amplified sample stacking, it is not without some level of increased complexity. The notable exception to the rule of focusing methods being more complex than simple stacking is the workhorse technique of IEF, which is, for the most part, only applicable with peptides and proteins and only exists in the simple, buy-the-kit-and-follow-the-directions format because of decades of development.<sup>50,51</sup>

Advances in microfluidic chip electrophoresis,<sup>52</sup> and in miniaturization in general, have enabled progress toward both multiplexed and field-portable CE systems.<sup>2,53-57</sup> Both of these applications require a higher degree of reliability than is necessary for a lab-based, single-capillary instrument, and these methods both could therefore benefit from the use of detection approaches that are much simpler and therefore more robust than the optical detection methods (UV absorbance and laser-induced fluorescence) most commonly used with laboratory CE instruments. As mentioned in the previous section, the use of a simpler mode of detection is likely to have a negative impact on the

sensitivity of the system, making the need for good methods of sensitivity enhancement even more pressing.

In Chapter 3, implementation of a stacking method aimed at achieving online concentration enhancement prior to separation with GEMBE with the goal of maintaining a fast, simple analysis is described. The technique is a combination of the simplest electrophoretic system (GEMBE with channel current detection) and the simplest method for sample enrichment (preparation of the sample in a lower concentration buffer with respect to the run buffer). The stacking method discussed in Chapter 3 is termed field amplified continuous sample injection (FACSI). The expectation was that the sensitivity improvement would be less than or equal to the ratio of the buffer conductivities (as with sample stacking in conventional CZE). However, the results show a much larger improvement in sensitivity.

Further improvements on GEMBE were predicted by Ross and Romantseva in 2007 suggesting that reduced channel lengths would provide a minimum separation time due to reduced step width and increased analyte resolution. This work is discussed in the following section, and a method to fabricate devices to test this theoretical prediction is discussed in Chapter 4.

### 1.5 Reducing separation channel dimensions for GEMBE

Aside from the physical benefit of small dimensions of microfluidic devices, the ability to reduce the length of analysis channels can also be used to decrease the amount of time required for detection. Ross *et al.* investigated the effect of shortening GEMBE separation channels on the resulting step width and resolution for a separation.<sup>22</sup> This theoretical work predicts that the ideal channel length to achieve the smallest step width while maintaining resolution between two analytes is about 100 times shorter than the shortest (3-mm) channels demonstrated with GEMBE.

In the 2009 work, the authors considered two limiting cases: very large dispersion where the resolution is independent of acceleration (the controllable separation parameter), and negligible dispersion where the resolution is dependent on the channel length and the acceleration. In general, very large dispersion dominates in short channels (nm to  $\mu\text{m}$ ) and negligible dispersion dominates in longer ( $\mu\text{m}$  to mm) channels. The channels that have been used in GEMBE thus far have been relatively long, (i.e. in the negligible-dispersion regime). The time for a separation can be adjusted by increasing or decreasing the acceleration of the pressure gradient, until the pressure acceleration is too fast, and analytes are no longer resolved.

In GEMBE, the step width is equal to the time it takes for an analyte boundary to traverse the separation channel. As the channel length is decreased, the resolution between two analytes should increase when compared to a separation in a longer channel with the same counter-flow acceleration because each moving boundary will take less time to traverse the channel. The increased resolution and decreased analyte step width should allow separations to be performed at faster accelerations in shorter channels.

With the current method of GEMBE device fabrication, the minimum channel length attainable is 2 to 3 mm. To fabricate shorter channels, a method of fabrication that provides the ability to create circular microchannels that imitate the fused-silica-capillary previously used for GEMBE is ideal. Many currently available lithographic methods require multiple time consuming steps to achieve circular dimensions, if they can be achieved at all. In Chapter 4, a method of fabrication that allows 3-dimensional control of structures and the fabrication structures with circular cross sections, multiphoton absorption polymerization (MAP), is introduced.

## 1.6 Conclusion

To improve GEMBE, the implementation of a simple concentration enhancement method (FACSI) is investigated (Chapter 3) and the length of the separation channel is altered (Chapters 4 and 5). The overarching theme of both of these efforts is to maintain device and method simplicity while decreasing the limit of detection and the analysis time of GEMBE.

## Chapter 2: GEMBE: method, device, and data analysis

### 2.1 Introduction

In the following chapters the optimization of GEMBE, coupled with channel current detection by increasing the concentration of an analyte in a boundary before it enters the detection capillary, will be discussed. This optimization is achieved by employing focusing or stacking mechanisms (Chapter 3) and decreasing the channel length to minimize the analysis time (Chapter 5). This chapter will focus on GEMBE device preparation, data collection and analysis, and separation parameter optimization.

### 2.2 Materials and methods

#### 2.2.1 Chemicals and reagents

All solutions were prepared with deionized (DI) water (18.2-M $\Omega$ ·cm, Barnsted Easypure II ultrapure water system). Stock solutions of 1-mmol/L sodium phosphate, sodium oxalate, and sodium arsenate were prepared from monobasic sodium phosphate (NaH<sub>2</sub>PO<sub>4</sub>, Sigma), dibasic sodium oxalate (Na<sub>2</sub>O<sub>4</sub>C<sub>2</sub>, Sigma), and dibasic sodium arsenate (Na<sub>2</sub>HAsO<sub>4</sub>, Sigma) by dissolving the salts in deionized water or in run buffer. The run buffer was 100-mmol/L in  $\beta$ -alanine (Fluka) and 70-, 80-, or 90-mmol/L in HCl (32%, Fluka) with a pH of 2.6, 3.0, or 3.2 respectively. The solution was sonicated for 15 minutes and degassed before use.

### 2.2.2 GEMBE device assembly

The GEMBE capillary device is assembled as described in publications by Ross *et al.*,<sup>22</sup> and is depicted in Figure 2.1. A 360- $\mu\text{m}$ -diameter hole is drilled through the ends of two female nylon Luer lock caps (McMaster-Carr, Atlanta, GA) and a fused-silica capillary (OD = 360  $\mu\text{m}$ , ID = 5  $\mu\text{m}$ ; Polymicro Technologies, LLC, Phoenix, AZ) is threaded through the holes. The capillary and Luer locks are sealed together with a two-part epoxy (Bondit B-45TH; McMaster-Carr, Atlanta, GA) and cured for 3 hours at 93 °C. Irregular current measurements are observed if the epoxy is instead cured at ambient temperature (typically for 24 to 72 hours). A jeweler's file is used to score the edge of the capillary near the bottom of each Luer lock cap and the excess capillary is removed, resulting in a minimum capillary length of 2- to 3-mm. To store the Luer lock and capillary assembly for subsequent use and to prevent dust and debris from settling at the capillary entrance, the assembly is placed in an empty pipette container. A 3-mL polypropylene syringe serves as the buffer reservoir. The syringe is connected to the capillary device through a manifold, using approximately 15 cm of Tygon tubing (Small Parts, Inc., ID = 1/8 in).

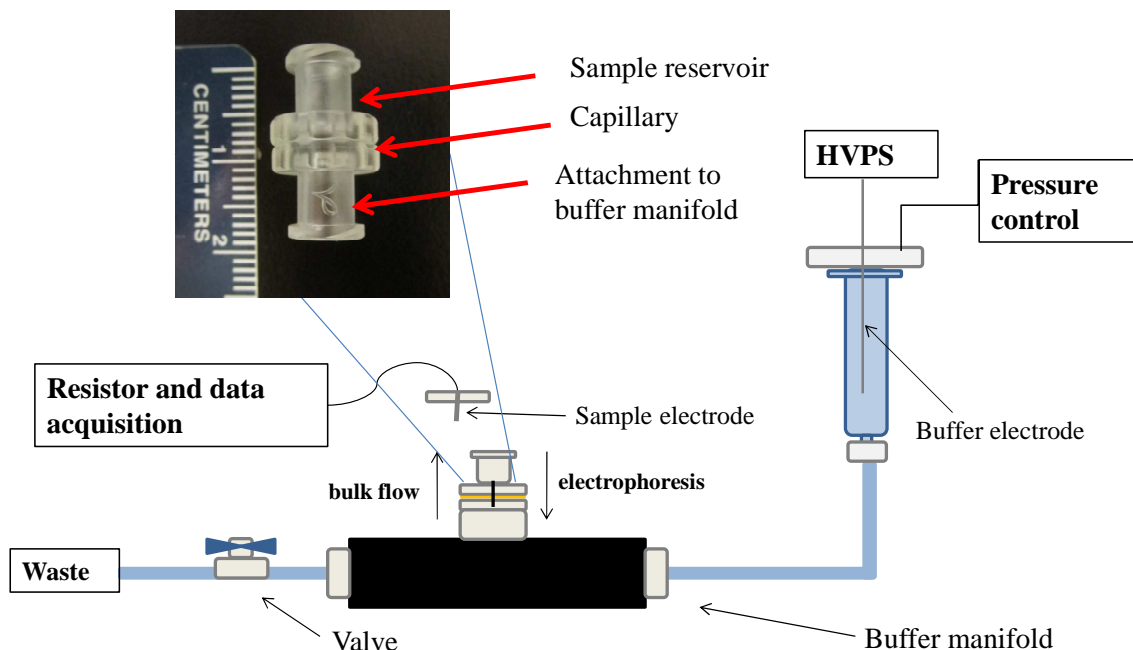


**Figure 2.1:** GEMBE device schematic. The detection capillary is threaded through two 360- $\mu\text{m}$  holes drilled through two female nylon Luer locks and sealed with epoxy (top left). This assembly is screwed into a manifold (black) that allows connection to the buffer reservoir (syringe), where the high voltage and pressure are applied. The Luer lock separation capillary component can be removed and cleaned, or discarded without re-assembling the entire device.

A custom-built plunger attached to tubing connected to the sample reservoir allows access for the pressure control and the high-voltage source (Stanford Research Institute Inc., Model PS350). All electrical connections and electrodes are made from high purity Pt wire (Sigma Aldrich, St. Louis, MO). A precision pressure controller (Series 600, Mensor, San Marcos, TX), with a range of  $\pm 68.900$  kPa, is used to control the applied pressure at the buffer reservoir. The end of one female Luer lock cap is used as the sample reservoir and is loosely covered with a custom-made plastic cap with a Pt electrode to provide the electrophoresis current. Measurement of the current through the capillary is performed with a 1-M $\Omega$  resistor (Mouser Electronics, Inc., Mansfield, TX) connected in series with the capillary and a 16-bit analog-to-digital converter (Model USB-6229, National Instruments). The capillary device, manifold, and resistor are enclosed by a metal box to reduce electrical noise.

### 2.2.3 Device preparation and data collection

The first step in performing a GEMBE separation is to fill the device with run buffer without allowing air bubbles to enter the manifold. Air bubbles can be avoided by filling the run buffer syringe first, while the port for the Luer lock assembly is sealed and the valve to the waste tubing is closed. It is important to prevent air bubbles from entering any part of the device as the fluid or current flow through the detection capillary can be disrupted by the presence of air bubbles. The waste valve is then slowly opened to allow run buffer to fill the tubing and manifold, while run buffer is continuously added to the syringe. After the entire device is filled with run buffer (i.e., when the run buffer exits at the “waste” end of the device), the waste valve is closed and the custom-built plunger is attached to the buffer syringe. Next, the pressure applied at the buffer reservoir is set to 5,000 Pa and the entire assembly is checked for leaks. The most common source of leakage is at edges of tubing that has been stretched or ripped during assembly. A leak due to stretched or ripped tubing can be fixed by cutting off the damaged portion of tubing. Other sources of leakage typically require the replacement of Luer lock connectors or the re-epoxying of joints (which must be done with clean, dry parts).

After the manifold is assembled, filled with run buffer, and checked for leaks, the Luer lock capillary assembly can be attached. To attach the assembly without introducing air bubbles, the pressure that is applied at the buffer reservoir is turned off and the seal is removed from the Luer lock-capillary attachment port. The end of the Luer lock assembly that is attached to the run buffer manifold is first over-filled with run buffer (to prevent the trapping of air bubbles). The sample reservoir (exposed side of the Luer lock assembly) is then filled with run buffer, and the waste valve is opened to flush fresh run buffer through the buffer manifold.

Before a sample can be analyzed, the current signal that is measured across the detection capillary is monitored for 3 to 6 separations over a large pressure range (typically from 40,000 Pa to 5,000 Pa for the analytes discussed here) at a pressure ramp rate of -25 Pa/s to -50 Pa/s. Signal monitoring is performed to check for the presence of air bubbles in the device, to check for contaminants or unknown species in the run buffer, and to collect a baseline to compare with separations that contain a given analyte. Figure 2.2 shows a run buffer separation in the presence of air bubbles in the device. If air bubbles are present in the initial run buffer separations, the device can be flushed by opening the waste valve, the Luer-lock capillary assembly can be removed and re-attached or replaced, or the entire GEMBE set-up can be disassembled, rinsed, dried, and re-assembled.

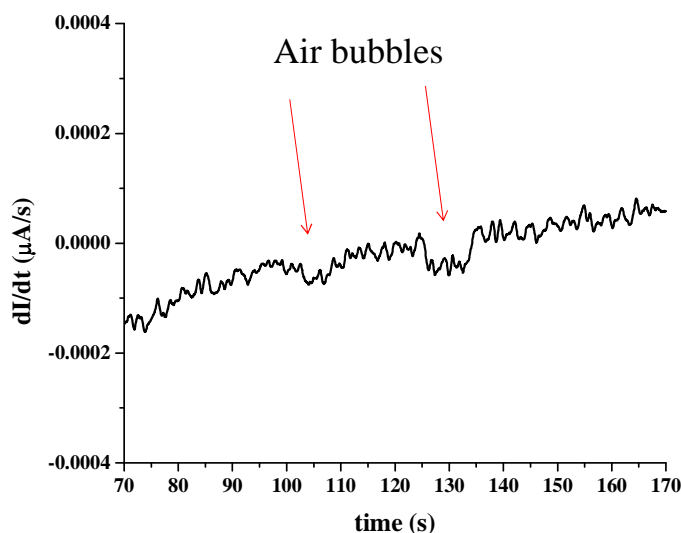


**Figure 2.2:** A typical GEMBE run buffer separation that indicates the presence of air bubbles in the device. Red arrows identify the area in the baseline where an air bubble is present.

To run a GEMBE separation, the starting pressure, pressure ramp rate, number of pressure steps, and voltage are entered into the front panel of a LabView program. A labeled screenshot of the front panel of this program is included in the Appendix (A.1). The starting pressure is chosen to

provide a sufficient baseline (typically 10 to 30 seconds) before an analyte is detected. The pressure ramp rate is determined by the pressure step size and the duration of each pressure step. For a typical separation, the pressure step size was -100 Pa with step duration of 2 s, which corresponds to a pressure ramp rate of -50 Pa/s. The separations discussed below were performed at an average start pressure of 38,000 Pa with 200 pressure steps, a ramp rate of -50 Pa/s, at a voltage of 1,000 V. Separations are monitored in real time with LabView with a plot of signal amplitude, allowing separation parameters to be optimized during a series of separations.

#### 2.2.4 Data analysis

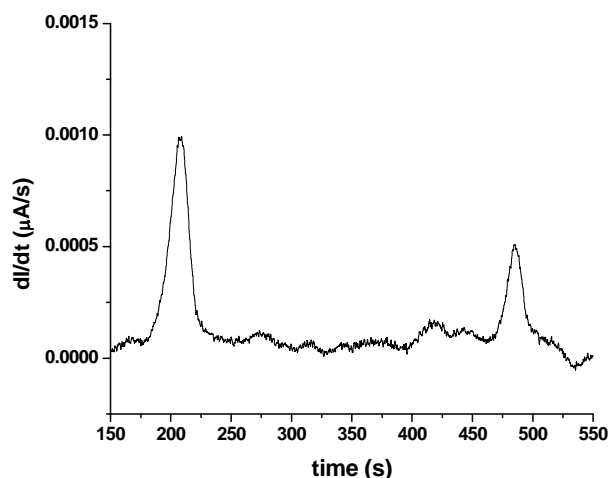
The data that are collected with LabView are imported into Origin 7.5 for further analysis. The current derivative is plotted as a function of time using a 51-point Savitzky-Golay derivative<sup>58</sup> and adjacent averaging smoothing. The extent of data smoothing is determined for each series of separations, so that noise is reduced without compromising signal integrity. A typical separation is plotted with 300-point adjacent averaging. For the data discussed in this document, the signal amplitude is multiplied by negative one to produce a plot that resembles a conventional electropherogram. Mathematica is used to determine step width, step height, resolution, and limit of detection (LOD). A representative Mathematica worksheet is included in the Appendix (A.2).

#### 2.3 Optimization of separation parameters

With the goal of eventually applying GEMBE to the analysis of environmental water samples, GEMBE separation parameters were investigated using a model system of dihydrogen phosphate ( $\text{H}_2\text{PO}_4^-$ ), which is commonly found in natural water samples, and hydrogen oxalate ( $\text{HO}_4\text{C}_2^-$ ), which is found in many common foods. This model system was chosen to determine separation parameters that could be applied to the separation of  $\text{H}_2\text{PO}_4^-$  and dihydrogen arsenate ( $\text{H}_2\text{AsO}_4^-$ ) in water, while

minimizing the use of toxic arsenic-containing samples. The GEMBE limit of detection of arsenate is of interest because it can co-elute with phosphate<sup>59,60</sup> and is toxic if ingested even at low concentrations (10 ppb).<sup>61</sup> Based on the pK<sub>a</sub>s for phosphoric acid and oxalic acid (Figure 2.3) a 100-mM β-alanine, 80-mM hydrochloric acid (HCl) run buffer (pH = 3.0) was chosen to allow the separation of H<sub>2</sub>PO<sub>4</sub><sup>-</sup> and HO<sub>4</sub>C<sub>2</sub><sup>-</sup>. Dihydrogen phosphate and hydrogen oxalate sample concentrations were chosen to be prepared in the micro-molar range based on previously reported detection limits of GEMBE.<sup>23,25</sup>

Figure 2.3 shows a plot of a separation of a 100-μM NaH<sub>2</sub>PO<sub>4</sub>, 300-μM Na<sub>2</sub>O<sub>4</sub>C<sub>2</sub> sample. The left and right peaks represent HO<sub>4</sub>C<sub>2</sub><sup>-</sup> and H<sub>2</sub>PO<sub>4</sub><sup>-</sup>, respectively. The pressure was decreased at a rate of -50 Pa/s from the starting pressure of 30,000 Pa until both peaks were detected. The elution of oxalate at an earlier time corresponds to a higher pressure and a higher electrophoretic velocity as compared to the later-eluting phosphate. Peak identifications were made by comparing a run buffer separation (blank) with samples containing only NaH<sub>2</sub>PO<sub>4</sub>, only Na<sub>2</sub>O<sub>4</sub>C<sub>2</sub>, and both NaH<sub>2</sub>PO<sub>4</sub> and Na<sub>2</sub>O<sub>4</sub>C<sub>2</sub>. To make peak identifications, the separation parameters were held constant.



Phosphate	pK <sub>a</sub>
$\text{H}_3\text{PO}_4 \leftrightarrow \text{H}^+ + \text{H}_2\text{PO}_4^-$	2.12
$\text{H}_2\text{PO}_4^- \leftrightarrow \text{H}^+ + \text{HPO}_4^{2-}$	7.21
$\text{HPO}_4^{2-} \leftrightarrow \text{H}^+ + \text{PO}_4^{3-}$	12.67
Oxalate	
$\text{H}_2\text{O}_4\text{C}_2 \leftrightarrow \text{H}^+ + \text{HO}_4\text{C}_2^-$	1.27
$\text{HO}_4\text{C}_2^- \leftrightarrow \text{H}^+ + \text{O}_4\text{C}_2^{2-}$	4.28

**Figure 2.3:** GEMBE separation of 100- $\mu\text{M}$   $\text{NaH}_2\text{PO}_4$  and 300- $\mu\text{M}$   $\text{Na}_2\text{O}_4\text{C}_2$ . This sample was prepared in 100-mM  $\beta$ -alanine, 80-mM HCl run buffer. Hydrogen oxalate elutes at a higher pressure (left) and dihydrogen phosphate elutes at a lower pressure (right). All of the pK<sub>a</sub>s of  $\text{H}_3\text{PO}_4$  and  $\text{H}_2\text{O}_4\text{C}_2$  are indicated on the right.

Based on the pK<sub>a1</sub> of arsenic acid (Figure 2.4), the dihydrogen arsenate anion,  $\text{H}_2\text{AsO}_4^-$ , is expected to elute closer to  $\text{H}_2\text{PO}_4^-$  than to  $\text{HO}_4\text{C}_2^-$ . The plot in Figure 2.4 shows the separation of a 100- $\mu\text{M}$   $\text{NaH}_2\text{PO}_4$ , 300- $\mu\text{M}$   $\text{Na}_2\text{O}_4\text{C}_2$ , and 50- $\mu\text{M}$   $\text{Na}_2\text{HAsO}_4$  sample, with the  $\text{H}_2\text{AsO}_4^-$  peak to the right of  $\text{H}_2\text{PO}_4^-$ . The separation parameters were held constant to allow the arsenate peak to be identified by comparing the plots in Figure 2.3 and Figure 2.4. The large elution time difference between  $\text{HO}_4\text{C}_2^-$  and  $\text{H}_2\text{PO}_4^-$  increases the time for a separation and, because  $\text{H}_2\text{O}_4\text{C}_2$  is not of primary interest, it can be eliminated from future samples.

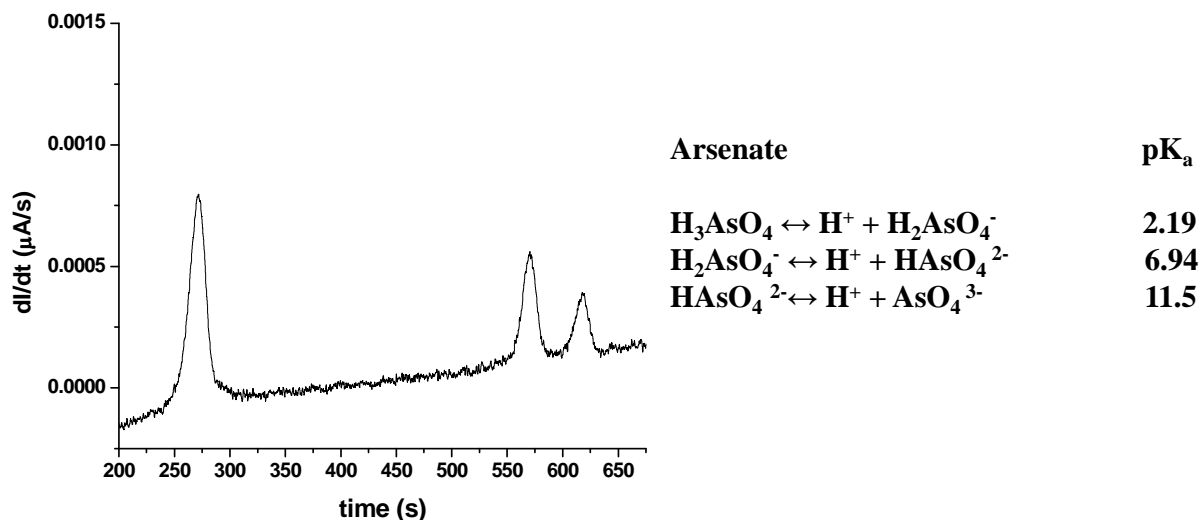


**Figure 2.4:** GEMBE separation of a sample containing 100- $\mu\text{M}$   $\text{NaH}_2\text{PO}_4$ , 300- $\mu\text{M}$   $\text{Na}_2\text{O}_4\text{C}_2$ , and 50- $\mu\text{M}$   $\text{Na}_2\text{HAsO}_4$ . This sample was prepared in 100-mM  $\beta$ -alanine, 80-mM HCl run buffer. The  $\text{HO}_4\text{C}_2^-$ ,  $\text{H}_2\text{PO}_4^-$ , and  $\text{H}_2\text{AsO}_4^-$  peaks elute from high to low pressures (left to right), respectively.

The first set of  $\text{NaH}_2\text{PO}_4$  and  $\text{Na}_2\text{HAsO}_4$  samples was a series of 2-fold run buffer dilutions of a 100- $\mu\text{M}$   $\text{NaH}_2\text{PO}_4$ , 50- $\mu\text{M}$   $\text{Na}_2\text{HAsO}_4$  sample (Figure 2.5A). The y-axis of each separation was manually adjusted to allow for visualization of the analyte peaks. For these separations, the starting pressure was decreased from the pressure that was used for the separations that include  $\text{Na}_2\text{O}_4\text{C}_2$  to minimize the separation time. As a consequence of this decrease, the time that the analyte peaks take to elute is much shorter in Figure 2.5A than in Figures 2.3 and 2.4, however the elution pressure remains the same. Non-linear least-squares fits were performed in Mathematica to determine the limit of detection (LOD) of approximately 15  $\mu\text{mol/L}$ .

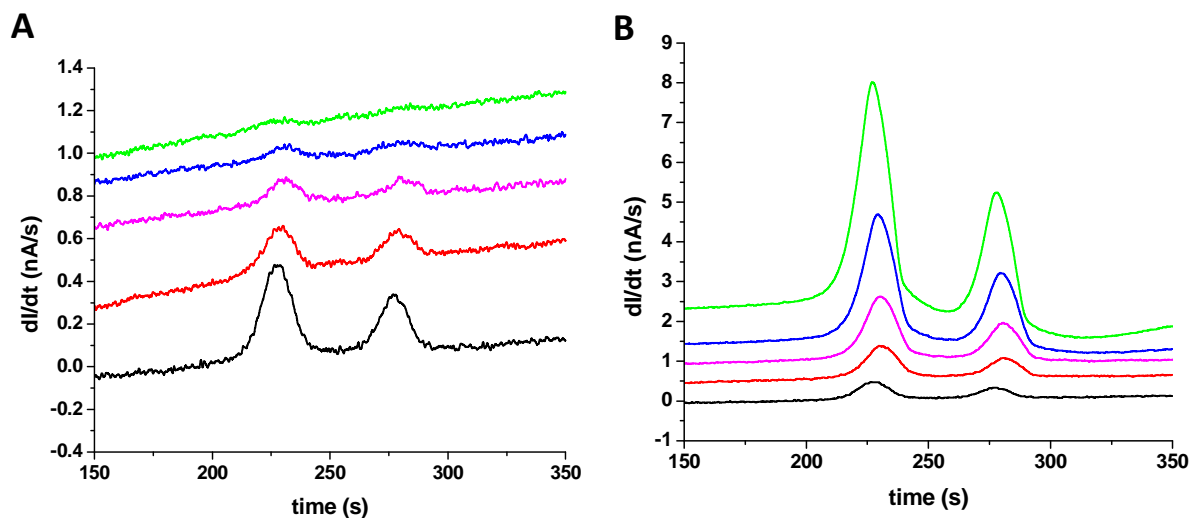


**Figure 2.5:** Separations of  $\text{H}_2\text{PO}_4^-$  and  $\text{H}_2\text{AsO}_4^-$  (A) in run buffer and (B) diluted with DI water. Concentrations decrease from the initial  $1\times$  concentration of  $100\text{-}\mu\text{M}$   $\text{H}_2\text{PO}_4^-$  and  $50\text{-}\mu\text{M}$   $\text{H}_2\text{AsO}_4^-$  (black), to  $2\times$  (red),  $4\times$  (pink),  $8\times$  (blue) and  $16\times$  (green). The peak height is increased for samples diluted to their final concentrations with DI water as compared to samples prepared in only run buffer.

In the next set of data, a 2-fold dilution series was prepared by dilution with DI water. The motivation for this dilution was a sample concentration effect reported by Munson *et al.* with temperature gradient focusing (TGF) in which samples with lower conductivities than the run buffer were analyzed.<sup>62</sup> The origin of this sample concentration is included in Chapter 1, and experimental details will be discussed in detail in Chapter 3. By diluting the samples with DI water, the concentrations of the buffer ions and the sample ions are decreasing, so the sample diluted with DI water has a lower conductivity than the GEMBE run buffer. The GEMBE separations of the 2-fold DI water diluted samples are shown in Figure 2.5B. As in Figure 2.5A, the y-axis of each separation has been manually adjusted to allow for visualization of the analyte peaks. In contrast to the 2-fold run-buffer-diluted samples, as the DI-water-diluted samples decrease in concentration, the signal increases. A detection limit for this set of data could not be determined because each sample had a different run buffer concentration. Before determining a detection limit for samples at a constant

dilution factor,  $\text{H}_2\text{PO}_4^-$  and  $\text{H}_2\text{AsO}_4^-$  need to be detected successfully in tap water to check for co-eluting species.

A sample containing 200- $\mu\text{M}$   $\text{NaH}_2\text{PO}_4$  and 60- $\mu\text{M}$   $\text{Na}_2\text{HAsO}_4$  was diluted 10-fold with tap water obtained from the laboratory sink at the National Institute of Standards and Technology (NIST, Gaithersburg, MD) to a final concentration of 20- $\mu\text{M}$   $\text{NaH}_2\text{PO}_4$  and 6- $\mu\text{M}$   $\text{Na}_2\text{HAsO}_4$ . Separations of this sample diluted 10-fold with DI water and diluted 10-fold with tap water are plotted in Figure 2.6B. Both analyte peak heights are larger in the sample diluted with tap water. The increase in the  $\text{H}_2\text{PO}_4^-$  peak height is likely due to the natural presence of phosphate anions in the tap water. Sodium phosphate was still added to the sample to ensure that tap water samples collected at different times would have a measurable  $\text{H}_2\text{PO}_4^-$  peak. The peak eluting at the position where  $\text{H}_2\text{AsO}_4^-$  is expected to elute is also much larger, and a shoulder on the peak near 310 s indicates a co-eluting species. To determine if  $\text{H}_2\text{PO}_4^-$  and  $\text{H}_2\text{AsO}_4^-$ , or an unknown co-eluting species are present in tap water, a run buffer sample diluted 2-fold with tap water was separated and compared to a 2-fold diluted sample containing  $\text{NaH}_2\text{PO}_4$ . The resulting signal is included in the Appendix (A.3), and confirms that  $\text{H}_2\text{PO}_4^-$  is present in tap water, and the shoulder around 310 s in Figure 2.6B is  $\text{H}_2\text{AsO}_4^-$ .

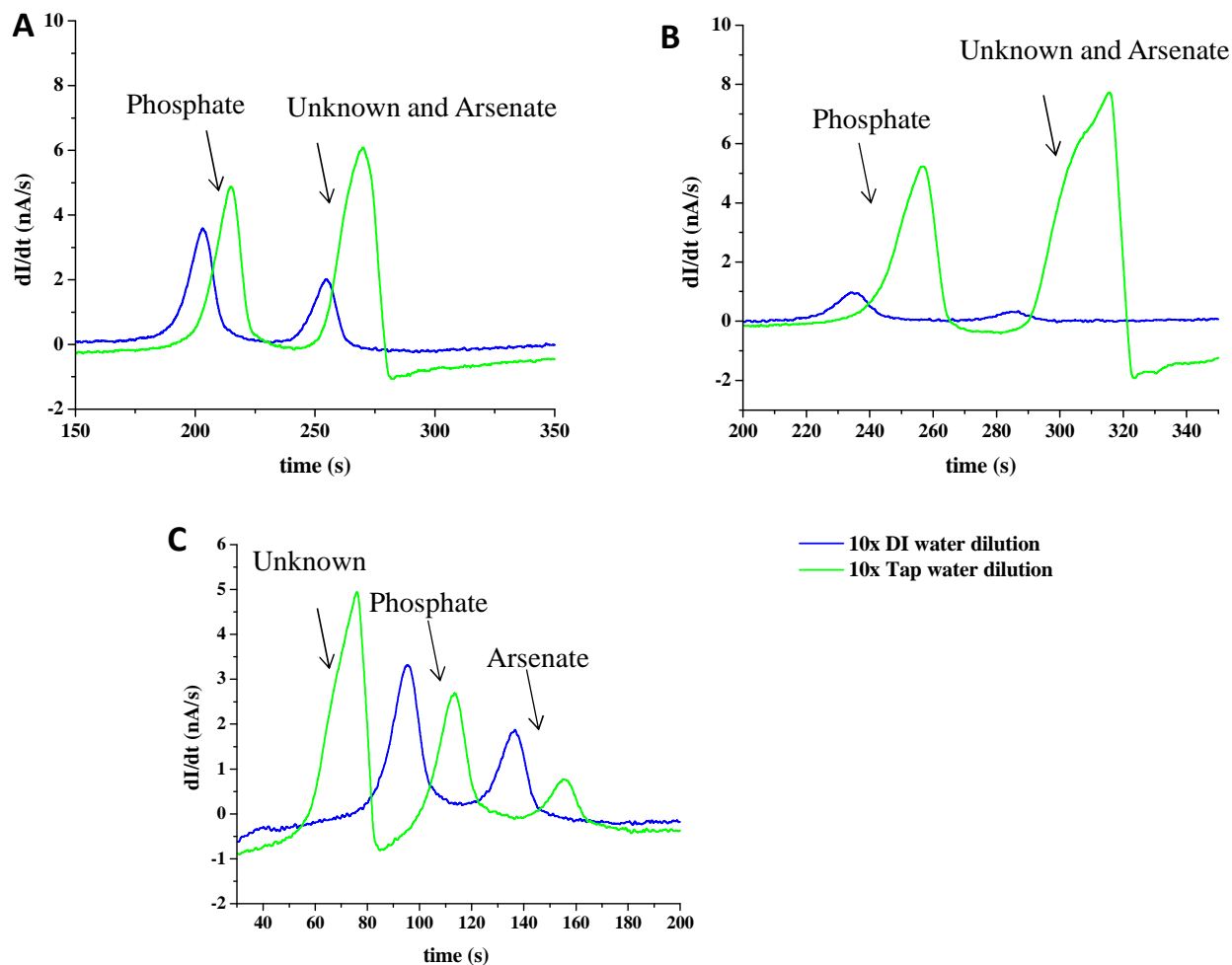


**Figure 2.6:** A comparison of  $\text{H}_2\text{PO}_4^-$  and  $\text{H}_2\text{AsO}_4^-$  separations in three different run buffers. (A) The final sample concentration is 10- $\mu\text{M}$   $\text{NaH}_2\text{PO}_4$ , 5- $\mu\text{M}$   $\text{Na}_2\text{HASO}_4$  in a buffer concentration of 100-mM  $\beta$ -alanine, 90-mM HCl (pH = 2.6) run buffer. (B) The final sample concentration is 2- $\mu\text{M}$   $\text{NaH}_2\text{PO}_4$ , 500-nM  $\text{Na}_2\text{HASO}_4$  in a buffer concentration of 100-mM  $\beta$ -alanine, 80-mM HCl (pH = 3.0). (C) The final sample concentration is 10- $\mu\text{M}$   $\text{NaH}_2\text{PO}_4$ , 5- $\mu\text{M}$   $\text{Na}_2\text{HASO}_4$  in a buffer concentration of 100-mM  $\beta$ -alanine, 70-mM HCl (pH = 3.2). The unknown species co-elutes with  $\text{H}_2\text{AsO}_4^-$  at pH = 2.6 and at pH = 3.0, but at pH = 3.2, all three species can be resolved. All three signals are shifted when diluted with DI water relative to tap water, and the direction of the shift changes with pH. This is a result of slight differences in the pH and conductivity of each solution, as well as the use of multiple capillary devices.

To resolve  $\text{H}_2\text{AsO}_4^-$  and the unknown co-eluting species, two slightly different buffer compositions were prepared. Figure 2.6A shows 100 mM  $\beta$ -alanine, 90 mM HCl (pH = 2.6) and Figure 2.6C shows 100-mM  $\beta$ -alanine, 70-mM HCl (pH = 3.2). At a pH of 2.6,  $\text{H}_2\text{AsO}_4^-$  still co-elutes with the unknown species in tap water, but at a pH of 3.2,  $\text{H}_2\text{PO}_4^-$ ,  $\text{H}_2\text{AsO}_4^-$ , and the unknown

species are resolved. To apply GEMBE to the separation of  $\text{H}_2\text{PO}_4^-$  and  $\text{H}_2\text{AsO}_4^-$  in environmental water samples, such as tap water, a buffer pH of 3.2 is necessary to allow the analytes to be resolved from an unknown, co-eluting species.

## 2.4 Conclusion

GEMBE combined with channel current detection is a separation technique that is ideal for the analysis of low concentration samples in potentially complex or dirty samples, and can be used to analyze charged molecules with relatively short analysis times. However, many potential applications of GEMBE, such as the detection of dihydrogen phosphate and dihydrogen arsenate presented here, would still benefit from decreasing the LOD of GEMBE. The following chapter describes GEMBE with a simple concentration enhancement method, field amplified continuous sample injection (FACSI), which has been implemented to decrease the LOD of GEMBE with channel current detection.

## Chapter 3: GEMBE with concentration enhancement

### 3.1 Introduction

This chapter is based on the work that was published in *Analytical Chemistry* in February of 2014 entitled “Gradient Elution Moving Boundary Electrophoresis with Field-Amplified Continuous Sample Injection” (citation). That work, and this chapter, focuses on decreasing the limit of detection (LOD) of GEMBE by combining it with a simple concentration enhancement method, field amplified continuous sample injection (FACSI), which was discussed in section 1.3.

### 3.2 Experimental

#### 3.2.1 Analyte system

With sensitivity enhancement methods in general, and with electrophoretic stacking and focusing methods in particular, it is often possible to achieve a high degree of preconcentration or sensitivity enhancement without any actual improvement in the detection limit of a trace analyte of interest in a real sample matrix. The reason for this lack of LOD improvement is that the interfering species in a real matrix are often preconcentrated along with the trace analytes. If the detection limit is primarily determined by the ability to detect the trace analytes against a higher background concentration of interfering species, stacking or focusing of the sample may not provide the expected benefit in LOD. Thus, when assessing the utility/applicability of a preconcentration method, it is important to consider preconcentration in the context of a trace analyte in a matrix with one or more difficult-to-resolve interferences. For this reason, and because arsenic is of interest due to its toxicity,

dihydrogen phosphate ( $\text{H}_2\text{PO}_4^-$ ) and dihydrogen arsenate ( $\text{H}_2\text{AsO}_4^-$ ) are used as a model analyte system. The two singly-charged anions have similar electrophoretic mobilities, making them difficult to separate electrophoretically. In typical natural water samples, phosphate anions are present in the micromolar range, whereas arsenic contamination is either absent or is present only at a much lower concentration.<sup>59,60</sup>

### 3.2.2 Chemicals and reagents

All solutions were prepared with deionized (DI) water (18.2-M $\Omega$ -cm, Barnsted Easypure II ultrapure water system). Stock solutions of 1-mmol/L sodium phosphate and sodium arsenate were prepared from monobasic sodium phosphate ( $\text{NaH}_2\text{PO}_4$ , Sigma) and dibasic sodium arsenate ( $\text{Na}_2\text{HAsO}_4$ , Sigma) by dissolving the salts in deionized water or in run buffer. The run buffer was 100-mmol/L in  $\beta$ -alanine (Fluka) and 70-mmol/L in HCl (32%, Fluka) with a pH of 3.2.

### 3.2.3 Procedures and analysis

The GEMBE device used to collect the data included in this chapter is identical to the device described in Chapter 2 (Figure 2.4). Specific details for each data set presented in this chapter are included in this section.

At the beginning of a typical separation, the counterflow pressure is set to 30,000 Pa for 6 s with the voltage off. Note that the zero of the time axis for Figures 3.1, 3.2, and 3.4 is at the beginning of this 6 s period. Then, the voltage is turned on to +1,000 V and the pressure is adjusted to the start pressure (indicated below) for 10 s, to stabilize the system. With the voltage on, the pressure is then decreased at a rate of 50 Pa/s from the start pressure to a minimum pressure determined by the electrophoretic velocity of the analytes of interest. At the end of each separation, the pressure is again increased to the start pressure for 10 s, after which the pressure is decreased to

30,000 Pa and the voltage is turned off until the next separation. Between separations, the pressure is set to 30,000 Pa for hold times between 0 and 30 min, and 5,000 Pa for hold times greater than 30 min. Analyte elution times (or step/peak locations) are identified by comparing blank buffer separations with separations in which individual analytes have been spiked in. During a typical separation, the volume transfer from the buffer reservoir into the sample reservoir is approximately 50 nL, or 0.1% of the sample volume. This volume was determined by considering the average flow rate (determined by the average pressure and the average capillary dimensions) and a typical separation time of 200 s.

Small shifts in elution pressure are typically observed when the capillary device is used for extended periods of time (~1 to 2 weeks) or when comparing data sets collected with different capillaries. These shifts are possibly due to irregularities at the cut edges of the capillary, small differences in capillary length, or small changes in the electroosmotic mobility of the capillary walls. Rinsing the capillary with sodium hydroxide (NaOH, 0.1-mol/L, Beckman Coulter) often affects the recovery of original elution pressure when data sets are collected over an extended time period (~2 to 3 days). However, even when elution pressures shift, the peak spacing between  $\text{H}_2\text{PO}_4^-$  and  $\text{H}_2\text{AsO}_4^-$  remains constant. Finally, it is important to prevent air bubbles from entering the device for the reasons that were discussed in Chapter 2.

For the data included in this chapter, each sample was separated in triplicate, and the sample reservoir was rinsed once with the next sample to be analyzed. Samples were prepared in run buffer and diluted to their final concentrations with run buffer, DI water, or tap water, as specified. Current-derivative data were plotted as a function of time with Origin 7.5 using a 51-point Savitzky-Golay derivative<sup>58</sup> and at least 300-point adjacent averaging smoothing. LOD calculations were calculated from step heights (equivalent to peak areas) obtained from the nonlinear fitting of the raw current

versus time data (done with Mathematica 7.0) as described by Ross *et al.* (a sample Mathematica worksheet is included in the Appendix, A.2).<sup>22</sup>

### 3.3 Results

The species of interest,  $\text{H}_2\text{PO}_4^-$  and  $\text{H}_2\text{AsO}_4^-$ , are shown in the inset of Figure 3.1A along with their corresponding  $\text{p}K_a$  values. At a run buffer pH of 3.2, both species are anionic. As a first illustration of the effect of combining field amplification (FACSI) with GEMBE, two sets of experiments were performed. In both cases, a 2:1 ratio of  $\text{NaH}_2\text{PO}_4$  to  $\text{Na}_2\text{HAsO}_4$  was used, and a series of samples was prepared by 2-fold serial dilution starting with a sample of 100- $\mu\text{mol/L}$   $\text{NaH}_2\text{PO}_4$  and 50- $\mu\text{mol/L}$   $\text{Na}_2\text{HAsO}_4$  prepared in run buffer. For the first set of experiments, the samples were prepared by dilution with the run buffer so that the conductivity of each sample was the same as the conductivity of the run buffer used to fill the buffer reservoir and the capillary. This case represents the normal mode of GEMBE without FACSI.

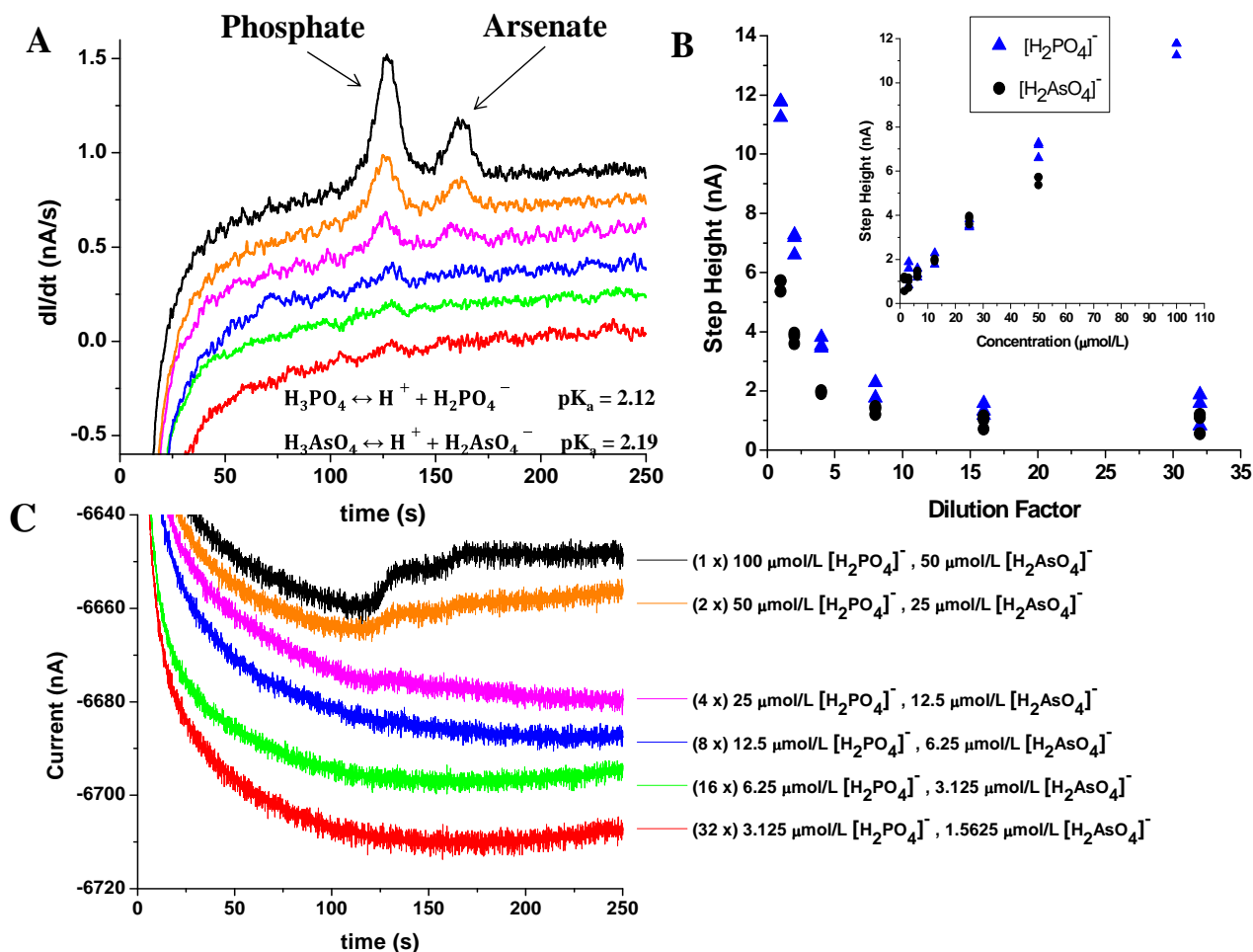


**Figure 3.1:** GEMBE for samples prepared via a serial 2-fold dilution of 100- $\mu\text{M}$   $\text{NaH}_2\text{PO}_4$  (left peak), 50- $\mu\text{M}$   $\text{Na}_2\text{HAsO}_4$  (right peak). The start pressure was 35,000 Pa and the pressure ramp rate was  $-50$  Pa/s. Dilutions were performed with run buffer so that the sample conductivity was the same as the run buffer conductivity, and samples were analyzed in triplicate. (A) Time derivative of the current vs time. Dilution factor increases from top to bottom as indicated in (C) from 1 $\times$  to 32 $\times$ . Inset: species of interest with relevant  $\text{pK}_{\text{a}}$ s. Other  $\text{pK}_{\text{a}}$ s are  $\text{pK}_{\text{a}2} = 7.21$  and  $\text{pK}_{\text{a}3} = 12.67$  for phosphoric acid and  $\text{pK}_{\text{a}2} = 6.94$  and  $\text{pK}_{\text{a}3} = 11.5$  for arsenic acid. (B) Step height (equivalent to the peak area from panel A) vs dilution factor. As the samples are progressively diluted and as the analyte concentration decreases, the signal decreases. The LOD for  $\text{H}_2\text{AsO}_4^-$  is approximately 12  $\mu\text{mol/L}$  (signal-to-noise ratio equal to 3). Inset: step height vs concentration. (C) Raw current as a function of time data. Step identities are the same as those in (A).

Figure 3.1A shows the GEMBE electropherograms for samples prepared in run buffer. For visualization of the data as peaks, the plots show the time derivative of the current as a function of time. The raw current as a function of time data, which were used for quantitative fitting, are shown

in Figure 3.1C. The peak on the left represents the dihydrogen phosphate anion,  $\text{H}_2\text{PO}_4^-$ , and the peak on the right represents the dihydrogen arsenate anion,  $\text{H}_2\text{AsO}_4^-$ . The location of  $\text{H}_2\text{PO}_4^-$  at an earlier elution time corresponds to higher counterflow pressure and larger electrophoretic velocity ( $v_{ep}$ ) when compared to the later-eluting  $\text{H}_2\text{AsO}_4^-$ . When the samples are progressively diluted and the analyte concentration decreases, the GEMBE signal decreases as well. Under these conditions, the LOD for  $\text{H}_2\text{AsO}_4^-$  is approximately 12  $\mu\text{mol/L}$  (signal-to-noise ratio equal to 3, see inset to Figure 3.1B).

For the second set of experiments, the samples were prepared by dilution with DI water instead of run buffer. In this case, as the samples were progressively diluted, the concentrations of both the analyte ions and the buffer ions in each sample were reduced. The concentration of the run buffer used to fill the buffer reservoir and capillary was left constant, resulting in field amplification during the separation. Consequently, with these diluted samples, an interface is formed between the high-conductivity run buffer and the lower-conductivity sample solution. Figure 3.2A is a plot of the time derivative of the current as a function of time for the samples prepared by dilution with DI water. The raw data are included in Figure 3.2C.

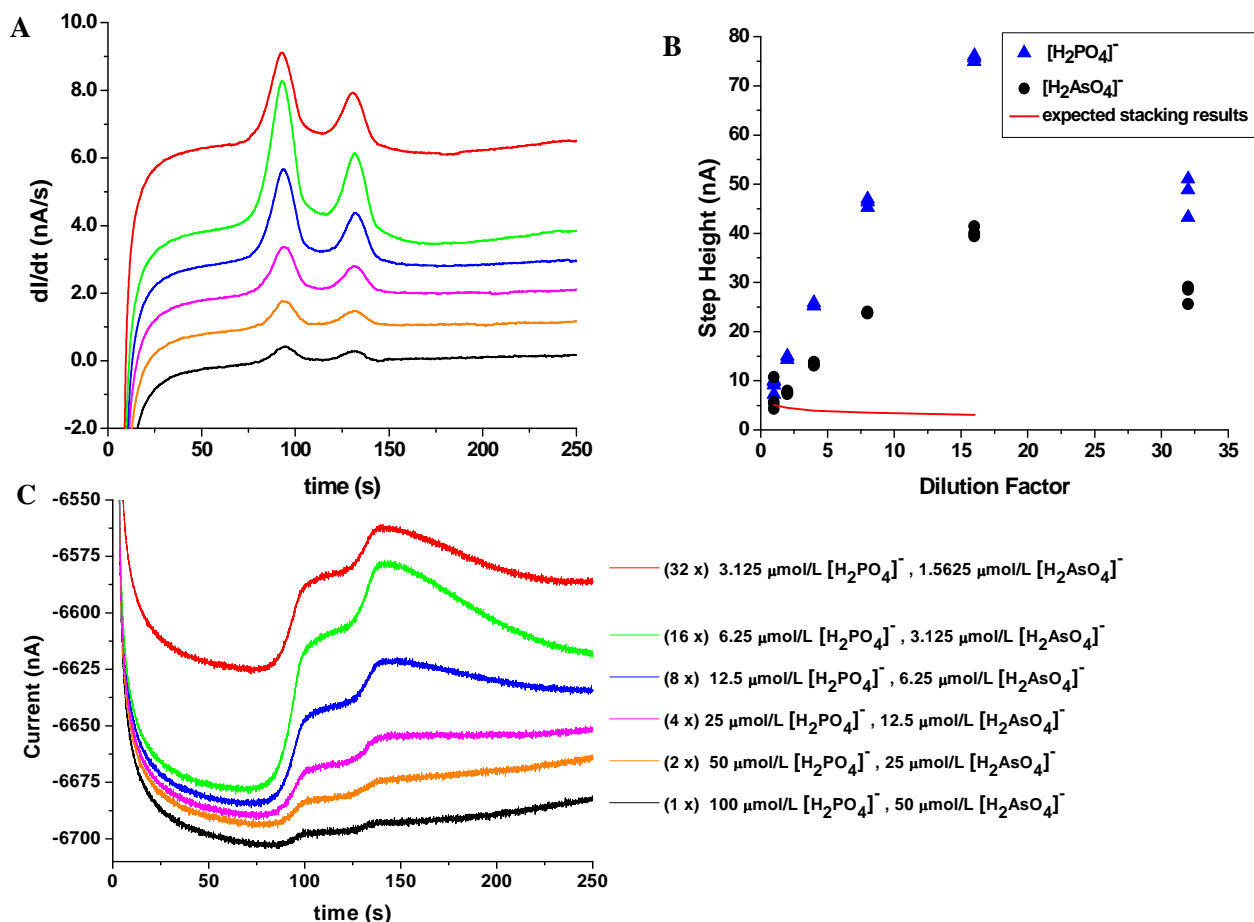


**Figure 3.2:** GEMBE for samples with a serial 2-fold dilution of 100- $\mu\text{M}$   $\text{NaH}_2\text{PO}_4$  (left peak), 50- $\mu\text{M}$   $\text{Na}_2\text{HAsO}_4$  (right peak). The start pressure was 36,000 Pa, and the pressure ramp rate was  $-50$  Pa/s. Salts were dissolved in run buffer, and dilutions were performed with DI water so that the sample conductivity was progressively reduced relative to the run-buffer conductivity. (A) Dilution factor increases from bottom to top: 1 $\times$  to 32 $\times$  as indicated in (C). In contrast to the data presented in Figure 3.1, as the analyte concentration is progressively decreased at larger dilution factors, the signal increases. (B) The solid line represents the result expected if concentration enhancement were due only to a normal (nonfocusing) stacking mechanism. The line was calculated using the following equation: (step height at dilution factor 1) $\times$ (conductivity ratio)/(dilution factor). The expected result decreases slightly as the dilution factor is increased because both the analytes ( $\text{H}_2\text{PO}_4^-$  and  $\text{H}_2\text{AsO}_4^-$ ) and the buffer ions ( $\beta$ -alanine and chloride) are being diluted and because the buffer conductivity decreases nonlinearly with dilution. A comparison with the GEMBE data shows the signal enhancement using GEMBE-FACSI. (C) Raw current as a function of time data. Step identities are the same as those in Figure 3.1.

As the samples were progressively diluted, the observed signals actually increased. This trend holds until the samples were diluted between 16- and 32-fold, at which point the conductivity of the diluted sample buffer stopped decreasing. The solid line in Figure 3.2B represents the result expected

if concentration enhancement were due only to a normal (nonfocusing) stacking mechanism, with the dilution of analyte to lower concentration approximately balanced by concentration enhancement (equal to conductivity ratio) from stacking. The conductivities of samples diluted with DI water were obtained by measuring a series of samples prepared identically to those used for analysis, except  $\text{H}_2\text{PO}_4^-$  and  $\text{H}_2\text{AsO}_4^-$  were not included. These values were used to determine the conductivity ratio of diluted samples to run buffer. To calculate the signal expected from normal stacking, the  $1\times$  (undiluted) step height was divided by the dilution factor and multiplied by the conductivity ratio. A comparison of this expected result and the GEMBE experimental data shows the much larger signal enhancement achieved using the FACSI mechanism presented here.

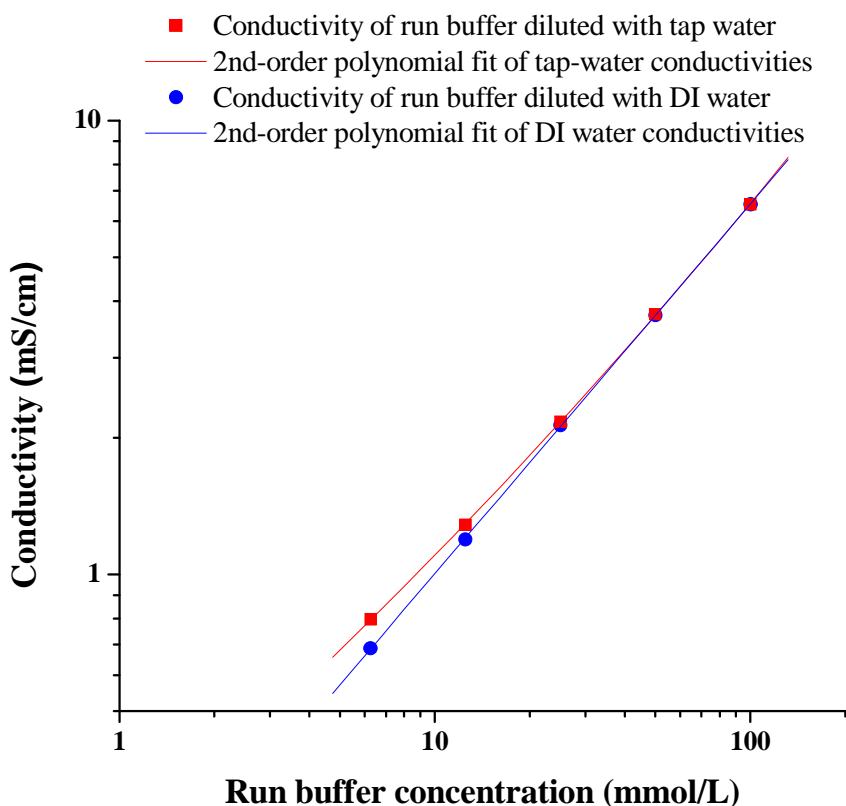


**Figure 3.3:** Logarithmic plot of conductivity as a function of run buffer concentration. The conductivities of run buffer diluted with tap (red) and DI (blue) water begin to diverge around a dilution factor of 10.

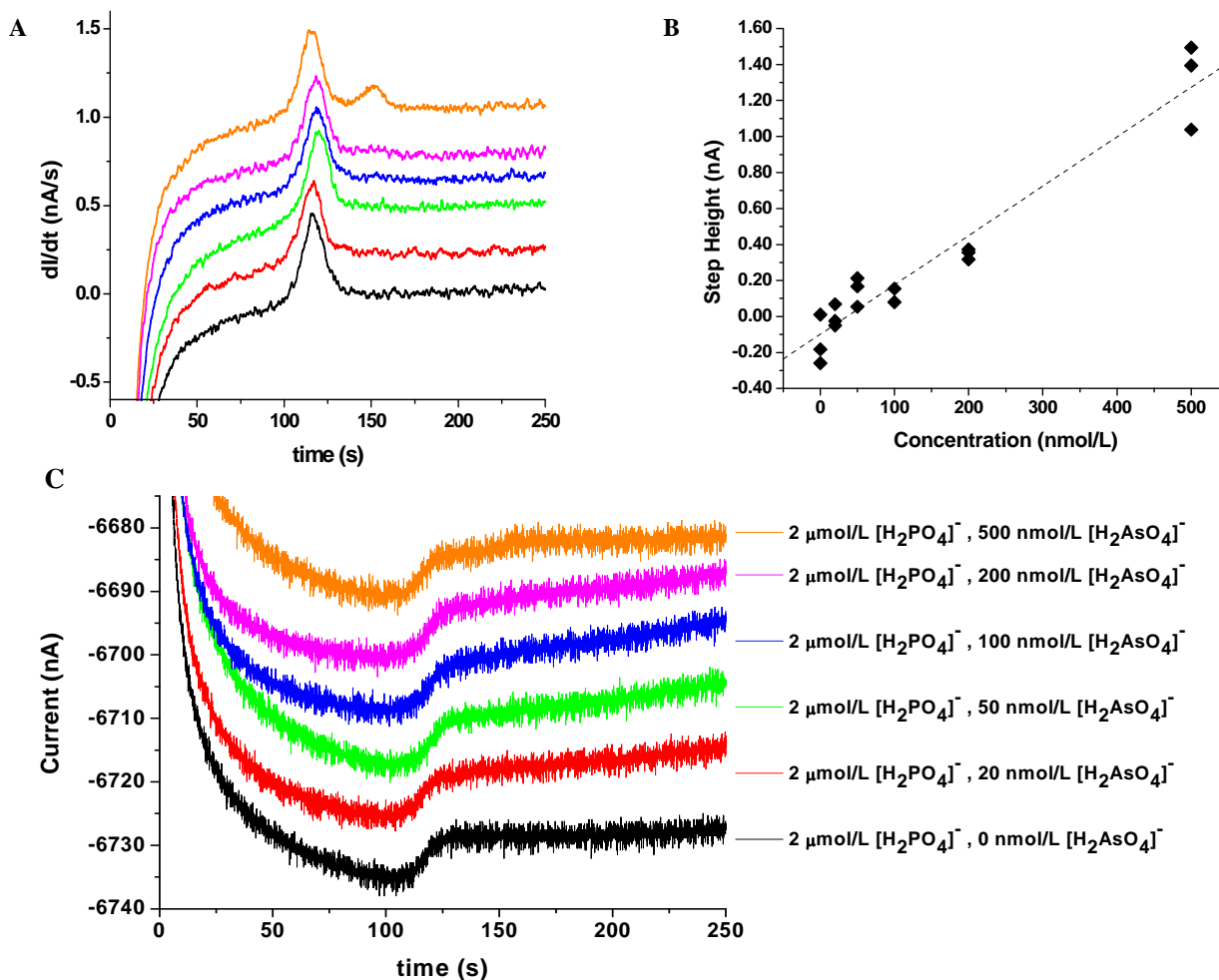


**Figure 3.4:** FACS-GEMBE data with sample buffer diluted 10 $\times$  (with DI water) relative to the run buffer. Samples were analyzed in triplicate. The start pressure was 38,000 Pa, and the pressure ramp rate was  $-50$  Pa/s. (A) Time derivative of the current as a function of time. The  $\text{H}_2\text{PO}_4^-$  (left peak) is held constant at 2  $\mu\text{mol/L}$ , and  $\text{H}_2\text{AsO}_4^-$  concentration (right peak) decreases from top to bottom: 500, 200, 100, 50, 20, 10, 0 nmol/L as indicated in (C). (B) Step height (equal to peak area from panel A) vs concentration. The LOD for  $\text{H}_2\text{AsO}_4^-$  is reduced approximately 80-fold from 12  $\mu\text{mol/L}$  (Figure 3.1) to 150 nmol/L. The dotted line represents a linear fit to all data points. (C) Raw current as a function of time data. Step identities are the same as those in Figure 3.1.

To determine the LOD of GEMBE with FACS, a series of samples was prepared in a buffer diluted 10 $\times$  with DI water relative to the run buffer. A dilution factor of 10 $\times$  (conductivity ratio = approximately 6.52) was chosen because it was the maximum dilution factor at which the conductivity of buffer diluted with tap water was similar to that of buffer diluted with DI water (Figure 3.3). This condition ensures that the conductivity of the sample will be determined primarily

by the diluted buffer ions and not by other ions present in a sample matrix (such as well water, pond water, or tap water). These samples, shown in Figure 3.4, were prepared in run buffer at an analyte concentration 10× higher than desired and they were then diluted with DI water to the final concentration. The final  $\text{H}_2\text{PO}_4^-$  concentration was held constant at 2  $\mu\text{mol/L}$ , and the final  $\text{H}_2\text{AsO}_4^-$  concentration was varied from 0 to 500  $\text{nmol/L}$ . Note that, for this LOD determination, the concentration of buffer ions in the samples was held constant, so the signal decreases as the analyte concentration decreases. The LOD for FACSI–GEMBE with DI water was determined from the  $\text{H}_2\text{AsO}_4^-$  signal to be approximately 150  $\text{nmol/L}$ . Implementing the FACSI concentration enhancement method, we have achieved an 80× reduction in the LOD as compared to GEMBE without FACSI concentration enhancement (LOD = 12  $\mu\text{mol/L}$ ).

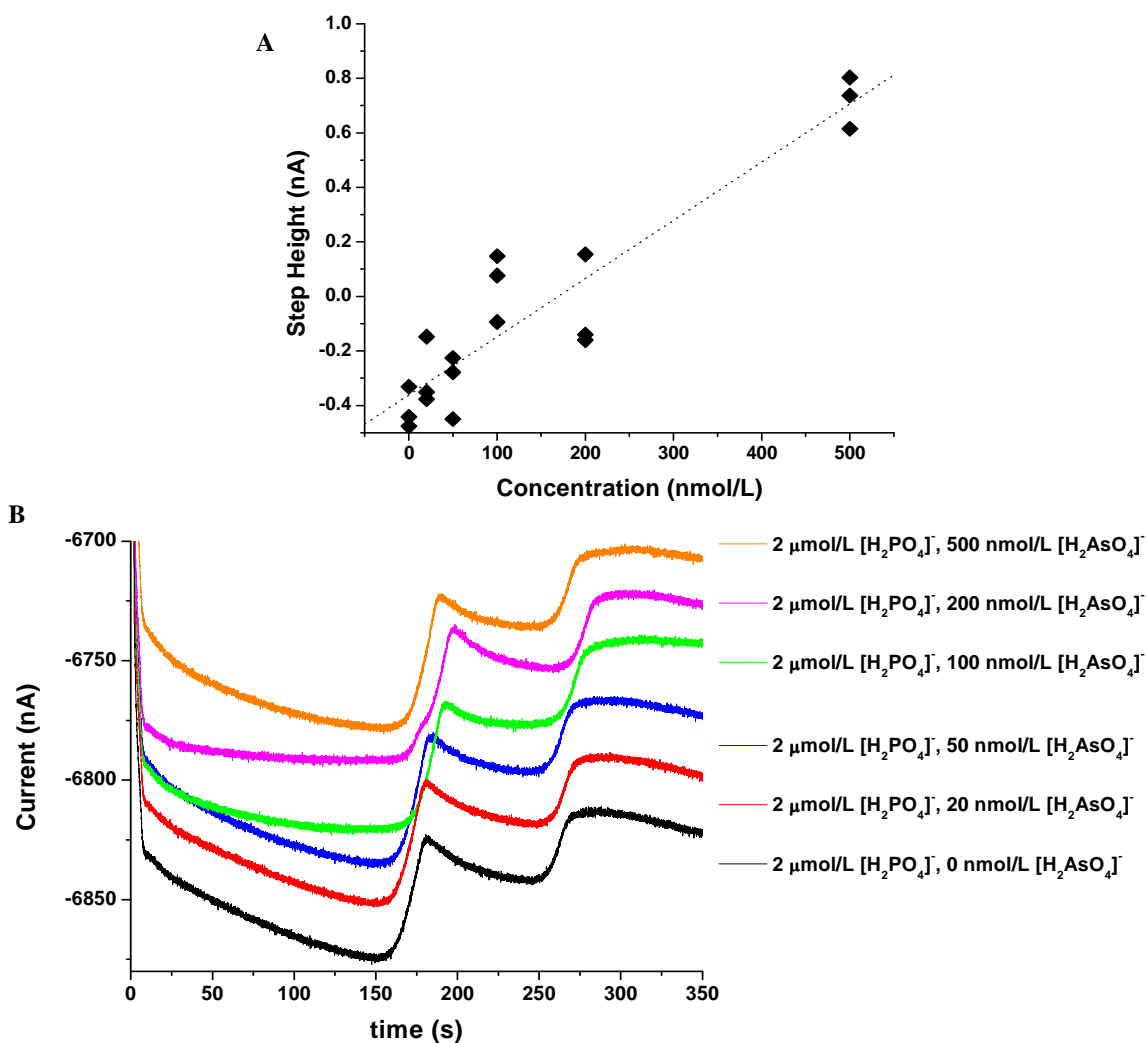


**Figure 3.5:** FACSI-GEMBE data for a series of samples prepared with 9 parts tap water, 1 part run buffer, with  $\text{NaH}_2\text{PO}_4$  and  $\text{Na}_2\text{HASO}_4$  spiked in to give the desired final  $\text{H}_2\text{PO}_4^-$  and  $\text{H}_2\text{AsO}_4^-$  concentrations. The start pressure was 45,000 Pa, and the pressure ramp rate was  $-50$  Pa/s. (A)  $\text{H}_2\text{AsO}_4^-$  step height vs concentration. The LOD for  $\text{H}_2\text{AsO}_4^-$  is reduced approximately 60-fold from  $12$   $\mu\text{mol/L}$  (Figure 3.2) to  $200$   $\text{nmol/L}$ . The dotted line represents a linear fit to all data points. (B) Raw current as a function of time data. The large peak around 150 seconds represents an unknown species in the tap-water samples.  $\text{H}_2\text{PO}_4^-$  elutes at approximately 250 seconds, followed by  $\text{H}_2\text{AsO}_4^-$ .

FACSI-GEMBE was then implemented to detect  $\text{H}_2\text{AsO}_4^-$  in drinking (tap) water (Figure 3.5). The samples were composed of 9 parts tap water and 1 part run buffer with  $\text{NaH}_2\text{PO}_4$  and  $\text{Na}_2\text{HASO}_4$  spiked in to give the desired final  $\text{H}_2\text{PO}_4^-$  and  $\text{H}_2\text{AsO}_4^-$  concentrations and a buffer ion concentration that was approximately  $10\times$  lower in the sample than in the run buffer. The

conductivity ratio for this set of measurements was approximately 5.93. Unspiked tap water showed a peak coeluting with  $\text{H}_2\text{PO}_4^-$  (expected since phosphate anions are often found in drinking water). Due to the relatively small size of this  $\text{H}_2\text{PO}_4^-$  peak, 2  $\mu\text{mol/L}$  additional  $\text{NaH}_2\text{PO}_4$  was spiked into the samples to give a  $\text{H}_2\text{PO}_4^-$  interference concentration comparable to that found in the natural/well water samples, as described by Kuban *et al.* and Nguyen *et al.*<sup>59,60</sup> With tap water samples, there was also an additional (unknown) species with an elution time similar to that of  $\text{H}_2\text{PO}_4^-$  and  $\text{H}_2\text{AsO}_4^-$  mentioned in Chapter 2. Baseline resolution of all three species ( $\text{H}_2\text{PO}_4^-$ ,  $\text{H}_2\text{AsO}_4^-$ , and unknown) was possible at the pH used here (3.2); at pH 3.0 better resolution between the  $\text{H}_2\text{PO}_4^-$  and  $\text{H}_2\text{AsO}_4^-$  peaks was obtained, but at this lower pH the unknown species found in the tap water coeluted with  $\text{H}_2\text{AsO}_4^-$  (Chapter 2, Figure 2.10).

The LOD for FACSI-GEMBE with tap water samples was approximately 200 nmol/L, as determined from the  $\text{H}_2\text{AsO}_4^-$  signal, corresponding to a 60 $\times$  improvement in the LOD over GEMBE without FACSI (Figure 3.1). A previously described method for portable CE analysis of multiple arsenic species achieved a similar LOD (150 nmol/L), using a large-volume hydrodynamic injection method. As a comparison to environmentally relevant concentrations of arsenic, the FACSI-GEMBE LOD for  $\text{H}_2\text{AsO}_4^-$  is approximately 0.028 mg/L which is on the same order of magnitude as the maximum contaminant limit established for total arsenic by the United States Environmental Protection Agency and the guideline value set by the World Health Organization, 0.01 mg/L (10 ppb).

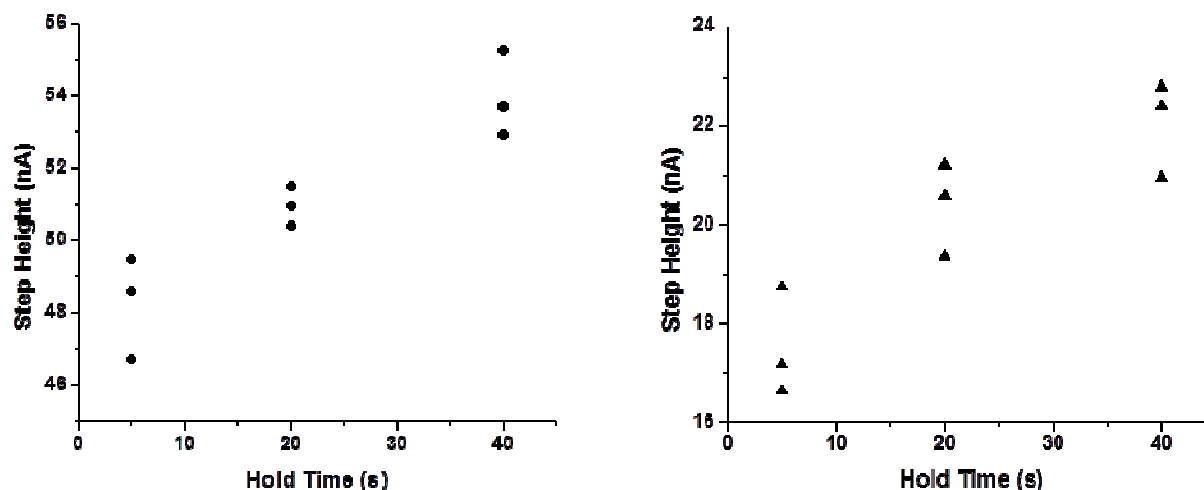


**Figure 3.6:** Step height (nA) for FACSI–GEMBE plotted vs hold time (s) for a 10- $\mu\text{M}$   $\text{NaH}_2\text{PO}_4$  and 5- $\mu\text{M}$   $\text{Na}_2\text{HAsO}_4$  sample that has been diluted 10 $\times$  from an original concentration of 100- $\mu\text{M}$   $\text{NaH}_2\text{PO}_4$  (left plot) and 50- $\mu\text{M}$   $\text{Na}_2\text{HAsO}_4$  (right plot). The start pressure was 53,000 Pa, and the pressure ramp rate was  $-50$  Pa/s. The  $\text{H}_2\text{PO}_4^-$  step height is shown in panel A, and the  $\text{H}_2\text{AsO}_4^-$  step height is shown in panel B. Hold time refers to the amount of time the start pressure was applied before beginning the pressure ramp. Both analytes show an increased step height with longer hold times, suggesting that concentration enhancement is occurring before the analyte enters the capillary and can be increased with a longer focusing time.

Finally, as a probe of the possible mechanism of unexplained large sensitivity improvement, we performed FACSI–GEMBE analyses of a 10- $\mu\text{M}$   $\text{NaH}_2\text{PO}_4$  and 5- $\mu\text{M}$   $\text{Na}_2\text{HAsO}_4$  sample that was diluted 10 $\times$  from an original concentration of 100- $\mu\text{M}$   $\text{NaH}_2\text{PO}_4$  (left plot) and 50- $\mu\text{M}$   $\text{Na}_2\text{HAsO}_4$  (right plot). Three separations of the same sample were performed (each in triplicate), the only difference being the hold time; the time that the start pressure was applied before beginning to decrease the pressure. As indicated in Figure 3.6, hold times of 5, 20, and 40 s were used. As the hold time increases, the step height increases for both analytes in the sample.

### 3.4 Discussion

The results presented in this chapter are inconsistent with the expectations for a simple field-amplified stacking method. The large observed sensitivity enhancement is likely related to the difference in the way analyte ions are introduced into the capillary with the GEMBE method as

compared with conventional capillary electrophoresis methods. The data that are presented support the existence of a solution boundary that remains outside of the separation capillary, which allows analytes to be stacked sequentially and introduced into the capillary for detection.

With conventional CE with field-amplified sample stacking (with only a conductivity difference across the boundary), the analyte ions are injected into the capillary at the beginning of the separation as a defined plug and the field-amplified stacking occurs at a buffer interface that is inside the capillary. The upper limit on concentration enhancement is then easily derived based on the conservation of electrophoresis current on either side of the interface.<sup>35</sup> In this case (with the interface inside the capillary), application of a solution counterflow (either electroosmotic, pressure-driven, or a combination of both) will cause the interface to move with the velocity of the counterflow, such that the concentration enhancement from stacking is unchanged by the counterflow.

With FACSI-GEMBE, however, the sample solution is left in contact with the capillary entrance throughout the course of the separation, and the counterflow is used to determine when each analyte is able to enter the capillary. Analyte ions are electrophoretically pulled into the capillary only when the counterflow is reduced to a velocity (inside the capillary) less than the electrophoretic velocity of each analyte. With field amplification, the low- and high-conductivity buffers differ only in concentration, and not in composition. Consequently, the buffer interface moves like an object with zero electrophoretic velocity, and with a counterflow, it never enters the capillary. In this case, field amplification occurs only in the sample space outside the capillary.

Another recently described method, termed electrophoretic exclusion,<sup>63,64</sup> is in some ways similar to the one described here in that analytes are focused at the entrance to a capillary and a counterflow is used to control when the analytes enter the capillary. In that method, however, the

focusing mechanism is clear since an electrode plated on the entrance end of the capillary is used to create a sharp electric-field gradient for focusing. With this method, enhancements of 40- and 1200-fold were reported for small dye molecules and proteins, respectively.

It is likely that, because the GEMBE sample space is large (approximately 3 mm) compared with the inner diameter of the capillary (5  $\mu\text{m}$ ), analyte ions in the sample far from the capillary entrance will not be affected by the counterflow. However, because of field amplification, they will be drawn toward the capillary entrance even when the counterflow velocity is too large to allow them to enter the capillary. Analyte ions then focus and accumulate at the interface until the counterflow is reduced sufficiently, at which time they enter the capillary at a greatly increased concentration. This explanation requires that the buffer interface remain near the capillary entrance and not expand outward from the entrance in spite of the continuous flow of higher concentration buffer exiting the capillary. Although we do not yet have a detailed model, in previous work, fluorescence microscopy of the region near the capillary entrance for TGF with FACSI<sup>62</sup> indicated that the interface is stable on the time scales of a TGF or GEMBE separation, and that the analyte molecules do indeed accumulate near the entrance. Additionally, this hypothesis is supported by the observed increase in step height shown in Figure 3.6. When a counterflow velocity greater than the electrophoretic velocity of all analytes is applied for longer times, the step height for a given analyte concentration increases. This behavior suggests that analytes are being focused at the entrance of the capillary, and greater signal enhancement can be achieved with a longer focusing time.

Presumably, the required stabilization of the buffer interface occurs as a consequence of the different transport regimes in the experiment. In the capillary and near its entrance, transport is dominated by convection and electrophoresis. In the sample space far from the entrance, transport is dominated by diffusion (or some similar, essentially random mixing process). Modeling results for

this experimental system could be helpful in clarifying the exact mechanism. However, reliable modeling of the system, with (possibly moving) conductivity gradients in a geometry that spans orders of magnitude in feature size, is not easy.

If the above proposed focusing mechanism (or something like it) is correct, then the technique described here may be more similar to the conductivity gradient focusing method developed by Greenlee and Ivory<sup>65</sup> and by Wang et al.<sup>45</sup> in which a buffer ion concentration gradient is formed by flowing the separation buffer through a hollow dialysis fiber or tube of dialysis membrane, while rinsing the outside of the tube or fiber with a lower concentration buffer. Proteins can be focused on the resulting conductivity gradient inside the fiber or tube. In particular, the results described by Wang et al. for which there was a sharp concentration gradient near one end of the dialysis fiber might be relevant for a more complete understanding of the results described here.

Other possible explanations of the greater than expected sensitivity enhancement include effects from pH and  $pK_a$  shifts resulting from the difference in ionic strength between the sample and run buffer and effects due to Joule-heating-induced temperature gradients. Calculation of the shifts in dissociation constants due to ionic strength changes<sup>66</sup> indicate that, to first order, the shift of the  $pK_a$  of the analytes and the shift of pH of the buffer solution are expected to be the same. Consequently, the charge state and electrophoretic mobility of the analyte ions are expected to remain approximately constant as the ions move across the boundary from low to high concentration.

From measurements of the nonlinearity of the electrophoresis current as a function of voltage, the temperature increase in the capillary is estimated to be 6.2 °C relative to the sample solution. This temperature gradient could, in principle, give rise to velocity differences as the analyte ions move from the cool sample buffer to the warmer run buffer inside the capillary. However, this velocity difference is expected to be small, as the effects from temperature-dependent viscosity exactly cancel.

Consequently, either the mobility of the buffer ions or the mobility of the analyte ion (or both) must have a temperature dependence different from that due to viscosity changes.<sup>67</sup> Using data for the relative mobilities and  $pK_a$ s (and their temperature dependence) of the buffer ions ( $\beta$ -alanine) and the analyte ions ( $H_2PO_4^-$ ),<sup>68</sup> the estimated change in analyte velocity due to the temperature gradient is approximately 3%. In addition to being much too small to account for the results reported here, this effect is in the wrong direction; the estimate indicates that the  $H_2PO_4^-$  ions should speed up and de-stack slightly as a result of the Joule heating effects.

### 3.5 Conclusion

Further work on FACSI-GEMBE should include efforts to develop a detailed understanding of the underlying mechanism for the observed high degree of sensitivity enhancement, to image the entrance of the capillary, to apply FACSI for sensitivity enhancement with other variants of GEMBE, and also to see if it can be implemented as a new injection mode with conventional CE. The next chapter discusses a method of fabrication that provides an avenue for the design of separation channels shorter than those currently attainable with the method of fabrication discussed above, with the goal of reducing the time required for a separation.

## Chapter 4: MAP fabrication of structures with circular cross-sections

### 4.1 Introduction

This chapter focuses on multiphoton absorption and its application to the fabrication of microstructures. The emphasis will be on the fabrication of structures with non-rectangular, 3-dimensional cross-sections that can be used as molds to make microfluidic structures.

### 4.2 Multiphoton absorption (MPA)

Multiphoton absorption (MPA) is a non-linear optical process in which a transition is driven by the simultaneous absorption of  $n$  photons (where  $n \geq 2$ ). Figure 4.1 shows single-photon absorption (blue arrow) and two-photon absorption (red arrows). In a single-photon process, a molecule is excited from the ground state ( $S_0$ ) to an excited state ( $S_n$ ) by the absorption of one photon. This single photon must have an energy that is equal to the energy difference between the ground and excited states. In a multiphoton process (two-photon in Figure 4.1), a molecule is excited by the simultaneous absorption of two or more photons. In this case, the sum of the energies of the photons must be equal to the energy difference between the ground and excited states.

In Figure 4.1, a two-photon process is depicted (red arrows) in which the two photons have the same energy ( $h\nu_2$ ). It is also possible for photons with different energies to cause excitation, as long as their combined energy is equal to the energy gap between the ground and excited states. The state labeled “virtual state” in Figure 4.1 is not a real state, so if a second photon is not present, no excitation will occur. Because simultaneous absorption is required, the probability of the occurrence of a multiphoton absorption event is proportional to the intensity of the incoming light to the power

of the number of photons absorbed,  $n$ . In the case of single-photon excitation,  $n = 1$ , so the probability of this event is proportional to the intensity of incident light.

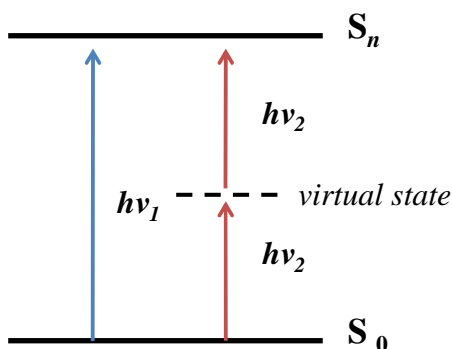


**Figure 4.1:** A simplified Jablonski diagram showing one-photon absorption (with photon energy  $h\nu_1$ ) with a blue arrow and two-photon absorption (with photon energy  $h\nu_2$ ) with two red arrows. Both absorption processes drive a transition from the ground state ( $S_0$ ) to the first excited state ( $S_n$ ). Two-photon absorption requires that the two photons be absorbed simultaneously. In this case,  $h\nu_2 = \frac{1}{2} h\nu_1$ .

To improve the probability of two-photon absorption, typically ultrafast lasers are directed through a microscope objective. Ultrafast lasers are used because they deliver high intensity pulses (with picosecond to femtosecond durations) and require a lower average power than using a high intensity, continuous-wave source. When an ultrafast laser is focused through a microscope objective, the intensity will only be high enough to cause MPA near the focal point of the laser beam. As a comparison, the cases of single- and two-photon excitation in a fluorescent dye are shown in Figure 4.2. Laser beams of two different wavelengths are focused in a fluorescent dye solution: on the left, a 380-nm laser beam and on the right a 760-nm laser beam. Single-photon excitation is observed through the entire cross-section of the cuvette (bottom), whereas multiphoton excitation only occurs in a small region at the focal point (top). The size of this region depends on the laser power and magnification of the microscope objective but is usually less than  $1 \mu\text{m}$  wide and greater than  $1 \mu\text{m}$  tall (with an aspect ratio of 1:2 or greater). The ability to achieve localized excitation

within a photosensitive material as shown in Figure 4.2 is a result of two-photon absorption being dependent on the square of the laser intensity.



**Figure 4.2:** Single-photon and two-photon absorption in a fluorescent dye. On the left, a laser beam of wavelength 380nm is focused and on the right a laser beam of wavelength 760nm is focused in the fluorescent dye. Single-photon excitation occurs throughout the cross-sectional volume of the cuvette, whereas multiphoton excitation only occurs in a small volume at the focal point of the microscope objective. The difference in these two cases is due to the linear and non-linear dependence on intensity in the single-photon and two-photon cases, respectively. (adapted from <http://chemistry.cos.ucf.edu/belfield/photophysics>)

The nonlinear dependence on intensity allows MPA to occur within a volume of photosensitive material without exposing the entire volume along the path of the laser beam. This characteristic of MPA can provide many advantages over single-photon excitation in areas such as spectroscopy, imaging, and fabrication.<sup>69-72</sup> The focus of the following sections is on the application of multiphoton absorption to the fabrication of microstructures.

### 4.3 Multiphoton absorption polymerization (MAP)

The unique ability of MPA to control excitation in three dimensions has been exploited to fabricate microstructures with arbitrary geometries that are not easily accessible by traditional

lithographic methods.<sup>73-75</sup> This technique was first introduced in 1997 by S. Maruo *et al.*<sup>76</sup> and has since been termed multiphoton absorption polymerization (MAP).<sup>69,70</sup> The MAP method of fabrication has been demonstrated to have the ability to create complex structures that incorporate features such as coils, large overhangs, and arbitrary cross-sections (Figure 4.3).

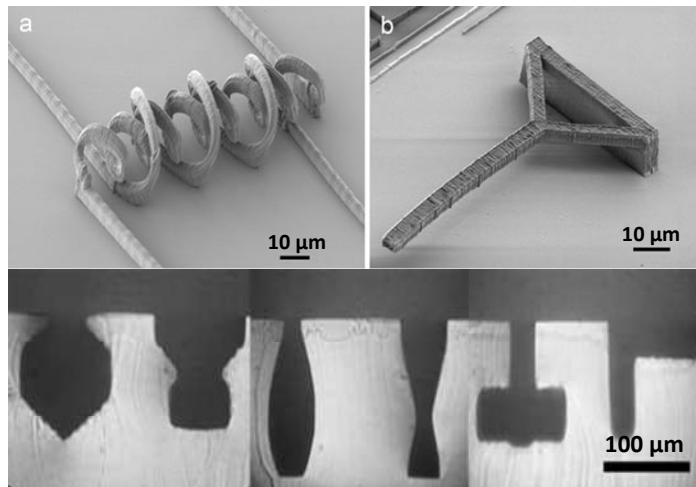


**Figure 4.3:** Representative structures fabricated with MAP: (a) interlocking coils, (b) a cantilever with a large overhang, and (c) molded structures with various cross-sectional geometries.<sup>69,70,73,75</sup>

Fabrication with MAP is typically performed in a photosensitive material called a photoresist, which contains monomers and a photoinitiator. The photoinitiator is excited by an ultrafast, pulsed laser focused through a microscope objective, and the photoresist or the laser beam is translated in the  $x$ ,  $y$ , and  $z$  directions to draw cross-linked polymer structures within the photoresist. The following sections will discuss the composition of a photoresist and the sample preparation required to fabricate structures successfully, as well as structures fabricated with MAP that can be used to create microfluidic devices.

#### 4.3.1 Photoresist: composition and preparation

There are two main types of photoresist, positive-tone and negative-tone. In both cases, the photoresist undergoes a change when the material is exposed to light. In a positive-tone photoresist,

the material becomes more soluble in the photoresist developer after exposure whereas in a negative-tone photoresist, the exposed area becomes insoluble in the photoresist developer after exposure. Negative-tone photoresists are most commonly used in MAP fabrication. These photoresists can be liquid (e.g., acrylate monomers) or solid (e.g., SU-8) during fabrication. Water-based photoresists for the fabrication of biologically compatible structures have also been developed.<sup>77</sup>

One facet of suitability of photoinitiators for MPA is often classified by the two-photon cross-section ( $\delta$ ) of the molecule, which is expressed as Equation 4.1.

$$\frac{d\varphi}{dz} = -\delta N_g \varphi^2 \quad \text{Equation 4.1}$$

The units for  $\delta$  are Göppert-Mayer (GM), named after the Nobel Laureate physicist who first predicted two-photon excitation. In SI units, 1 GM =  $10^{-58} \text{ m}^4 \text{ s photon}^{-1}$ . The photon flux, or number of photons per unit area and time, is represented by  $\varphi$ ,  $N_g$  is the number of molecules in the ground state, and  $z$  is the direction of propagation. As an example, the photoinitiator that will be discussed in the following sections, Lucirin TPO-L (Figure 4.4), has a two-photon cross-section of approximately 0.1 GM at 800 nm.<sup>78</sup>

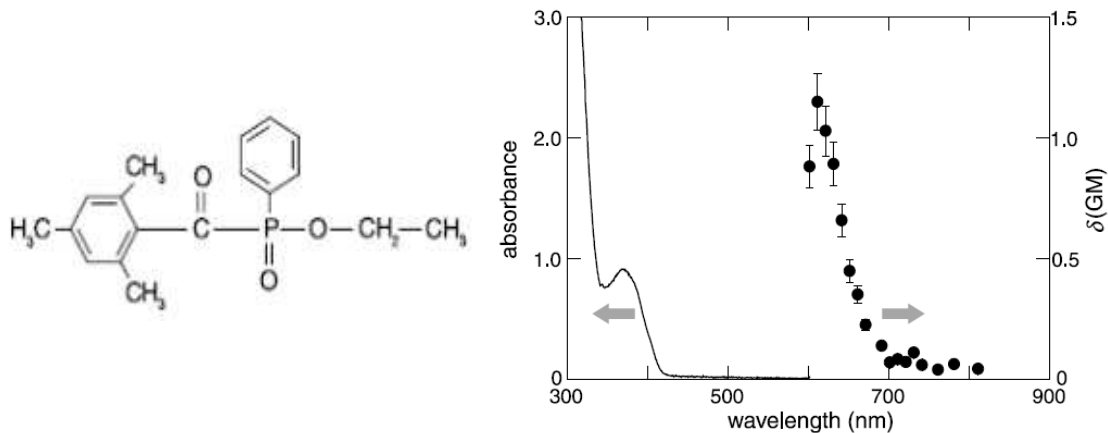


**Figure 4.4:** Ethyl 2, 4, 6-trimethylbenzoylphenylphosphinate (Lucirin TPO-L, photoinitiator). Structure (left), linear absorption spectrum and two-photon absorption cross-section spectrum (right).<sup>78</sup>

The other component of a negative-tone photoresist is the monomer (or monomers). The majority of the work contained in this document was performed using a negative-tone photoresist composed of a combination of acrylate monomers shown in Figure 4.5. The most common mixture was SR-499 and SR-368, which is liquid during fabrication. To prepare a typical photoresist (also called a resin), 3% (by weight) TPO-L photoinitiator is combined with SR-499 and SR-368 monomers mixed in a 1:1 weight percent ratio. First, Lucirin TPO-L (0.1 to 0.2 g) is measured in a glass vial. The mass of monomers needed is calculated from the photoinitiator mass (a sample calculation can be found in the Appendix, A.9), and the desired amount of each monomer is added to the same glass vial. In the case of monomers that are solid or have viscosities that make transfer difficult, the entire bottle of monomer is heated in a 95°C oven for 15 to 30 minutes to liquefy it or to decrease the viscosity. A batch of resin has a mass between 3 and 6 grams and can be used for a few months. Eventually the resin begins to crystallize, at which point it must be discarded. After all of the components are combined in a glass vial, they are heated for approximately 1 minute at 95°C and mixed on an inverting mixer overnight. Heating is necessary to decrease the viscosity of the resin

and to ensure that the mixture is homogeneous. For storage, the glass vial is covered with aluminum foil to keep stray light from reaching the resin and causing undesired polymerization. Before each use, the vial of resin is heated for approximately 1 minute at 95°C and centrifuged for 2-5 minutes to remove bubbles.

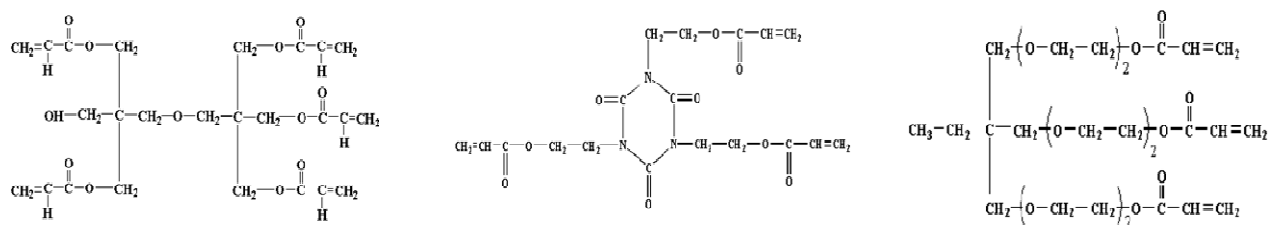


**Figure 4.5:** Components of a negative-tone photoresist (resin). The resin used here typically contains Lucirin TPO-L (Figure 4.3), SR-368 and either SR-399 or SR-499. Left to right: Diapentaerythritol pentaacrylate (SR-399, monomer), tris (2-hydroxyethyl) isocyanurate triacrylate (SR-368, monomer), ethoxylated (6) trimethylolpropane triacrylate (SR-499, monomer). Structures from [www.sartomer.com](http://www.sartomer.com).

In some cases, a negative-tone photoresist that is solid during fabrication can be used with MAP. When a solid photoresist, such as SU-8, is used with MAP the photoresist is prepared similarly, by mixing the photoinitiator and monomer (a full description of the components of this resin is included in the Appendix, A.7). In the case of SU-8, fluorescent dye (rhodamine) is added to the photoresist to provide a way to navigate within the photoresist during fabrication. The reason for this addition is discussed further in the Appendix (A.7).

#### 4.3.2 Sample preparation

When a liquid photoresist, such as the acrylate resin discussed above, is used for MAP the photoresist is sandwiched between two coverslips and mounted on a microscope slide (Figure 4.6). To promote adhesion of the polymerized structures to the glass coverslip, one of the coverslips is first functionalized with acrylate groups using 3-acryloxypropyl trimethoxysilane (Gelest Inc.,

Morrisville, PA). In Figure 4.6, the coverslip attached to the microscope slide is the functionalized coverslip. See the Appendix (A.10) for functionalization procedure.

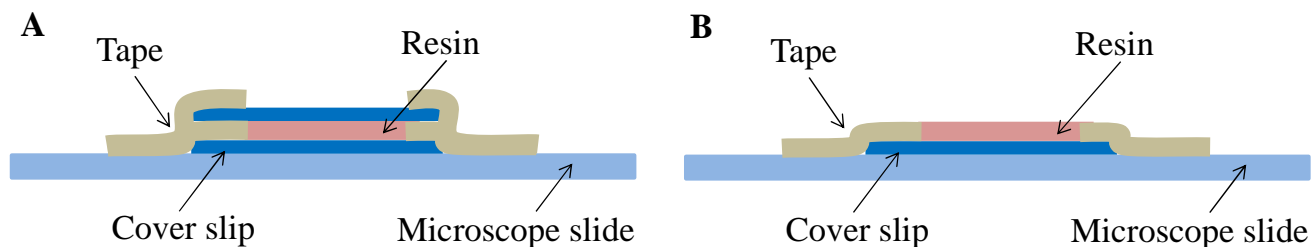


**Figure 4.6:** (A) Preparation of an acrylate resin sample for MAP fabrication. A drop of liquid acrylate resin (pink) is sandwiched between two coverslips (dark blue) using tape (tan) to define the space between them. Typically the coverslip taped to the microscope slide (light blue) is functionalized with acrylate groups before fabrication to promote adhesion between the surface and the polymerized resin. (B) Preparation of a sample of solid SU-8 resin. A drop of resin is spin-coated on a functionalized glass cover slip and taped to a microscope slide. The resin is prebaked to solidify it before fabrication. The microscope slide is used to mount the sample onto a microscope stage to allow fabrication by a focused laser beam. After fabrication, the sample is post-baked and the unexposed resin is dissolved leaving a polymer structure.

A prepared sample is mounted on a microscope stage (discussed in the following section), and the stage is translated so that the laser beam is focused within the resin. Many of the photoinitiators used with MPA, including Lucirin TPO-L, are radical photoinitiators. When a photoinitiator (P) of this type is exposed to a high intensity of light with photons of the correct energy to cause MPA, a radical polymerization reaction is initiated within the photoresist. Radical polymerization involves three primary steps: initiation, propagation, and termination (Figure 4.7). Initiation involves the creation of a radical ( $R\bullet$ ) through MPA. Propagation of the radicals causes crosslinking of the monomers (M). Termination of the propagation occurs when two nearby radicals combine.

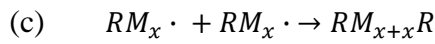
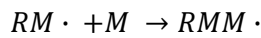
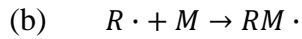
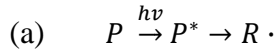


**Figure 4.7:** Radical polymerization steps. (a) Initiation. Excitation of the photoinitiator (P) creates two radicals ( $R \cdot$ ) (in the case of TPO-L). (b) Propagation. The acrylate monomers (M) form a highly crosslinked polymer network during the propagation step. (c) Termination. Two radicals combine to prevent the reaction from continuing.

To fabricate a structure via radical polymerization, the sample is mounted on a microscope stage and the stage is translated in the  $x$ ,  $y$ , and  $z$  dimensions to move the sample surface to the focal region of the laser beam. The following section discusses the different sample orientations and the fabrication process.

### 4.3.3 Experimental set-up and fabrication

Photoresist samples are prepared as described in Figure 4.6 above and are mounted on a microscope stage that is controlled in three dimensions by a LabView program. There are two sample orientations used for fabrication: inverted and upright. In Figure 4.8, the inverted set-up is depicted. This orientation is typically used with high magnifications (100 $\times$  oil-immersion objective), relatively low powers (10- to 30-mW) and low speeds (20- to 50- $\mu$ m/s). In the inverted case, the sample is mounted with the coverslip facing downward so that the focused laser beam passes through an unfunctionalized coverslip before reaching the resin. With this geometry, the microscope

objective is translated up to move the focal point of the laser beam into the resin. Before beginning fabrication in an acrylate resin, the interface between the resin and the acrylate-functionalized coverslip is identified by observing fabrication on a CCD screen. Observation is possible because the refractive index of the polymerized resin is different than that of the unpolymerized resin. Once the interface between the acrylate-functionalized glass surface and the resin is identified, fabrication is typically started slightly above this interface to make sure that the structures will be anchored to the glass. If structures are fabricated without being attached to the substrate, they will be washed away during the development step.

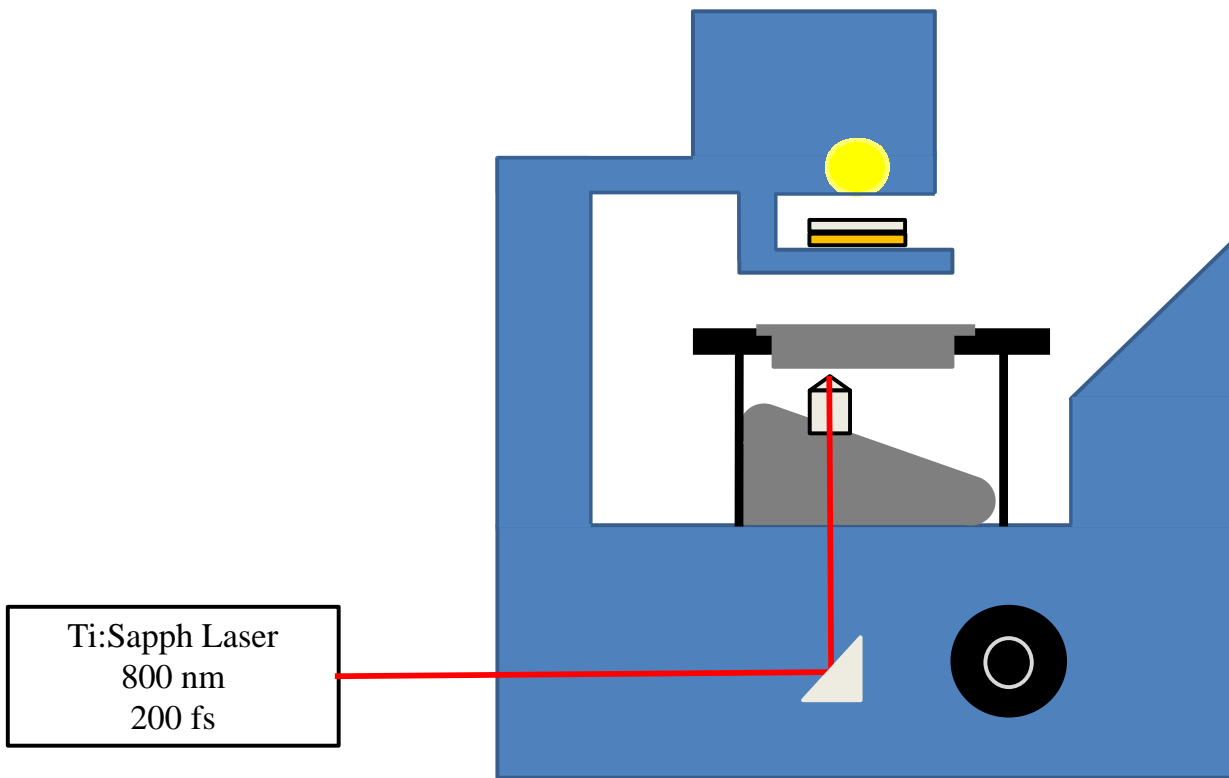


**Figure 4.8:** The inverted microscope orientation. A sample is mounted with the coverslip facing downward so that the microscope objective must be translated up to situate the focal point of the laser beam in the resin. After the microscope objective is manually translated in the  $z$  dimension, the microscope stage (and therefore the sample) is translated in the  $x$ ,  $y$ , and  $z$  dimensions to fabricate structures while the laser focal point is stationary. Typical fabrication speeds are 20 to 50  $\mu\text{m/s}$ , and typical fabrication powers are 10 to 30 mW.

With the inverted orientation, after the microscope objective is first translated in the  $z$  dimension to position the focal point of the laser beam at the resin/functionalized cover-slip interface, a LabView program reads a text file containing  $x$ ,  $y$ , and  $z$  coordinates. These coordinates are used to translate the microscope stage (and therefore the sample) in the  $x$ ,  $y$ , and  $z$  dimensions to fabricate polymer structures, while the laser focal point is held stationary. Instructions for writing programs for the inverted microscope set-up are included in the Appendix (A.11.1).

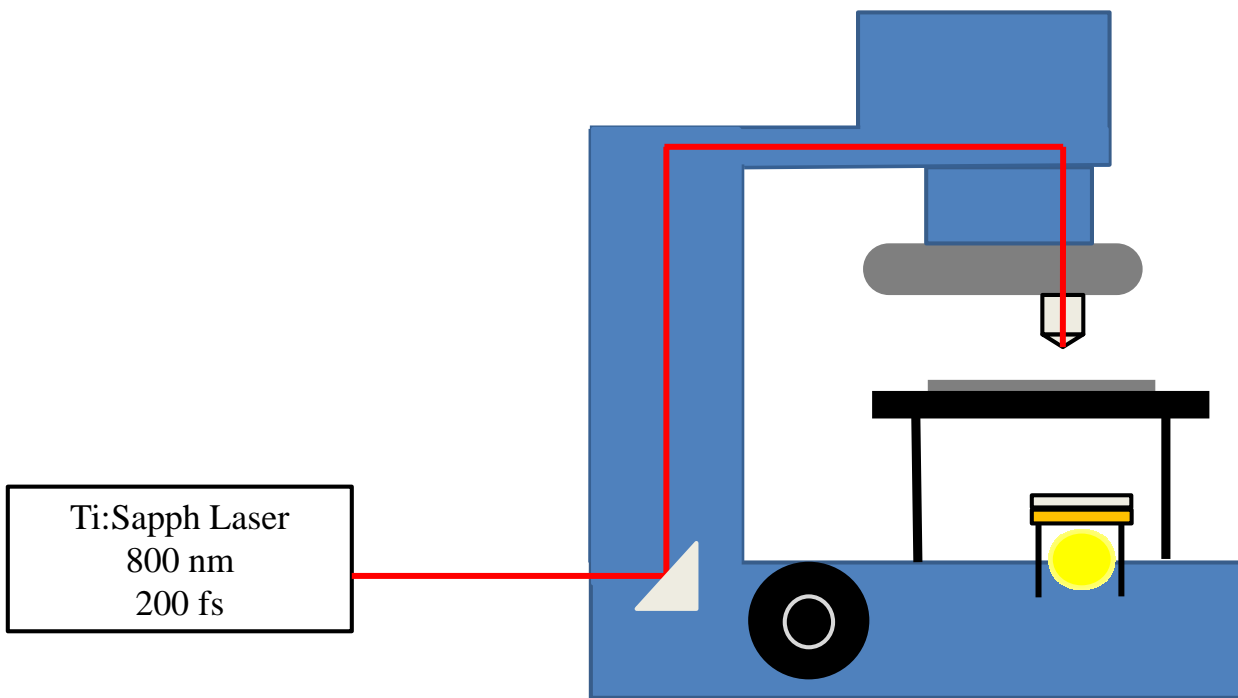


**Figure 4.9:** The upright microscope set-up. In this orientation, the sample is mounted in the opposite orientation as for the inverted microscope. The upright orientation is typically used with lower-magnification objectives, and is fitted with a stage that allows fabrication at velocities of up to 1 cm/s. At such velocities, larger structures can be fabricated in a relatively small amount of time. The typical fabrication speed is 5,000  $\mu\text{m/s}$  and typical fabrication powers are 180 to 220 mW.

The upright orientation, depicted in Figure 4.9, is typically employed for the fabrication of larger structures (approximately 0.5- to 1-cm in length). This microscope is typically used with lower-magnification objectives (10 $\times$  or 20 $\times$ ), higher powers (180- to 220-mW), and higher speeds

(up to 1 cm/s). At lower magnifications and higher speeds, larger structures (0.5-to 1-cm-long channels) can be fabricated in a few hours, the same time it would take to fabricate structures 10 to 50 times smaller with the inverted orientation. The resin/acrylate-functionalized cover slip interface is located by visualizing the sample using a CCD camera, as with the inverted set-up, and fabrication is achieved by translating the microscope stage (and therefore sample) in the  $x$ ,  $y$ , and  $z$  dimensions. The main difference between these two orientations is that in the case of the upright orientation, the stage, instead of the microscope objective, is translated upward to locate the interface initially.

#### 4.3.4 Laser table and optics

For the fabrication discussed above, a Ti:Sapphire ultrafast pulsed laser is tuned to 800 nm, mode-locked, and directed through a series of optics to the microscope, as shown in Figures 4.10 and 4.11. Figures 4.10 and 4.11 are schematics of the optical elements that are movable and can be adjusted to align the laser beam into the microscope. The Appendix (A.8) includes detailed information describing laser alignment procedures separated into those performed before each experiment and those performed less often (as needed, in approximately 1- to 3-month intervals).

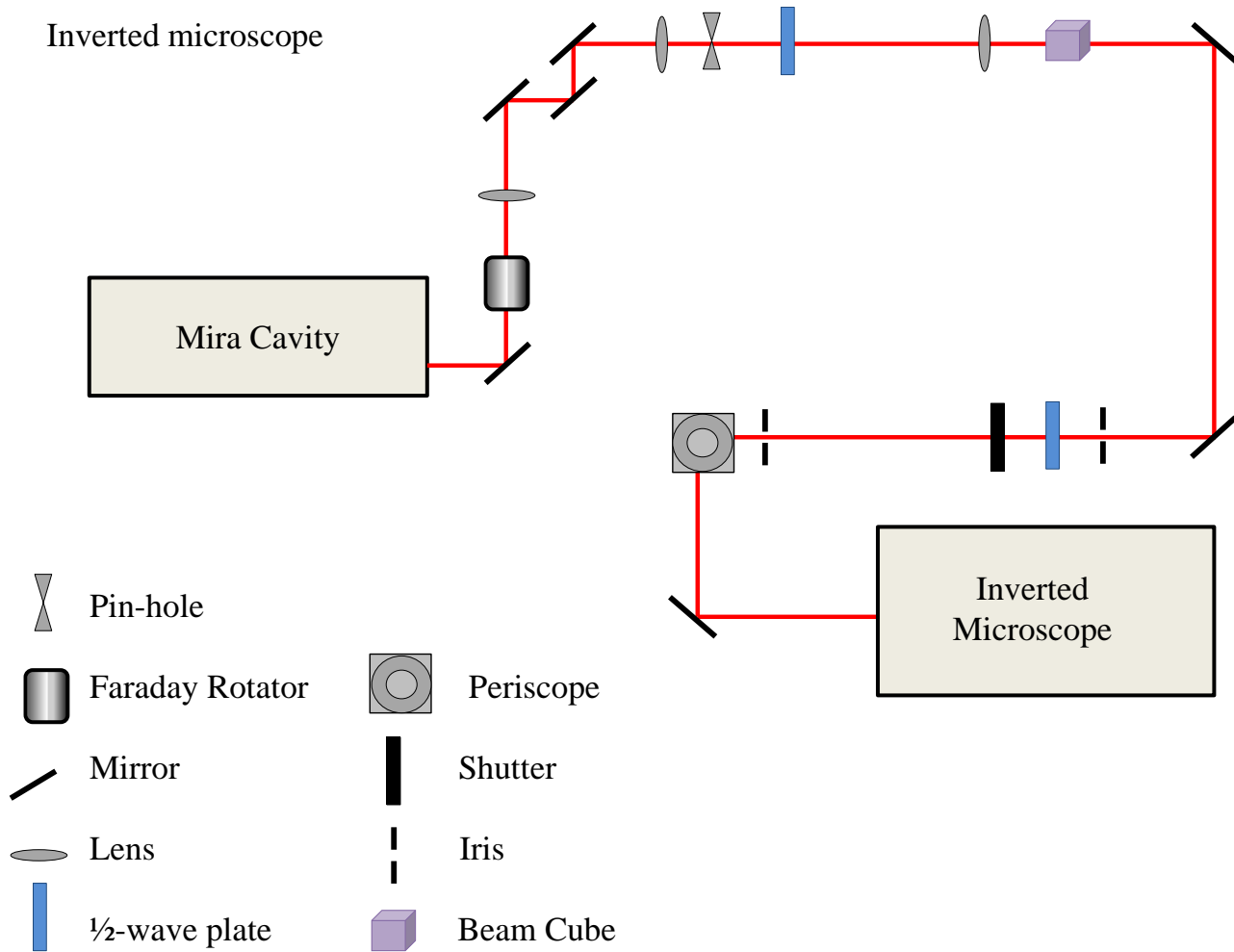


**Figure 4.10:** The beam path from the Mira cavity to the inverted microscope. A diagram of the inverted microscope is included in Figure 4.7. A summary of the alignment procedure is included in the Appendix (A.8).

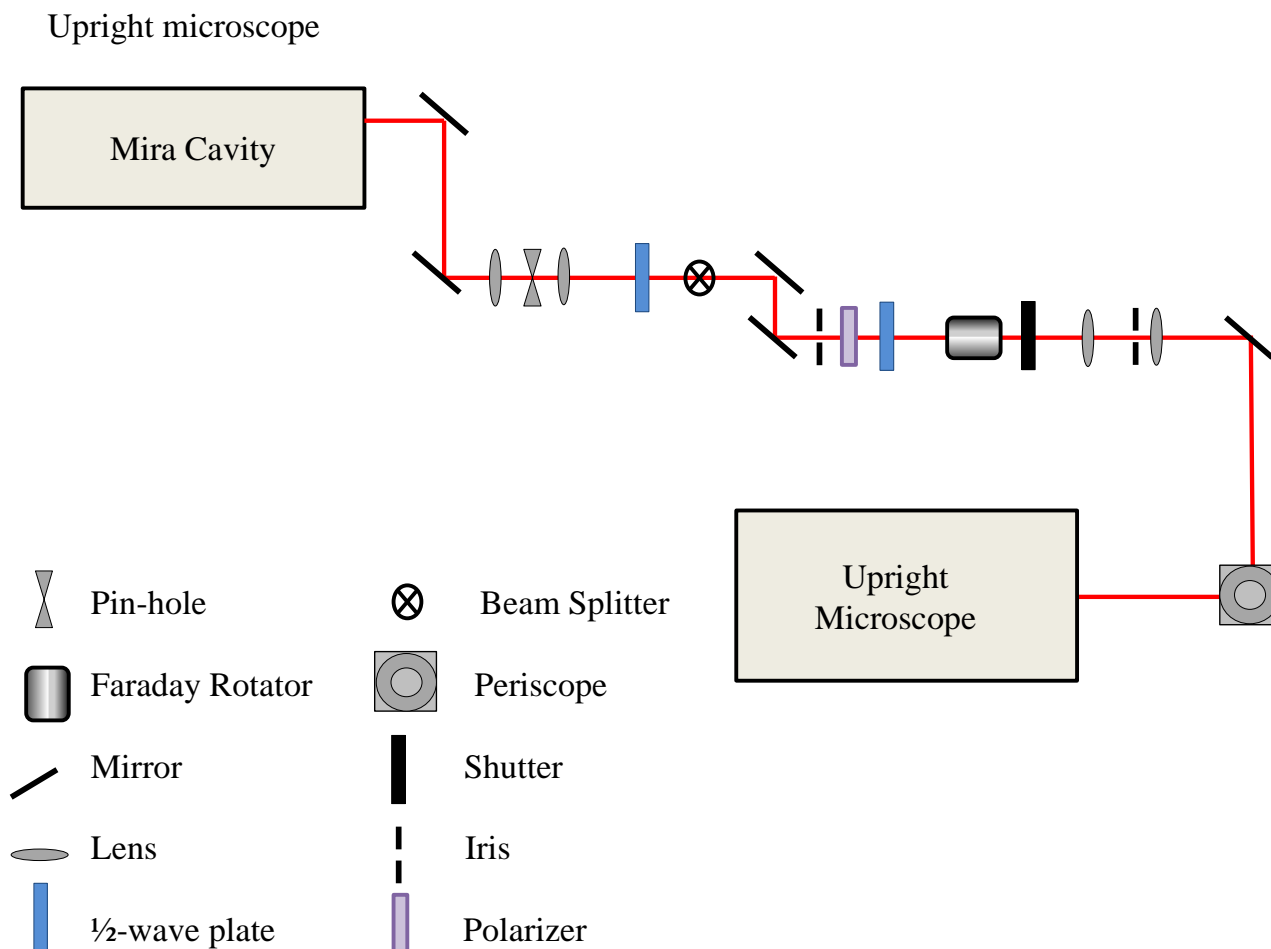


**Figure 4.11:** The beam path from the Mira cavity to the upright microscope. A diagram of the upright microscope is included in Figure 4.8. A summary of the alignment procedure is included in the Appendix (A.8).

#### 4.4 Microfluidic devices: fabrication and molding

Structures fabricated with MAP for replication are referred to as “master structures”. Master structures can typically be replicated several times through a molding process depicted in Figure 4.12. After a structure is fabricated, unpolymerized resin is washed away by rinsing for three minutes each in two beakers of dimethylformamide (DMF) and two beakers of ethanol (EtOH). In this context, rinsing involves placing the functionalized coverslip structure-side-down (leaning on the side of the beaker) in a 30 ml beaker filled with approximately 20 ml of solvent. The structure is then rinsed for

one minute in hexane and dried in a 95°C oven to ensure polymerization throughout the entire structure. This process is referred to as “development” in the following sections.

After development, the master structure is examined under an optical microscope to make sure that no part of the structure has been damaged or washed away during the development process. When a master structure has been developed and determined to be intact and ready for molding, it is either molded directly with PDMS, or a coating process can be performed to prevent the elastomeric molding material from sticking to the acrylate structure. The two methods of anti-stick coating application that are commonly employed are solution coating, which aims to create a covalent bond between unreacted acrylate molecules on the surface of the master structure, and vacuum coating, which deposits a layer of anti-stick coating on the entire surface of the master structure by placing it in a desiccator with a small volume (< 1 mL) of a silane solution and evacuating the desiccator. The details of these procedures are included in the Appendix (A.12). The desiccator method of coating has been determined to work better when molding with PDMS. It is crucial that the master structure is not left in the desiccator with the silane solution for longer than 30 minutes, to prevent too much material from being deposited on the surface, as over-deposition inhibits the curing process of the PDMS.

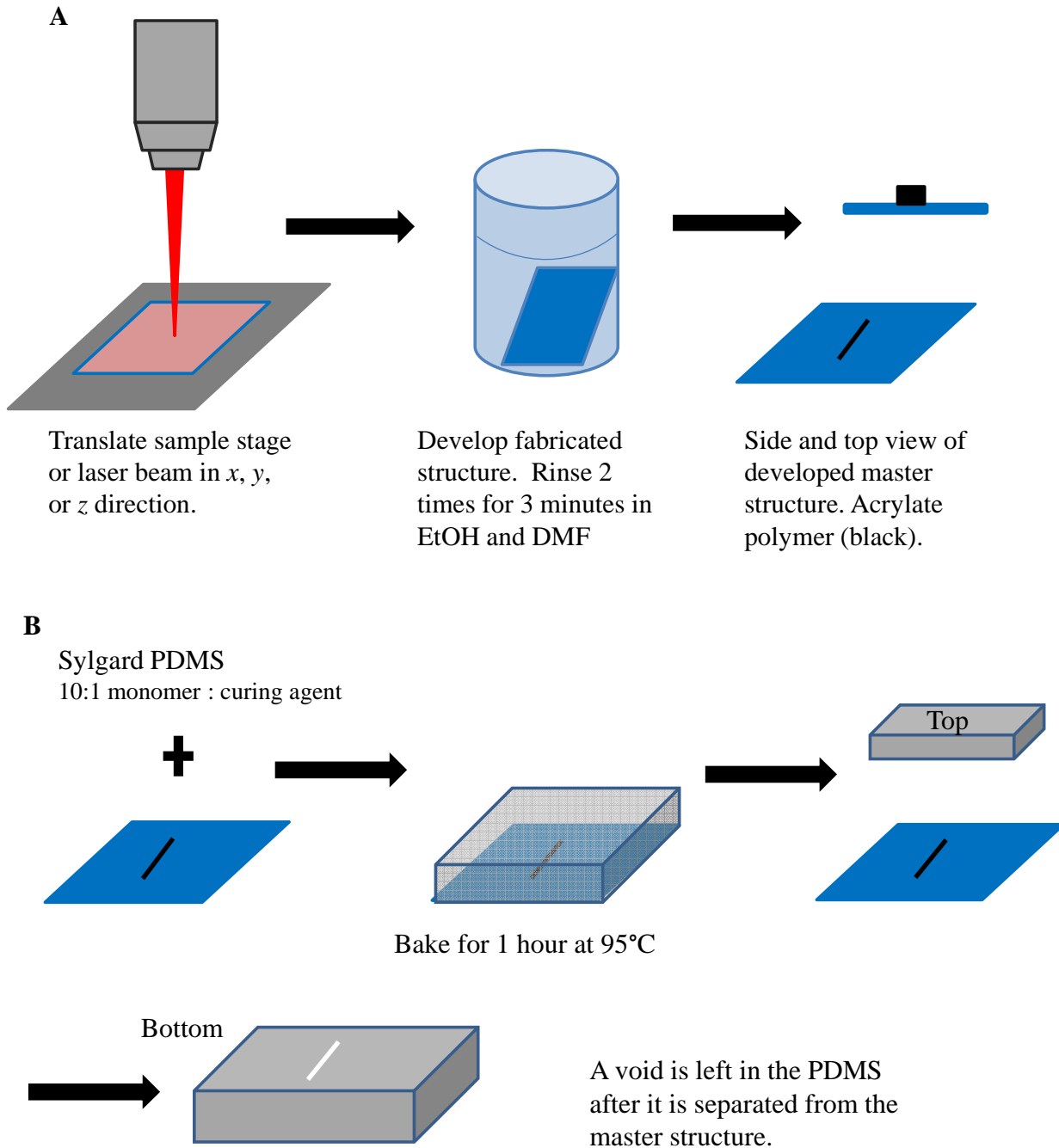


**Figure 4.12:** (A) After a structure is fabricated by MAP (left) it is developed to remove unexposed resin (center), and treated by either baking or coating. In the case of microfluidics, baking and coating steps are performed to condition the master structure for use as a mold. (B) PDMS is mixed, degassed, poured on top of a master structure, and baked at  $95^{\circ}\text{C}$  for 1 hour to polymerize. The cured PDMS is peeled away from the glass coverslip, and a void in the shape of the acrylate structure is left in the cured PDMS.

A master structure that is ready to be molded is situated in a foil boat (Figure 4.12, foil boat not pictured) or other vessel to contain the molding material. The PDMS molding material is prepared in a 10:1 by weight ratio of monomer to curing agent, and is degassed by placing it inside a desiccator and attaching the desiccator to a vacuum line. The degassed PDMS is poured over the master structure, being careful to avoid capturing air bubbles in the PDMS, and baked at 60 to 90°C for 30- to 120-minutes. The baking temperature and time depend on the thickness of the PDMS layer. Typically a 4-mm-thick layer is baked at 90°C for 1 hour. After baking, the PDMS is carefully peeled off of the glass coverslip. The master structure and PDMS mold are then examined under an optical microscope. Occasionally, some parts of the master structure will be peeled off of the glass coverslip and will stick in the PDMS mold, damaging the master structure. However, the acrylate pieces can be removed from the mold with tweezers. A replica of the master structure can be created for SEM imaging by dropping resin on the PDMS mold and using a UV light source to polymerize the resin. This process will be discussed further below.

To fabricate master structures that can be molded to create functional microfluidic devices, multiple fabrication steps and/or fabrication programs may be combined to achieve a set of channels with the desired connectivity and dimensions. In Figure 4.13, SEM images of representative microfluidic master structures are shown. To control the width and height of the fabricated structure, the number of fabricated lines in the vertical and horizontal direction is adjusted. For example, to fabricate a channel with a square cross section, more lines would be fabricated in the  $xy$  plane than in the  $z$  dimension to compensate for the oblong shape of the fabrication voxel. Similar considerations can be given to fabricate channels of various cross sections, such as those shown in Figure 4.14. It has been demonstrated that channels with arbitrary cross sections can be fabricated (with MAP) and molded with PDMS to create microfluidic channels that have the potential to be used to study flow

profiles of fluid, create differential mixing zones, and mimic the flow environment in capillary environments.<sup>73</sup>

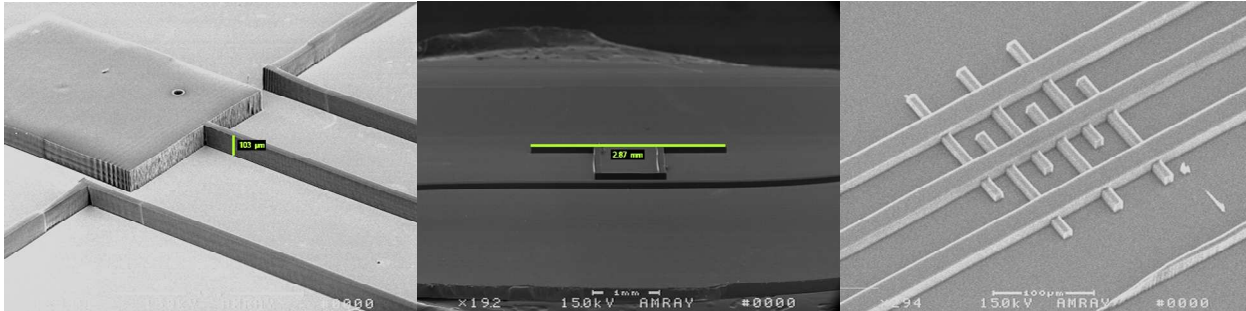


**Figure 4.13:** SEM images of representative master structures fabricated with MAP for use as molds to create microfluidic devices.

In the case of structures fabricated with the upright microscope, the length of a structure is determined by specifying the fabrication speed and the amount of time the shutter is open and allowing the laser to come into contact with the photoresist. When a program is written, the coordinates specify the fabrication distance, and the fabrication time entered into the LabView program is determined based on the fabrication speed. The high speed typically used for larger-channel master structures requires a certain amount of acceleration time before the stage is moving at the desired velocity. This amount of time is incorporated into the total fabrication distance. However, the laser shutter remains closed during acceleration so that no polymer is created. A typical acceleration time for a fabrication velocity of 5,000  $\mu\text{m/s}$  is 350 ms, which corresponds to a distance of 1000  $\mu\text{m}$  added to the total fabrication distance. These values are experimentally determined for each fabrication speed. If the acceleration time and distance of the stage are not considered, the dimensions of a fabricated structure are likely to be different than what is expected based on the coordinates written in the fabrication text file. For example, if the stage has not accelerated to the maximum velocity when fabrication begins, the total distance the stage travels in a

given amount of time will be smaller than expected. This phenomenon can be a problem when corners or intersections are being fabricated (example in Figure 4.13).

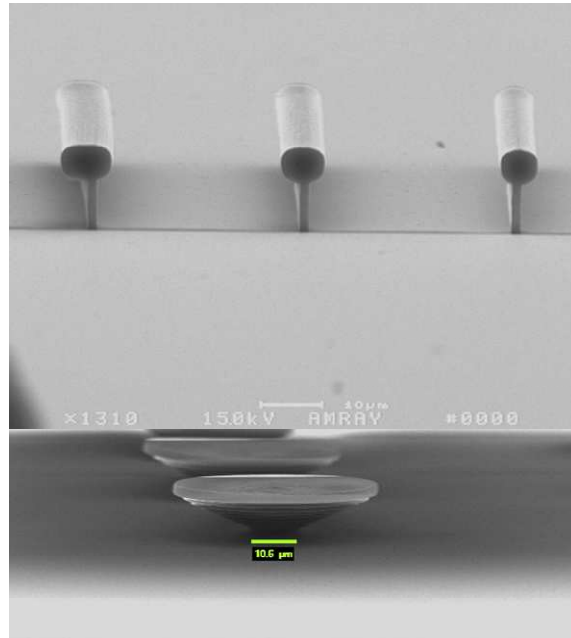


**Figure 4.14:** Various structures fabricated with the inverted microscope: (A) channels with circular cross-sections (with membranes) and (B) cell traps.

Creating channels with smaller cross sections ( $<10 \mu\text{m}$ ) requires a higher-magnification objective (100 $\times$  oil immersion objective) and slower speed. Circular structures of 5 to 10  $\mu\text{m}$  in diameter (Figure 4.14) can be fabricated with MAP using a LabView program (elliptical block) that compensates for the oblong shape of the voxel. This program fabricates layers with different widths in the  $xy$  plane to create a circular shape. Further details of this program are included in the Appendix (A.13). Figure 4.14 includes an SEM image of a structure that resembles an inverted cone that was developed to be molded to create a cell trap. The cell trap would allow the interaction between two cells to be investigated through the PDMS molding material. This structure is also circular, but instead of layers, concentric circles are fabricated in the  $xy$  plane. These two structures demonstrate the ability to use MAP to fabricate structures with circular cross-sections in different planes.

After a master structure has been successfully molded with PDMS, it can be used to create replicas of the master structure (Figure 4.15A), or it can be sealed to create closed microfluidic channels (Figure 4.15B). In Figure 4.15A, a scheme for replication of a mold is shown. A drop of the same acrylate resin used for MAP fabrication is placed on the PDMS mold, and an acrylate-functionalized coverslip is pressed onto the top. Next, the PDMS mold and acrylate-functionalized coverslip sandwich is placed under a UV light source (BLAK-RAY 365 nm long wave-UV-lamp, 100 W, Upland, CA) for 40 seconds to 2 minutes to polymerize the resin. The use of an acrylate-functionalized coverslip ensures adhesion of the polymerized resin to the coverslip. After polymerization, the coverslip is peeled away from the PDMS mold, and examined under an optical microscope to confirm successful replication. Replicas of microfluidic-channel master structures are typically used for SEM imaging to gain information about the channel measurements.

In Figure 4.15B, the process for sealing a PDMS mold for use as a microfluidic device is depicted. First, the PDMS mold is trimmed and holes are punched to create reservoirs, or to provide ports for the connection of tubing after the device is sealed. Next, several pieces of Scotch tape are used to clean dust and debris from the surface of the PDMS mold, and ethanol is used to clean a glass coverslip. The two clean pieces are plasma cleaned, and the PDMS mold is placed on top of the coverslip, and baked at 95°C for 10 to 20 minutes to promote adhesion.

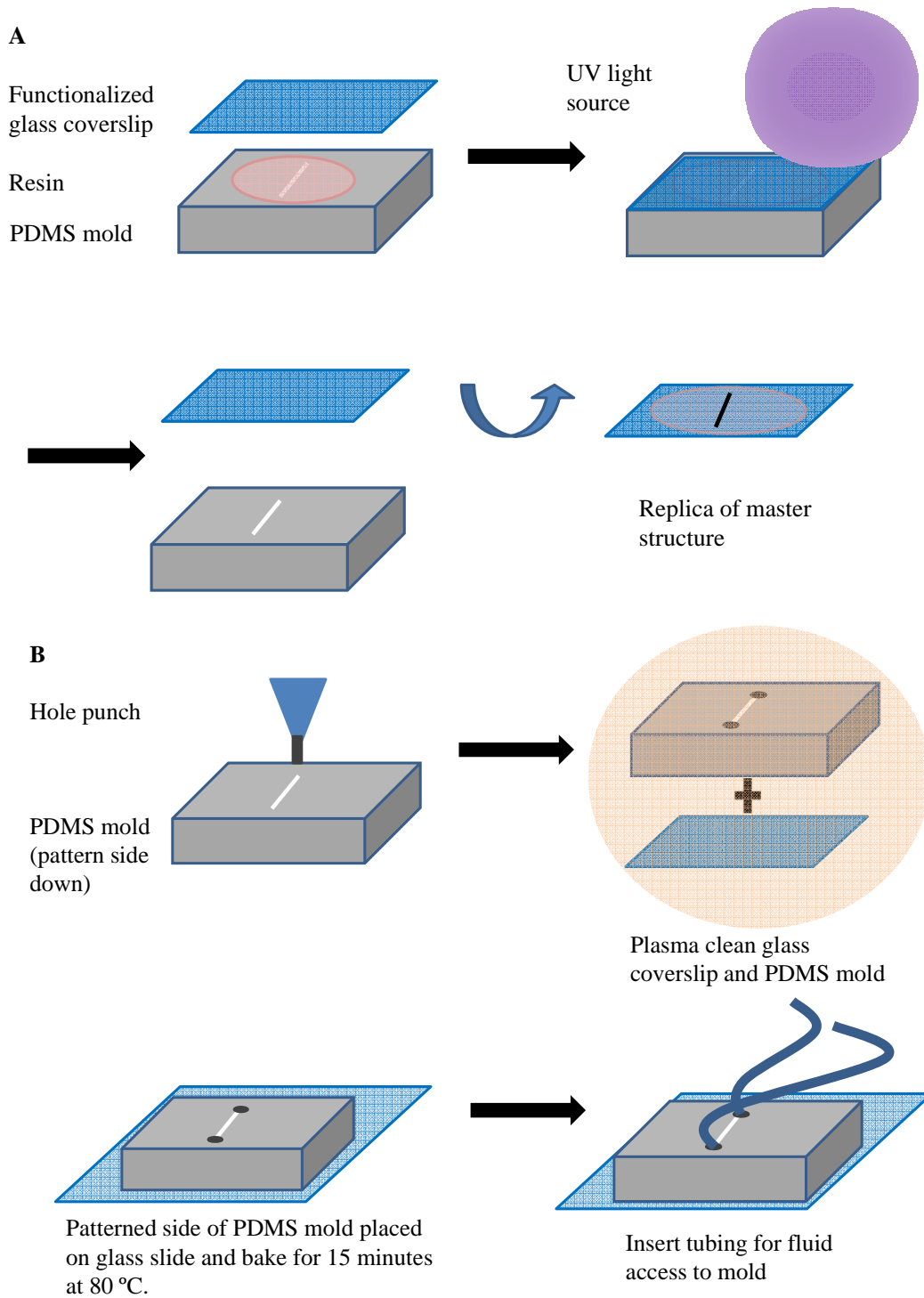


**Figure 4.15:** (a) Process for the replication of a master structure from a PDMS mold. (b) Creating a microfluidic device from a PDMS mold of a master structure.

#### 4.5 Conclusion

The 3-D fabrication capabilities of MAP have been exploited to create structures with circular cross-sections that can be integrated into microfluidic device master structures. Circular cross-sections are beneficial because they provide the ability to mimic the fluid environment in capillaries, which are commonly used in microfluidic devices. The following chapter will discuss PDMS microfluidic devices created from MAP fabricated master structures and their use to study the relationship between channel length and resolution with GEMBE.

## Chapter 5: MAP-fabrication of GEMBE devices

### 5.1 Introduction

This Chapter discusses the MAP fabrication of master structures that can be molded with PDMS to make microfluidic devices. The devices discussed in the following sections were designed with the goal of creating a device geometry similar to that of the GEMBE device discussed in Chapters 2 and 3. As with that device, simplification in all aspects of the channel fabrication, assembly, and operation was a motivating factor. The PDMS devices have been developed to allow GEMBE to be performed with shorter separation channels than the previous fabrication method allows (2- to 3-mm) to investigate the change in step width and resolution as channel length is decreased.

### 5.2 Experimental

#### 5.2.1 Chemicals and reagents

All solutions were prepared with deionized (DI) water (18.2-M $\Omega$ •cm, Barnsted Easypure II ultrapure water system). Stock solutions of 1-mmol/L sodium chloride (NaCl), sodium sulfate (Na<sub>2</sub>SO<sub>4</sub>), and potassium nitrate (KNO<sub>3</sub>) were prepared by dissolving the solid salts in deionized water or run buffer. The run buffer was 100 mM bis-tris (2-[Bis(2-hydroxyethyl)amino]-2-(hydroxymethyl)-1,3-propanediol) and 100 mM HEPES (4-(2-hydroxyethyl)-1-piperazineethanesulfonic acid) prepared by dissolving solid bis-tris and HEPES in DI water. All chemicals involved in the MAP fabrication process were the same as previously described (Chapter 4).

### 5.2.2 Device fabrication and set-up

The GEMBE device discussed here was molded with PDMS from a master structure fabricated with MAP (Figures 4.12 and 4.15), as described in Chapter 4. Figure 5.1 is a group of SEM images of MAP-fabricated master structures of the various channel orientations that were investigated. For all of the channel designs, the goal was to maintain a simple geometry that closely followed the orientation of the GEMBE device described in Chapter 2 (Figure 2.1). Key components of the device design include a buffer reservoir that can be rinsed after each separation and that can be connected to the high-voltage power supply and pressure control, a sample reservoir that can be accessed with a pipette for sample exchange, and a separation channel with a circular cross-section.

The large “reservoir” channels were fabricated with the upright microscope set-up (Figure 4.9) and the circular-cross-section separation channels were fabricated with the inverted microscope set-up (Figure 4.8). To fabricate one master structure using two different microscopes the separation channel was fabricated first, close to the center of the sample on the inverted microscope. The sample was then removed, and the location of fabrication (indicated by oil remaining from the use of an oil-immersion objective) was marked on the glass slide supporting the sample. The sample was then placed on the upright microscope stage and the CCD screen was used to visualize the sample so that the reservoir channels could be fabricated in the desired location with respect to the separation channel.

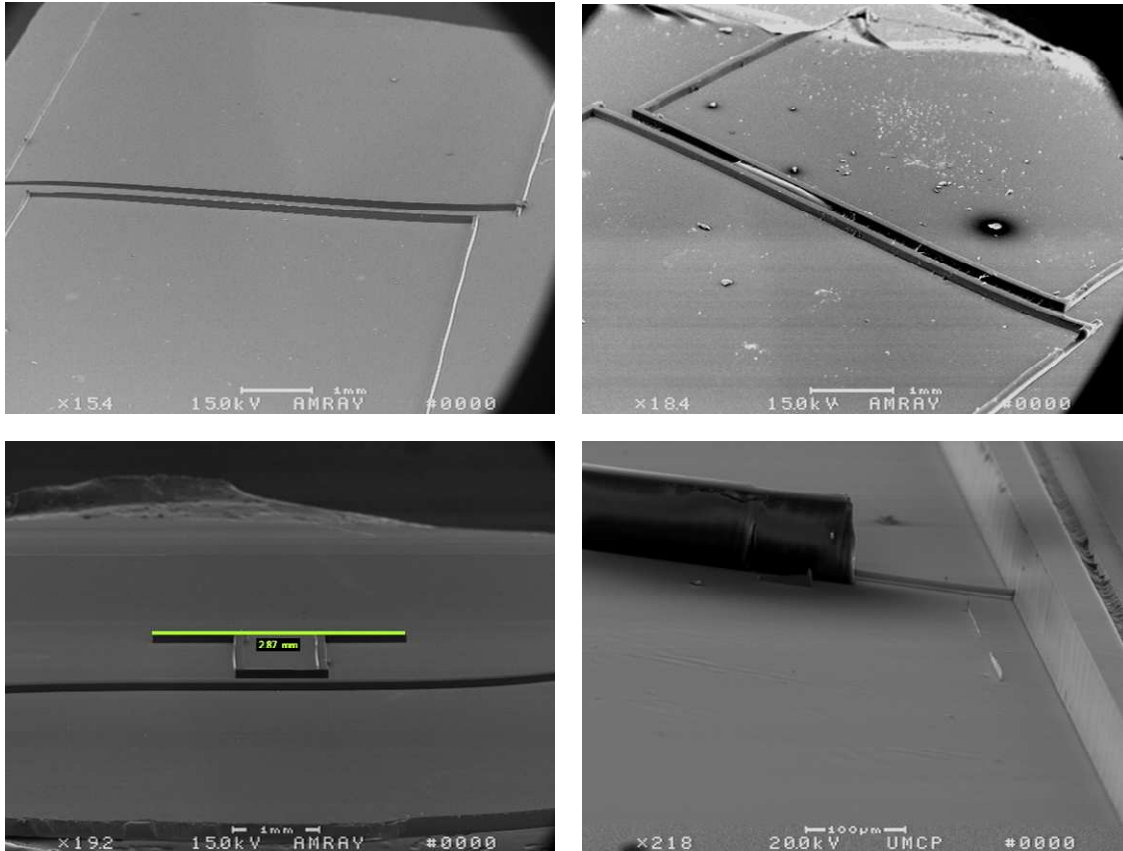


**Figure 5.1:** SEM images of MAP-fabricated master structures that were molded and investigated for their ability to perform GEMBE separations.

Frequently, after the devices were molded with PDMS, some PDMS remained stuck between two closely oriented channels (Figure 5.1 B). As the separation channel was shortened, this effect occurred more often requiring cleaning of the master structure and re-molding or, in some cases, fabrication of a new master structure. To avoid this problem, the channel orientation was adjusted to the T-shaped geometry shown in Figure 5.2. The results presented in the following sections were collected using devices with the T-shaped reservoir channel geometry. After a PMDS mold was made, the integrity of the mold (how well it has replicated the master structure) could be determined by cutting the mold in various places to allow imaging of channel cross-sections. SEM imaging of channel cross-sections also allows the dimensions of each channel to be determined.

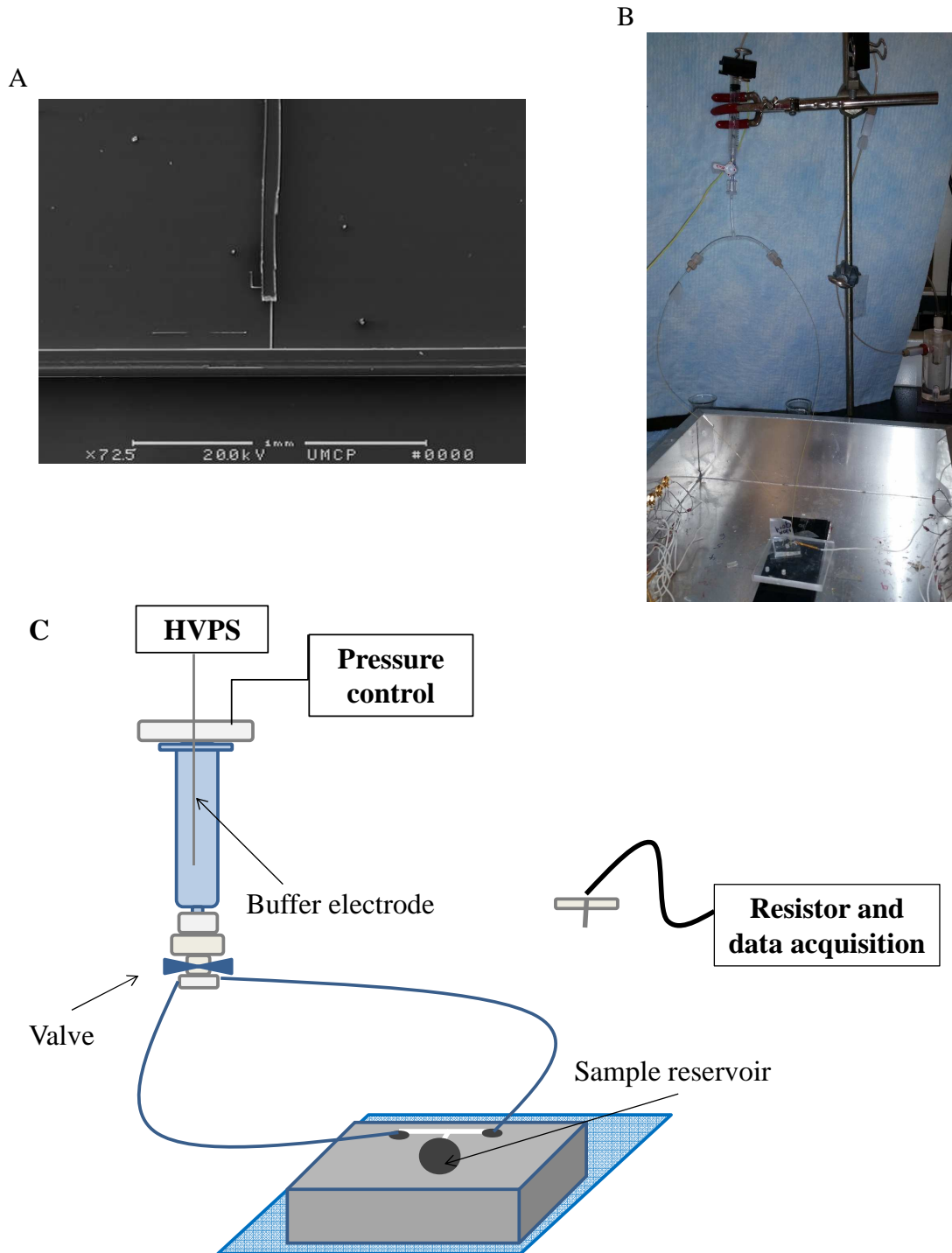


**Figure 5.2:** (A) SEM image of a MAP-fabricated master structure with a t-shaped channel orientation. The horizontal channel of the “T” is the buffer reservoir channel and the vertical channel is the sample reservoir channel. (B) Photograph of the assembled PDMS-GEMBE microfluidic device. (C) Schematic of (B) with labeled reservoirs.

The larger reservoir channels were easily measured (approximately 4 cm long and 75  $\mu\text{m}$  in height and width) by cutting the PDMS mold so that the channel cross-section was visible. Cutting the PDMS mold to measure the cross-section of the separation channel was more difficult because of its short length and small diameter, however, the mold could be cut using an optical microscope, straight-edge razor, and buffer reservoir channel as a guide. SEM images of the PDMS mold of the separation channel are necessary to determine channel dimensions and to ensure that the membrane supporting the circular channel has sealed. Figure 5.3 shows SEM images of separation channels with membranes that did not seal (5.3A and 5.3B) and with membranes that did seal (5.3C and 5.3D). For reference, the larger grooves visible in 5.3 A are the reservoir channels.

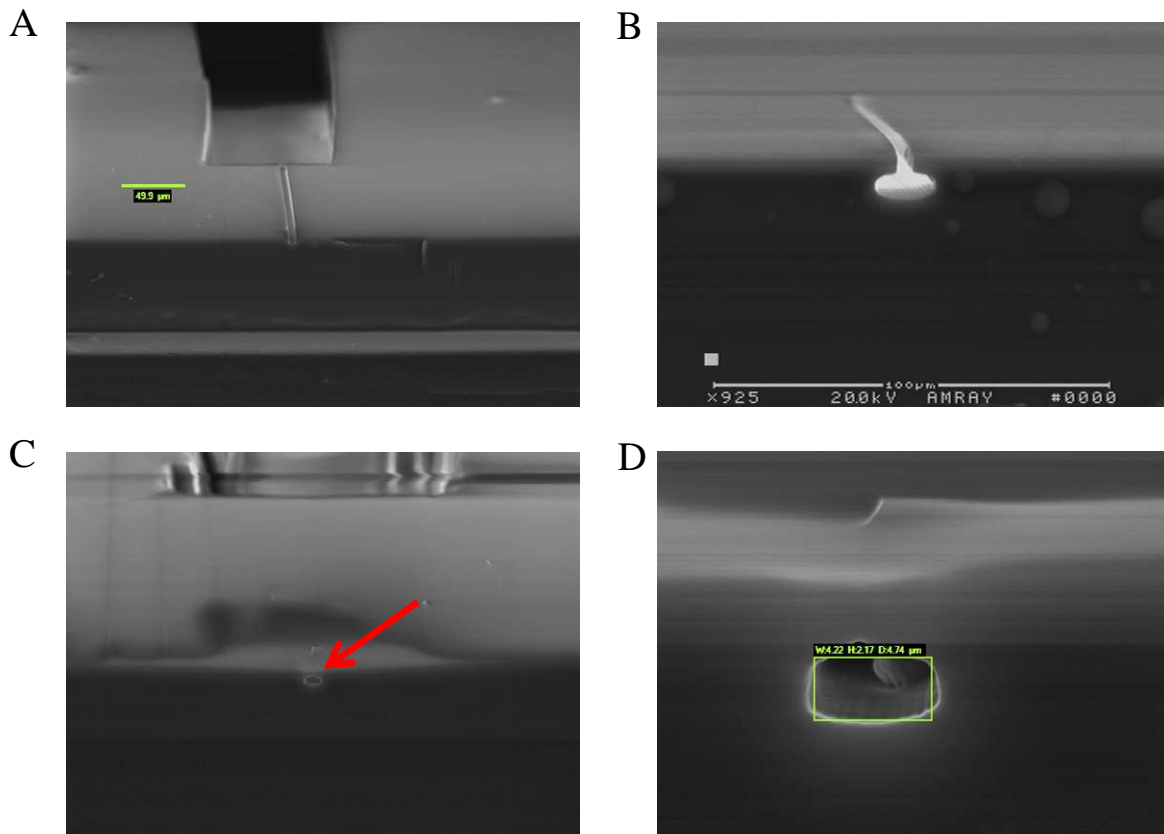


**Figure 5.3:** SEM images of (A) and (B) circular channels with membranes that did not close after the PDMS mold was removed from the MAP-fabricated master structure and (C) and (D) circular channels with membranes that did close. In (C) a red arrow is pointing to the channel cross section that is shown larger in (D).

A membrane may not seal if the fabrication stage is not flat, if the membrane is too thick in comparison to the channel dimensions, or if the membrane is not tall enough. Ideal membrane dimensions for a channel with a 5- to 7- $\mu\text{m}$  diameter are approximately 2  $\mu\text{m}$  wide and 5- to 10- $\mu\text{m}$  tall. If the membrane is wider than approximately 2  $\mu\text{m}$ , the PDMS mold remains open, as in Figures 5.3 A and B. A membrane that is too tall will fall over or become “wiggly” as shown in Figures 5.4 A and B, respectively. In all three images in Figure 5.4, the channels are of the same width, and the membrane height decreases from left to right.

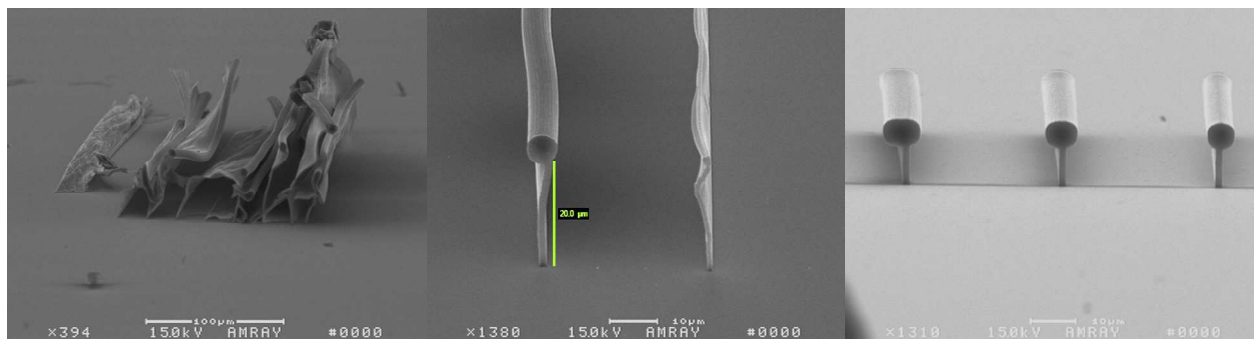


**Figure 5.4:** SEM images of MAP-fabricated master structures of circular channels with membranes. In (A) the channels have fallen over because the membranes are too tall and in (B) the membranes are “wiggly” and the channels are unstable and in (C) the membranes and channels are stable and can be molded to create a sealed PDMS microfluidic separation channel.

### 5.2.3 Device assembly and data collection

The photograph and schematic in Figure 5.2 depict the PDMS-GEMBE device used to collect the data presented below. To prepare the PDMS device, the basic procedure outlined in Figure 4.14 was followed. A 360- $\mu\text{m}$  hole punch was used to punch access ports on either end of the buffer channel, and a 2- to 3-mm hole punch was used to punch a sample reservoir in the PDMS. All holes were punched while observing the PDMS under an optical microscope. The sample reservoir placement was important to ensure that the sample was in contact with the separation channel. If too much of the sample reservoir channel remained between the separation channel and sample reservoir, sample often was not able to be completely rinsed from the channel. Figure 5.5 shows incorrect (Figure 5.5 A) and correct (Figure 5.5 B) placement of the sample reservoir. After punching buffer and sample reservoirs and plasma bonding the PDMS mold to a glass coverslip, the PDMS mold was again observed under an optical microscope to check for debris or incomplete bonding between the PDMS and glass.

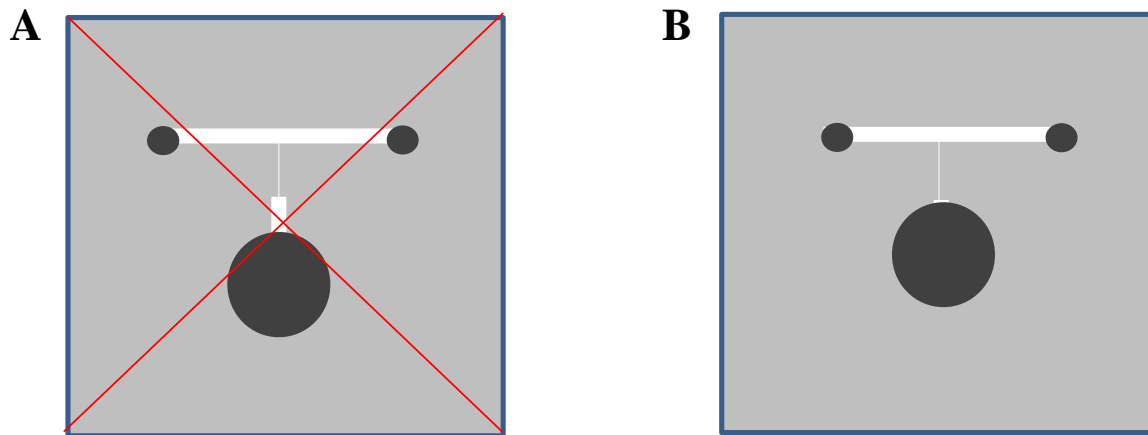


**Figure 5.5:** A top-view schematic of the T-shaped PDMS-GEMBE device with (A) incorrect placement of the sample reservoir and (B) correct placement of the sample reservoir.

A device that was determined to be plasma bonded successfully was then attached to external pressure and voltage control. The buffer reservoir consisted of a polypropylene syringe (Figure 5.2 C) identical to the one discussed in Chapter 2, except with a smaller total volume. A valve was connected to the end of the syringe and two fittings were secured to the valve to allow coupling of PEEK tubing (OD: 360  $\mu\text{m}$ , ID 75- to 150- $\mu\text{m}$ , Upchurch). The buffer syringe was filled with run buffer and the pressure was turned on to 10,000 Pa to fill the valve and PEEK tubing. When run buffer droplets were observed at the end of the PEEK tubing, the pressure was decreased to 2,000 Pa and one side of tubing was connected to one side of the buffer reservoir channel. If the buffer syringe was filled and the buffer needed to be replaced (with fresh buffer or a new buffer entirely), tubing was removed from the PDMS device and excess buffer was pipetted out of the syringe to leave 0.2 to 0.5 mL. The new buffer was added in 1 mL aliquots and rinsed through the syringe, valve, and PEEK tubing at 10,000 Pa for a total of 4 mL.

The pressure was held at 2,000 Pa with PEEK tubing attached to one side of the buffer channel until a bead of buffer was visible on the other side. To rinse the buffer channel, a bead of

buffer was allowed to exit one side of the buffer reservoir channel. This process was often repeated between separations of high concentration analytes, or if the measured current baseline decreased (suggesting the presence of an air bubble). After a bead of buffer was visible, PEEK tubing was connected to the second port on the buffer channel. The pressure was held at 2,000 Pa for approximately 10 minutes, and was increased in 2,000 Pa intervals to a maximum of 20,000 Pa. An abrupt increase in pressure from 2,000 Pa to 20,000 Pa typically separated the PDMS from the glass coverslip, as indicated by a sharp increase in the current measured across the device, visible leaking at the glass/PDMS interface, or overflowing of the sample reservoir.

To confirm that the device was filled with run buffer, the sample reservoir was filled with 15 to 20  $\mu\text{L}$  of run buffer and the sample electrode was placed in the reservoir. The voltage was turned on (typically between 50 V and 150 V) and the pressure was set to 2,000 Pa. The current was monitored for 10 minutes (by turning the applied voltage on and off) while adjusting the pressure by 2,000 Pa increments. If a constant current was not maintained during pressure adjustments, the device was examined for leaks, and/or allowed to rinse at 10,000 Pa for a longer amount of time. This step in the device preparation also provided an indication of a separation channel with a membrane that was not sealed at all or only partially sealed. A higher applied pressure resulting in an increased current measurement, but no leaks, was indicative of a membrane that was open at higher pressures, but closed at lower pressures. This behavior was confirmed by SEM images of PDMS devices with partially sealed membranes.

When a constant current was measured, at high (20,000 to 30,000 Pa) and low (2,000 to 6,000 Pa) pressures, separations were performed first with run buffer, and then with sample. Samples were introduced at concentrations from 200  $\mu\text{mol/L}$  to 3  $\text{mmol/L}$  to identify step locations. Initial

separations were performed at the same accelerations (-100 Pa/s) used for the GEMBE device described in Chapters 2 and 3 to identify an elution pressure, and then slower accelerations were used (-2 Pa/s to -10 Pa/s). The ratio of PDMS monomer to curing agent was adjusted from 15:1 to 2:1 to determine if the integrity of the PDMS-glass plasma bond would be affected. Improvement was monitored based on the maximum pressure that the device was able to withstand before delamination occurred, and the length of time that lower pressure (1,000 to 10,000 Pa) could be applied to the device before leaks were observed. No reproducible improvement was obtained by altering the PDMS mixing ratio, so a 10:1 monomer to curing agent ratio was used.

### 5.3 Results and discussion

The species of interest are NaCl, Na<sub>2</sub>SO<sub>4</sub>, and KNO<sub>3</sub> and the anions of interest are Cl<sup>-</sup>, SO<sub>4</sub><sup>2-</sup>, and NO<sub>3</sub><sup>-</sup>. Figures 5.6 and 5.7 show separations of a sample of 1 mmol/L Cl<sup>-</sup>, SO<sub>4</sub><sup>2-</sup>, and NO<sub>3</sub><sup>-</sup>. With most devices, the pressure required for GEMBE analysis could only be sustained for 3 to 6 hours. The acceleration required to begin to resolve the three anions (Cl<sup>-</sup>, SO<sub>4</sub><sup>2-</sup>, and NO<sub>3</sub><sup>-</sup>) is indicated in Figure 5.6. At an acceleration of -2.5 Pa/s, a separation over a wide range of pressures can take up to 1 hour. Unfortunately, the long time required to locate analyte elution pressures often caused the PDMS mold to separate from the glass coverslip, and the device had to be replaced.

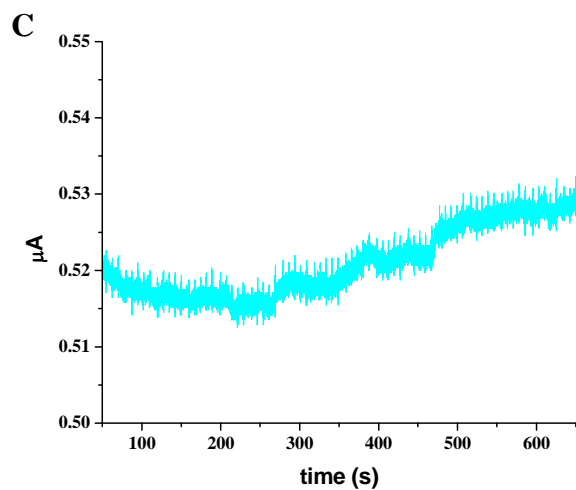
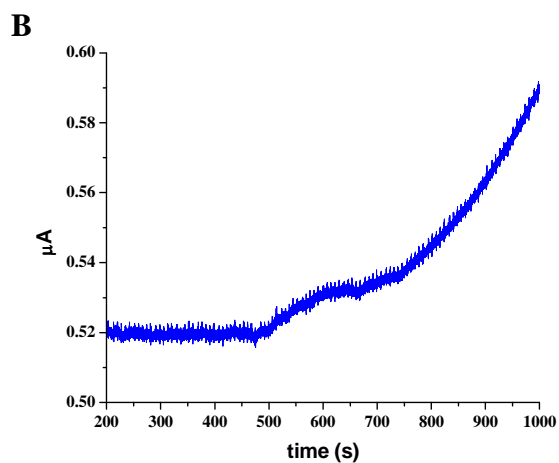
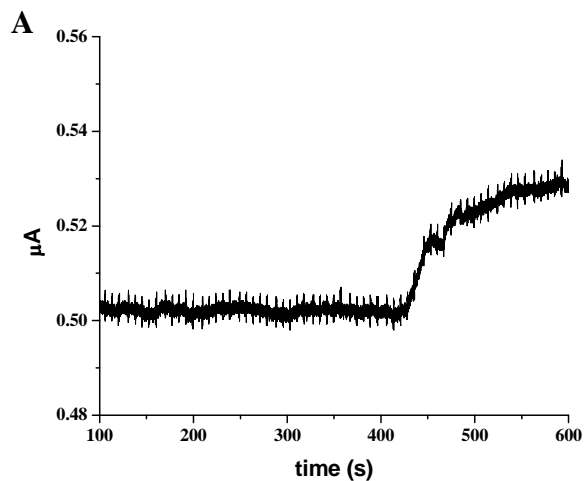
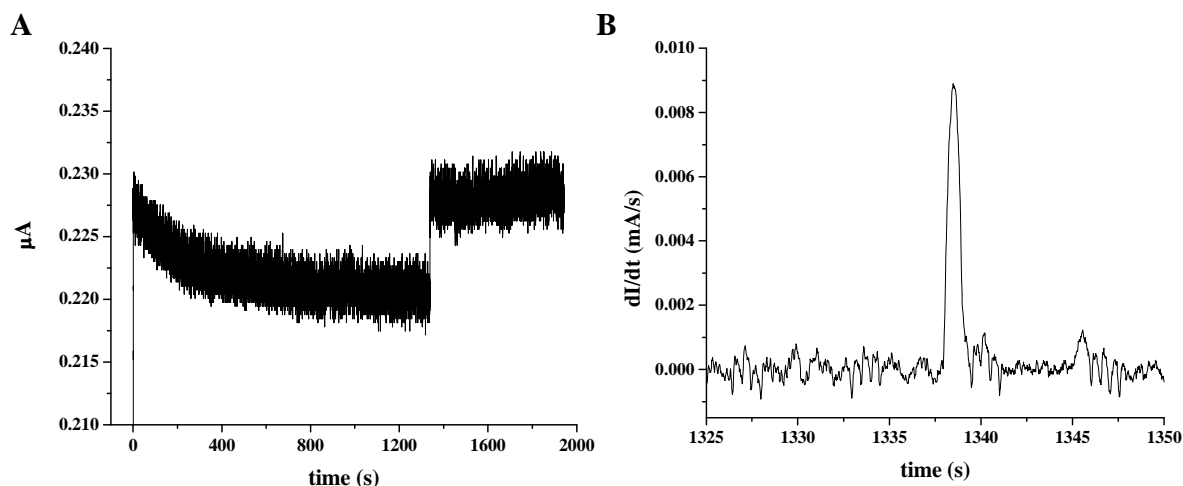


**Figure 5.6:** Separations of  $1\text{ mmol/L Cl}^-$ ,  $\text{SO}_4^{2-}$ , and  $\text{NO}_3^-$  at three counter-flow accelerations. As the acceleration is decreased, the resolution between analyte steps increases.

The most promising data that were collected from a PDMS GEMBE device are shown in Figure 5.7. These data were collected using a device with a sample reservoir punched as depicted in Figure 5.5B, and plasma cleaned before it was filled with run buffer. The device used to collect the data shown in Figure 5.7 held pressure up to 40,000 Pa for about 4 hours, or a total of 3 to 9 separations. A high concentration sample, 1.5 mmol/L NaCl, was used to make the identification of a conductivity step easier. Figure 5.7A shows the raw data, and Figure 5.7B shows the 51-point Savitzky-Golay derivative.<sup>58</sup> Although resolution cannot be determined from this separation (because only one analyte was separated), the step width can be determined and compared to the step width of samples analyzed in longer GEMBE channels. The baseline step width of the peak in Figure 5.7B is approximately 3 s. In comparison to the step width of the data included in Chapters 2 and 3 (separated with a 2 to 3 mm long channel), the PDMS GEMBE device (200 to 300  $\mu\text{m}$  long channel) has a step width an order of magnitude smaller.

In Chapter 1, the step width of GEMBE with channel current detection was related to the channel length. The data in Figure 5.7 shows a reduced step width with a reduced channel length, as expected. Also, as expected, the counter-flow acceleration for shorter channel lengths is smaller (Figure 5.6) than the acceleration for longer channel lengths. To gain an understanding of the PDMS device behavior, an optical microscope was used to image the device while filling and during a typical GEMBE separation. Visualization of the device was the next step due to the variability in device performance during data collection and to the relatively short time that each device was able to operate under the pressures required for GEMBE.



Pressure gradient acceleration:  $-5\text{Pa}/2\text{s}$

Elution time: 1338 s

Elution Pressure: 36,655 Pa

**Figure 5.7:** GEMBE separation of a sample containing 1 mmol/L NaCl in a PDMS device with a channel length of 200-to-300  $\mu\text{m}$ . The run buffer was 100 mM Bis-tris, and 100 mM HEPES. The step width in B is an order of magnitude smaller than that of the separations in 2- to 3-mm channels in Chapters 2 and 3.

To determine if delamination was the cause of device failure, the PDMS GEMBE device was mounted on an optical microscope to allow visualization of the reservoir channel and of the separation channel. Figure 5.8 shows a series of images of a PDMS GEMBE device taken through the glass coverslip. The images show the device as it was being filled at pressures from 1,000 Pa to 5,000 Pa. Initially, in Figure 5.8 A, one side of the buffer reservoir channel was connected to PEEK tubing, as mentioned above. The channels were allowed to fill with run buffer at 2,000 Pa until a bead of buffer was visible in the sample reservoir (Figure 5.8C, approximately 20 minutes). The PDMS began to separate from the glass coverslip (Figure 5.8B) approximately 6 hours after the channels were filled with run buffer, after pressures between 30,000 Pa and 40,000 Pa were applied.

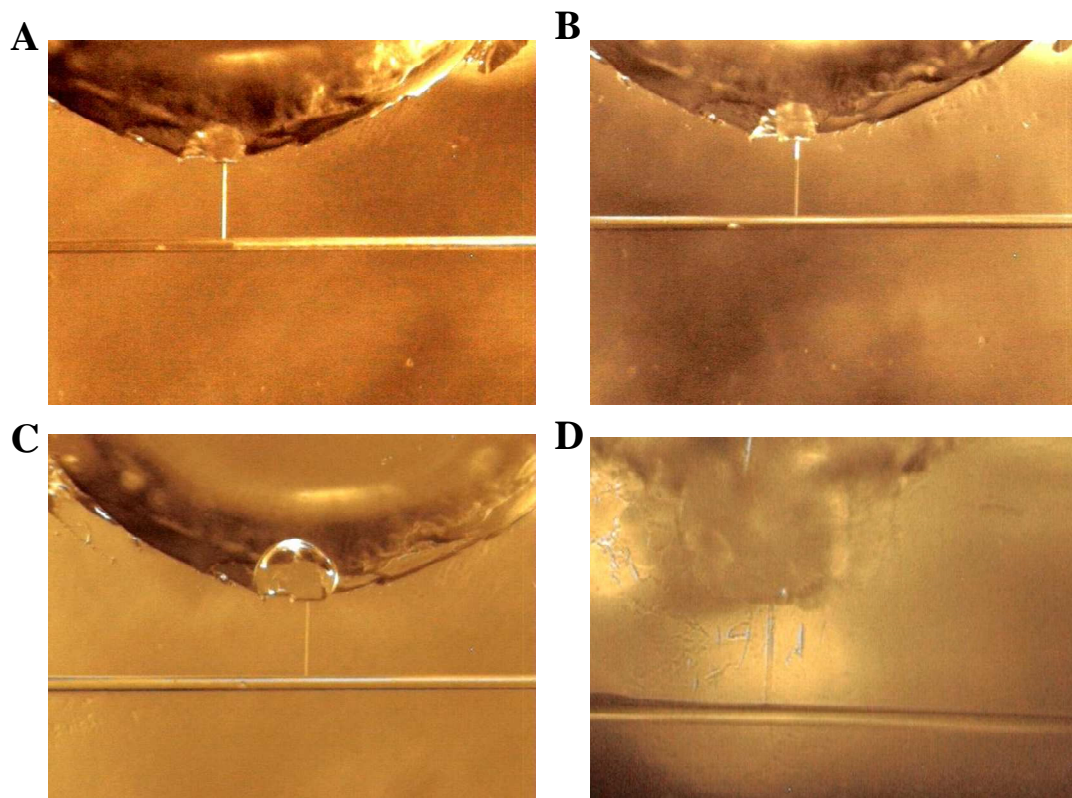


**Figure 5.8:** Images taken through the glass coverslip of a PDMS GEMBE device as it is filled with run buffer for the first time. In (A) half of the reservoir channel is filled, and (B) the entire reservoir channel and half of the separation channel are filled, and (C) both channels are filled, and a bead of run buffer is visible in the sample reservoir, and finally (D) the run buffer has begun to leak between the PDMS and the glass coverslip. Leakage is also indicated by an increase in the current that is measured.

To visualize a separation, a 6-carboxy-fluorescein solution was prepared. A new device was filled in the same manner as shown in Figure 5.8, and a sample containing 6-carboxy-fluorescein was pipetted into the sample reservoir. Figure 5.9 shows a series of images collected during a separation. In Figures 5.9A, B, and C, the counter-flow was too great to allow the fluorescent analyte to enter the separation channel, and a dark region in the sample reservoir was present. As the pressure was decreased, the dark area decreased as the fluorescent analyte moved closer to the entrance of the separation channel. When the counter-flow pressure was less than the electrophoretic velocity of 6-carboxy-fluorescein (Figure 5.9D), the fluorescent analyte entered the separation channel. For the

separations in Figures 5.8 and 5.9 the voltage applied to the device was 100 V. The application of higher voltages (300 to 500V) caused the rapid production of bubbles at the entrance of the separation capillary. Air bubbles were also observed in the separation reservoir if incomplete removal of the previous sample occurred. In these cases, the current measured across the channel decreased partially, or completely to zero. This decrease in current was dependent on the location and size of the air bubble. The device used to collect the images in Figure 5.9 was able to maintain a pressure of 1,000 Pa for two days before the PDMS mold separated from the glass coverslip.

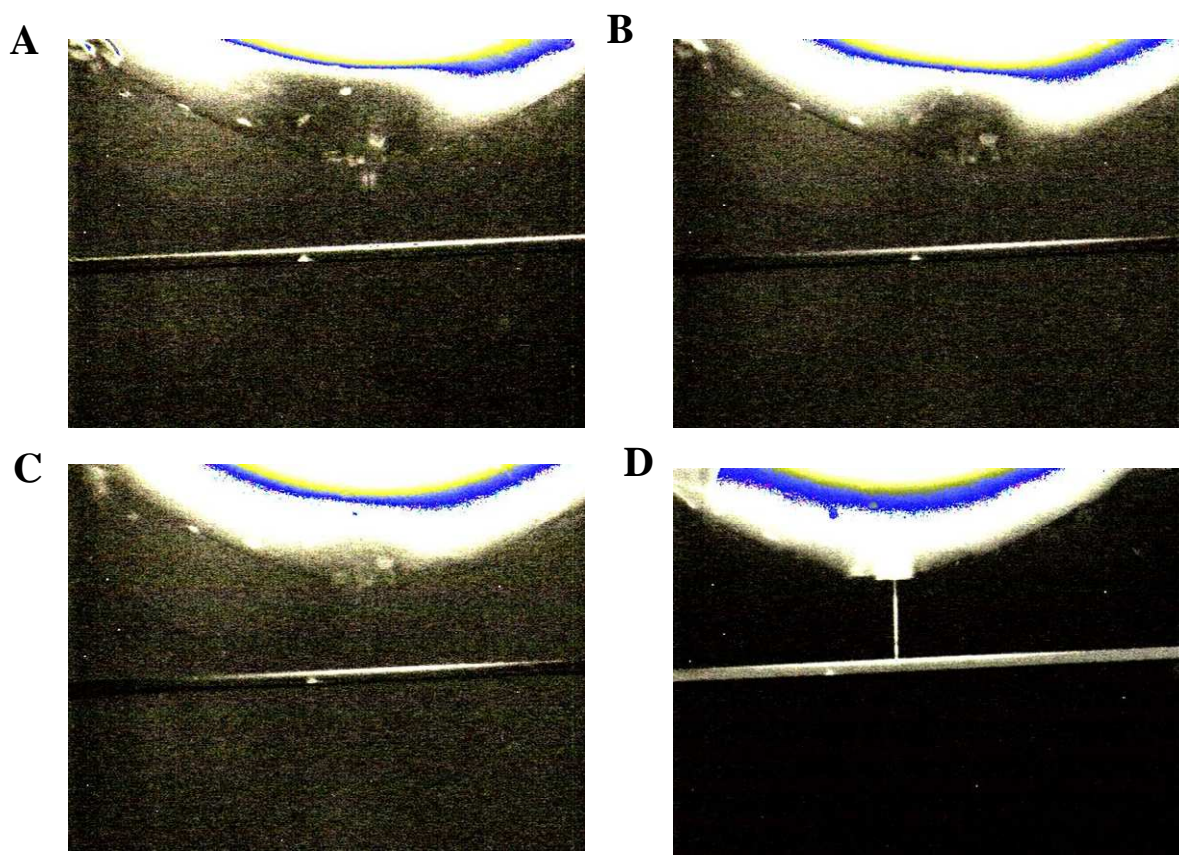


**Figure 5.9:** A series of images of the GEMBE separation of a sample containing 6-carboxy-fluorescein. In (A), (B), and (C), the pressure applied to the run buffer reservoir excluded the fluorescent analyte from the separation channel and in (D) the separation channel was filled with fluorescent analyte.

## 5.4 Conclusion

The use of an optical microscope and of a fluorescent analyte to visualize GEMBE separations in the PDMS device revealed that delamination occurred within 1 to 2 days (maximum) of the device being connected to the pressure supply. Indications of delamination included an increase in the measured current, visible fluid streams outside of the separation channel, and filling of the reservoir channel with fluorescent analyte without observing fluorescence in the separation channel. Future work to improve the device performance will be discussed in Chapter 6.

## Chapter 6: Conclusions and future work

### 6.1 Conclusions

Advances in the field of microfluidics have resulted in devices and methods of analysis that are able to perform a wide variety of functions, such as chemical analysis, chemical synthesis, and biological assays. Many of these functions take advantage of the absence of mixing due to the laminar flow of fluids when they are confined to microfluidic devices. In Chapter 1, pressure-driven flow in microfluidic devices was discussed, and the specific case of GEMBE was introduced. GEMBE is an electrophoretic method that was developed with the goal of simplifying the detection of ions in complex solutions by excluding large contaminants from the separation channel with a pressure driven counter-flow.

Further improvements to the GEMBE method were introduced in Chapters 2 and 3, where the implementation of concentration enhancement by sample dilution was discussed. The use of channel current detection and concentration enhancement provides a method of improving the LOD of GEMBE while maintaining a simple sample preparation method and detection method. With the concentration method discussed in Chapter 3 a LOD improvement of 60× was achieved for the detection of ions in drinking water.

In Chapters 4 and 5, the fabrication of microfluidic devices with circular cross sections, and their inclusion into microfluidic devices was introduced. The use of MAP fabrication provides the ability to control structural dimensions in all three Cartesian directions, so that microfluidic devices can be created with circular channels that closely resemble the dimensions of the fused silica

capillaries used in the original demonstrations of GEMBE. In Chapter 5, the fabrication and assembly of PDMS microfluidic devices, as well as their use for GEMBE separations, were investigated. Due to the high pressures required to perform GEMBE separations, the devices were unable to be used for more than 1 or 2 days. Although the separations performed with different devices using the same sample analytes were not always consistent, data suggesting a smaller step width were obtained. Additionally, optical and fluorescence imaging of the PDMS-GEMBE devices showed that although detection of analyte boundaries is possible, delamination of the PDMS from the glass coverslip occurred after approximately 6 hours of use.

## 6.2 Future work

### 6.2.1 Fluorescence studies

The optical and fluorescence images that were collected during GEMBE separations demonstrated the inability of the PDMS-GEMBE devices to sustain pressures in excess of 10,000 Pa, which is desirable for GEMBE separations. However, the images confirmed the ability of the devices to control entrance of the fluorescent analyte before delamination occurred. Further fluorescence studies should include multiple fluorescent analytes at various concentrations. From these studies, information about the resolution of GEMBE with shorter channels can be obtained. In addition, fluorescence imaging of channels with larger cross sections ( $>10\ \mu\text{m}$ ) should be investigated to determine if a larger channel cross sections will exhibit similar behavior.

### 6.2.2 PDMS composite

Keeping in mind the goal of simplification of the device, of the detection method, and of the sample preparation method, preliminary work to develop a conductive PDMS composite that can be

used as an on-chip electrode was performed. Previous work<sup>79-81</sup> to develop composite materials with PDMS was motivated by the ability to create a PDMS-PDMS interface between composite and microfluidic devices made of PDMS by plasma cleaning both pieces. A common issue when PDMS composites are created is the difficulty found in mixing a powder (carbon black, silver, etc.) in a quantity large enough to create a functional (conductive, magnetic, etc.) PDMS composite material. Typically the weight percent is limited to about 25% when carbon black is mixed with PDMS. Beyond 25%, mixing becomes difficult, and the resulting composite material is often non-uniform and brittle. By adding a variety of volatile solvents (ethanol and hexane) to the PDMS or to the carbon black, weight percentages exceeding 30% carbon black have been achieved. Future work to create electrodes from the PDMS composite materials should include improvement of the interface between the PDMS composite and conductive material, as well as the investigation of a larger variety of solvents.

### 6.2.3 Molding material

One primary problem with the PDMS-GEMBE devices discussed in Chapter 5 could be the PDMS material. To determine if a different material would allow the application of higher pressures for longer amounts of time, a variety of thermoplastics should be investigated. As a starting point, thermoplastic materials that are flexible enough to peel off of a master structure and that are optically transparent (for optical and fluorescent imaging) should be used. The primary goal of using a different molding material would be to achieve an improved seal with the glass coverslip.

# Appendices

## A.1 LabView program for GEMBE separations

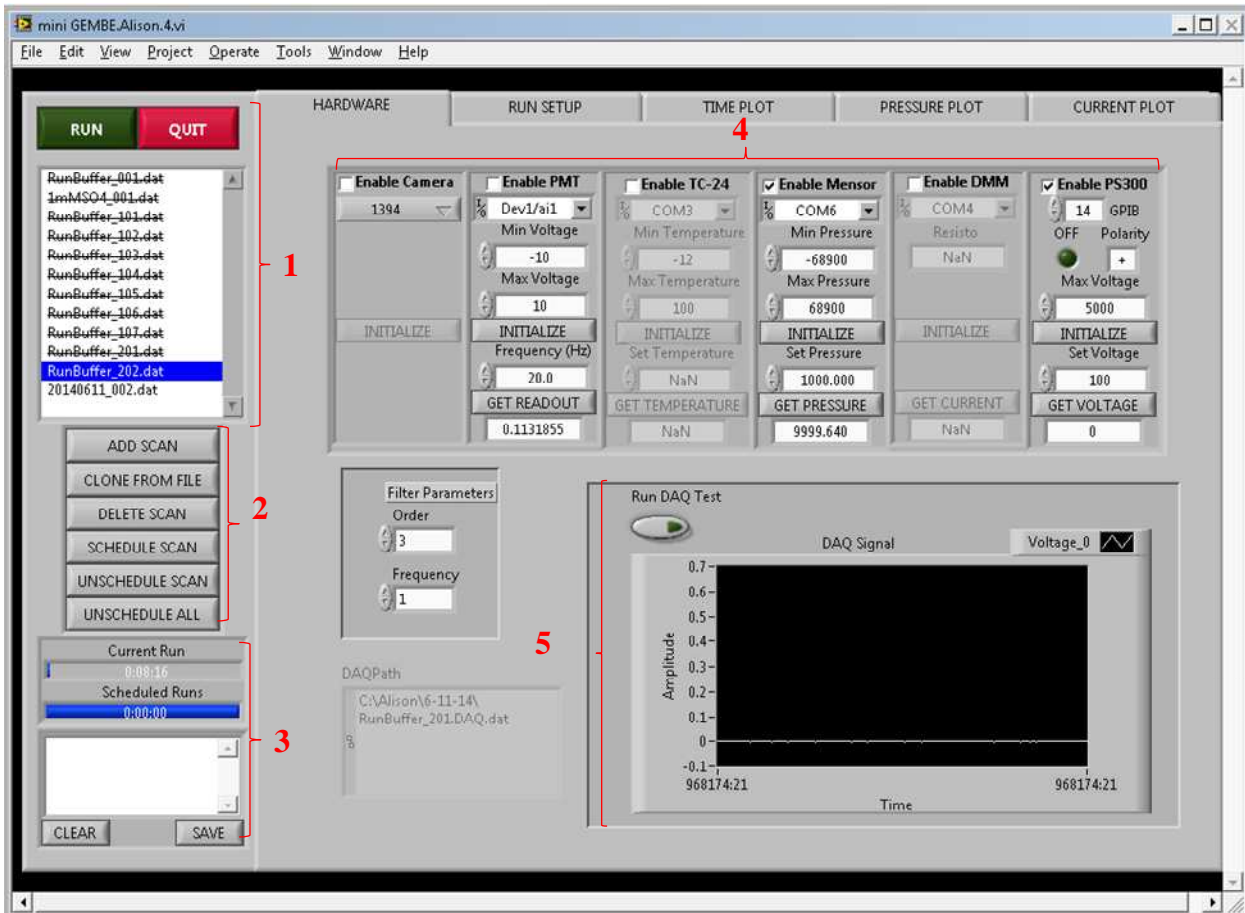


**Figure A.1.1:** The instrument interface panel of the LabView program used to control GEMBE separations. 1: The green Run button starts a scheduled separation, and the red Quit button stops a running separation and the program. The white panel displays past, current, and future separations with file names that can be user-defined. 2: Command buttons. All commands are executed on the filename that is highlighted in blue when the button is clicked. 3: Time remaining is displayed in blue bars with white lettering. Below, the white box displays errors or messages as they occur during a scan. 4: Each panel allows communication with various instrumentation. For the GEMBE applications discussed in this document, the “Mensor” and “PS3000” options were used (the pressure controller and high voltage supply, respectively). 5: Data acquisition plot. A real-time display of data acquisition that is commonly used to monitor changes in signal amplitude when the applied pressure or voltage is changed.

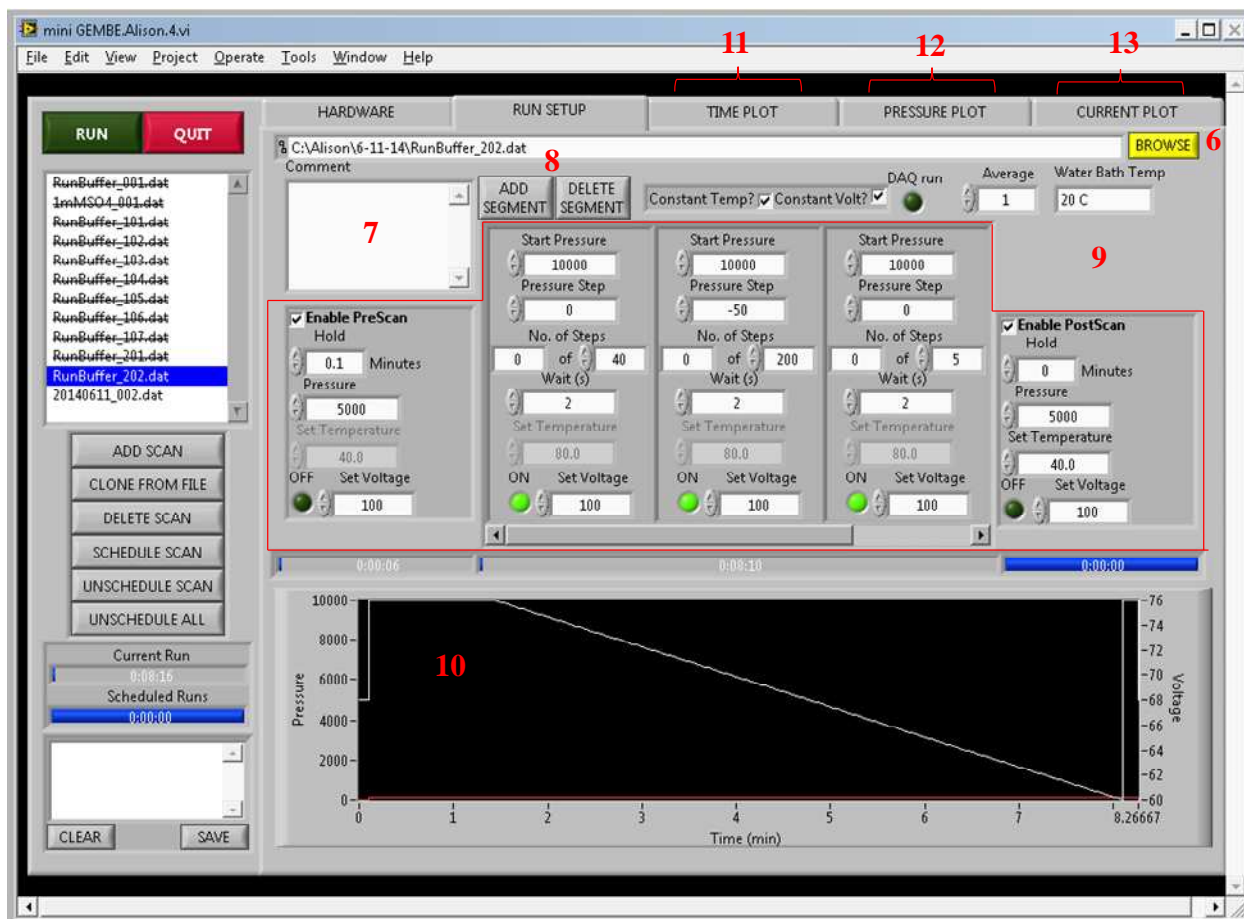


**Figure A.1.2:** The separation parameter control panel of the LabView program used to control GEMBE separations. 6: “Browse” opens the dialogue box to name a file and designate where the file is to be saved. 7: Information written in the “Comment” box is saved with the separation. 8: Buttons to add or remove panels in “9”. 9: Segments of a separation. Separation parameters are adjusted here for each separation. 10: Time vs Pressure and Voltage for the segments in “9”. 11, 12, 13: Various real-time displays of separation data.

## A.2 Representative Mathematica worksheet

### Setup and Load Data

<<NonlinearRegression`

General::obspkg :

NonlinearRegression` is now obsolete. The legacy version being loaded may conflict with current Mathematica functionality.

See the Compatibility Guide for updating information. >>

```
SetDirectory["C:\Users\Ali\Desktop\GEMBE As Paper\GEMBE  
Raw Data\GEMBE Raw Data for As Paper\9-20-11 2x Buffer dilutions"]
```

```
C:\Users\Ali\Desktop\GEMBE As Paper\GEMBE Raw  
Data\GEMBE Raw Data for As Paper\9-20-11 2x Buffer dilutions
```

```
DAQFiles = FileNames["*DAQ*"]
```

```
{1_100uMP_50uMAs_002.DAQ.dat, 1_100uMP_50uMAs_003.DAQ.dat, 1_100uMP_50uMAs_004.DAQ.dat,  
2_50uMP_25uMAs_001.DAQ.dat, 2_50uMP_25uMAs_002.DAQ.dat,  
2_50uMP_25uMAs_003.DAQ.dat, 3_25uMP_12.5uMAs_001.DAQ.dat, 3_25uMP_12.5uMAs_002.DAQ.dat,  
3_25uMP_12.5uMAs_003.DAQ.dat, 4_12.5uMP_6.25uMAs_001.DAQ.dat,  
4_12.5uMP_6.25uMAs_002.DAQ.dat, 4_12.5uMP_6.25uMAs_003.DAQ.dat,  
5_6.25uMP_3.125uMAs_001.DAQ.dat, 5_6.25uMP_3.125uMAs_002.DAQ.dat,  
5_6.25uMP_3.125uMAs_003.DAQ.dat, 6_3.125uMP_1.5625uMAs_002.DAQ.dat,  
6_3.125uMP_1.5625uMAs_003.DAQ.dat, 6_3.125uMP_1.5625uMAs_004.DAQ.dat}
```

```
DAQFiles
```

```
{1_100uMP_50uMAs_002.DAQ.dat, 1_100uMP_50uMAs_003.DAQ.dat, 1_100uMP_50uMAs_004.DAQ.dat,  
2_50uMP_25uMAs_001.DAQ.dat, 2_50uMP_25uMAs_002.DAQ.dat,  
2_50uMP_25uMAs_003.DAQ.dat, 3_25uMP_12.5uMAs_001.DAQ.dat, 3_25uMP_12.5uMAs_002.DAQ.dat,  
3_25uMP_12.5uMAs_003.DAQ.dat, 4_12.5uMP_6.25uMAs_001.DAQ.dat,  
4_12.5uMP_6.25uMAs_002.DAQ.dat, 4_12.5uMP_6.25uMAs_003.DAQ.dat,  
5_6.25uMP_3.125uMAs_001.DAQ.dat, 5_6.25uMP_3.125uMAs_002.DAQ.dat,  
5_6.25uMP_3.125uMAs_003.DAQ.dat, 6_3.125uMP_1.5625uMAs_002.DAQ.dat,  
6_3.125uMP_1.5625uMAs_003.DAQ.dat, 6_3.125uMP_1.5625uMAs_004.DAQ.dat}
```

```
inputData0 = Table[Transpose[Drop[Import[DAQFiles[[j]], "TSV"], 1]], {j, Length[DAQFiles]}];
```

- No binning

```
timeDataBig = Table[Table[inputData0[[j]][[1]][[i]] - inputData0[[j]][[1]][[1]],  
{i, Length[inputData0[[j]][[1]]}], {j, Length[DAQFiles]}];
```

```
inputDataBig = Table[Table[inputData0[[j]][[2]][[i]],  
{i, Length[inputData0[[j]][[1]]}], {j, Length[DAQFiles]}];
```

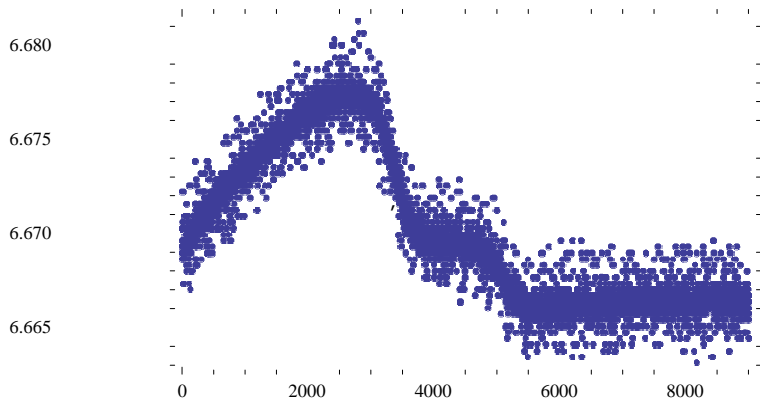
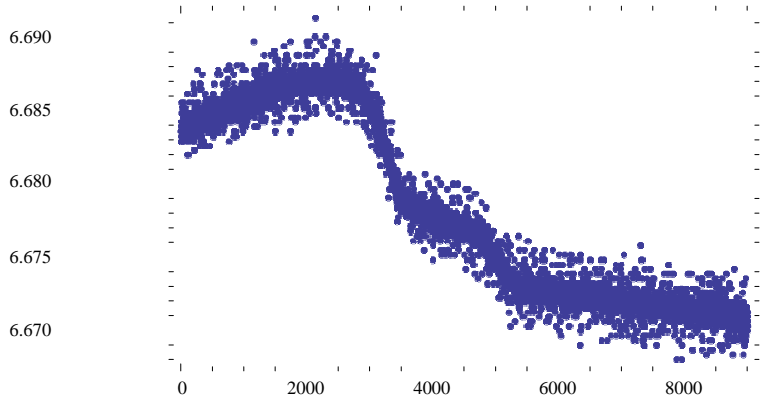
```
inputData = Table[Transpose[{timeDataBig[[j]], inputDataBig[[j]]}], {j, Length[DAQFiles]}];
```

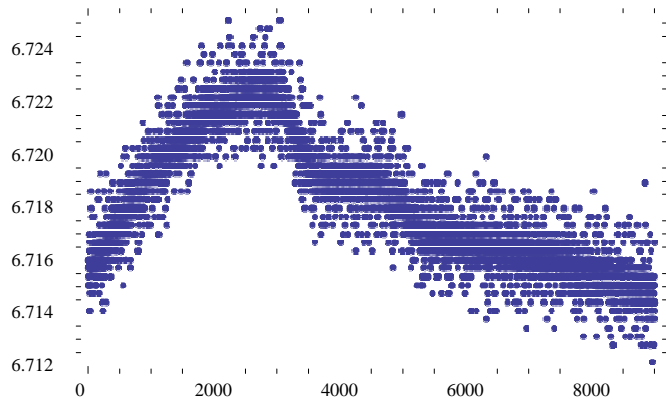
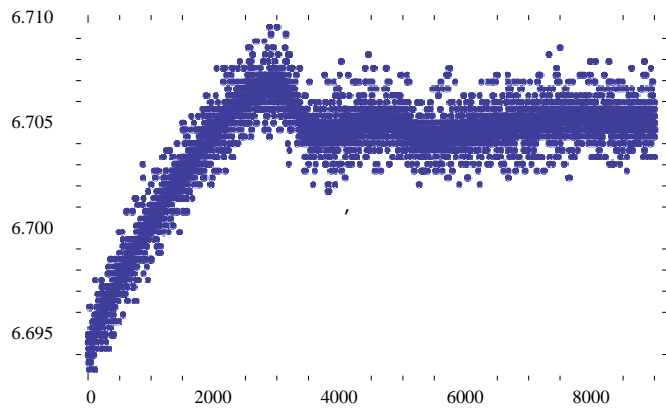
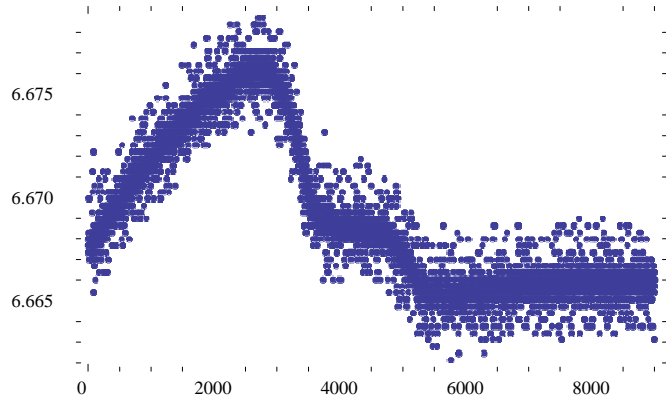
- Trim Data Front and Back

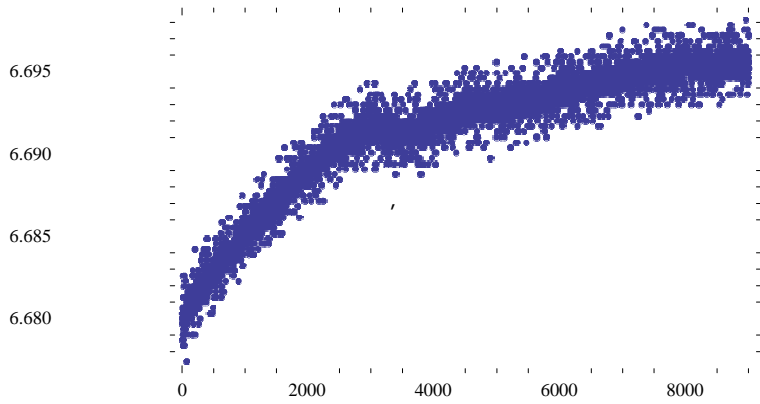
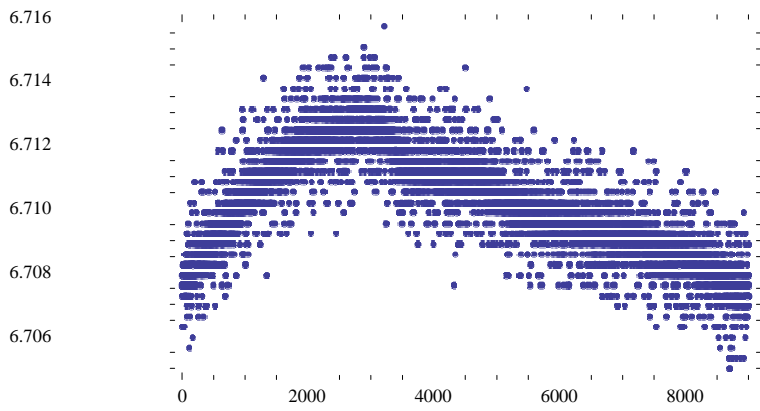
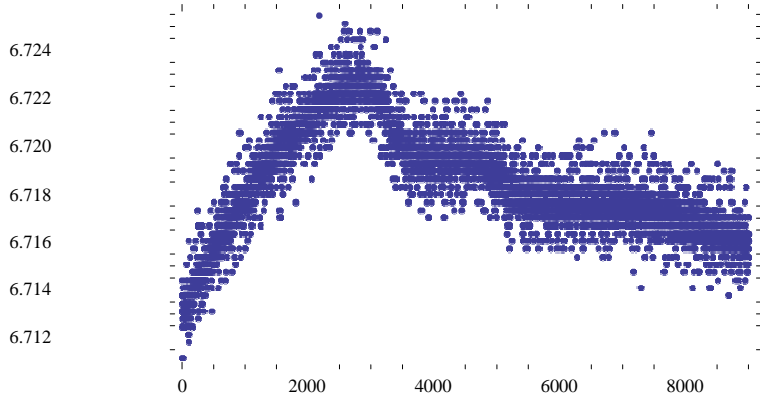
```
trimFront = 3000;
```

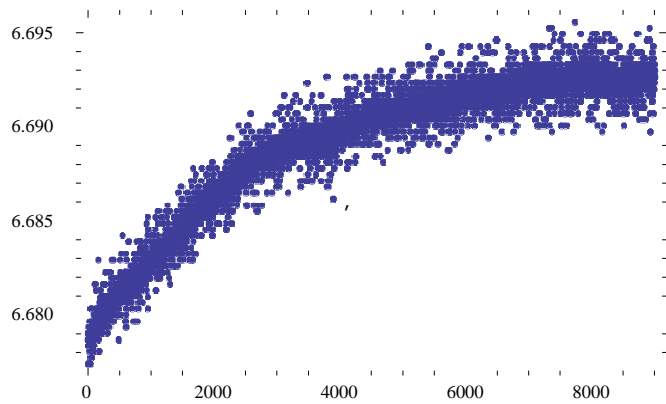
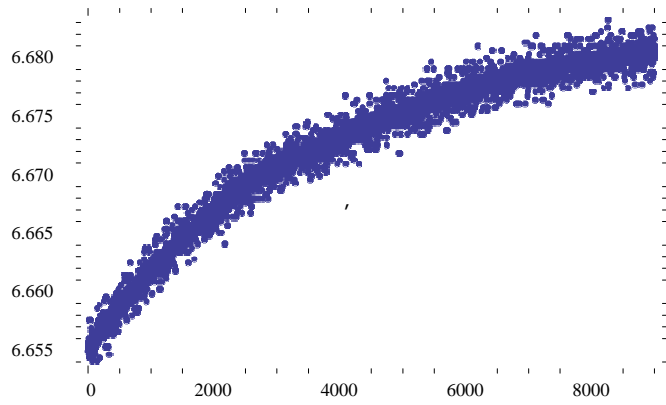
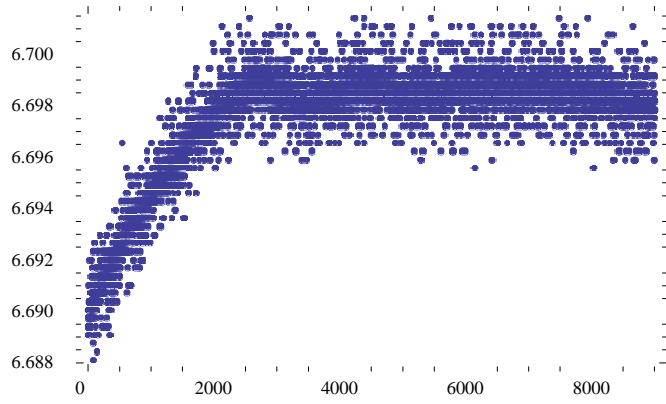
```
trimLength = 9000;
```

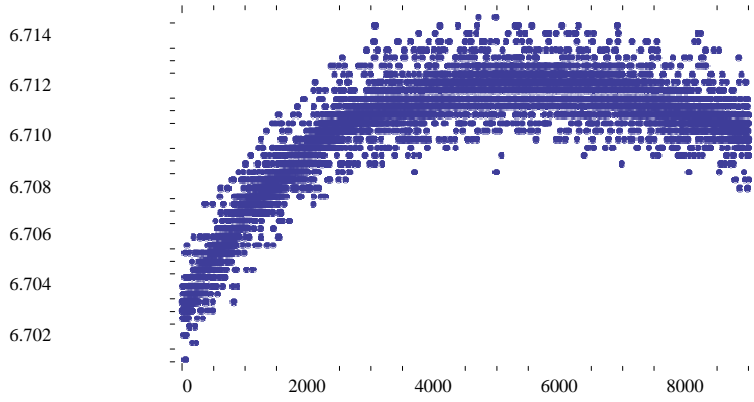
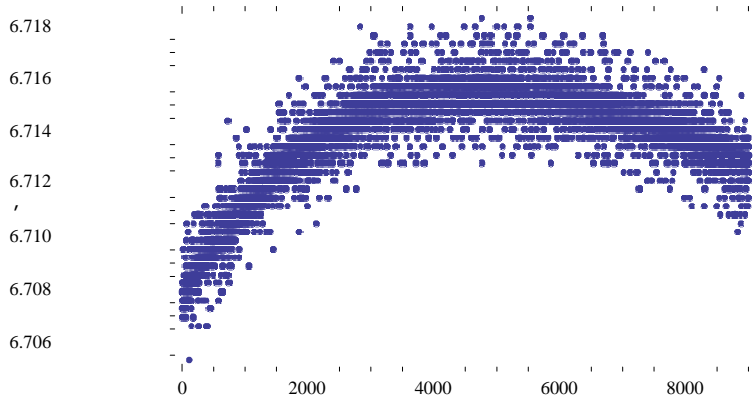
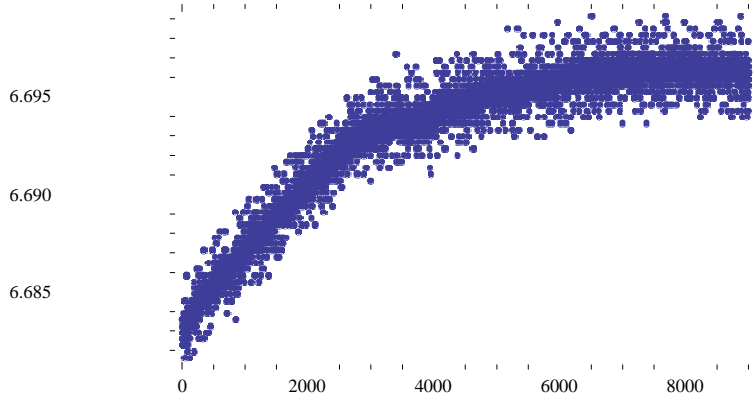
```
Table[ListPlot[Take[inputDataBig[[j]], {trimFront, trimFront + trimLength}], PlotRange -+ All, GridLines -+ Automatic, Frame -+ True], {j, 1, Length[DAQFiles]}]
```

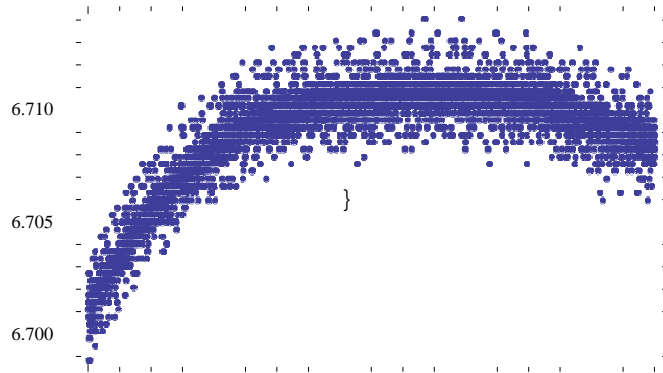
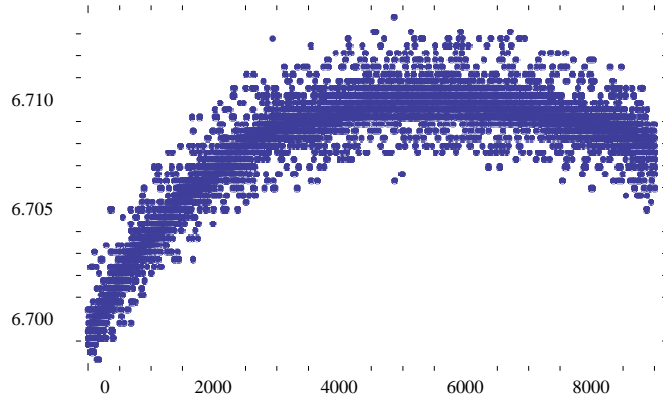
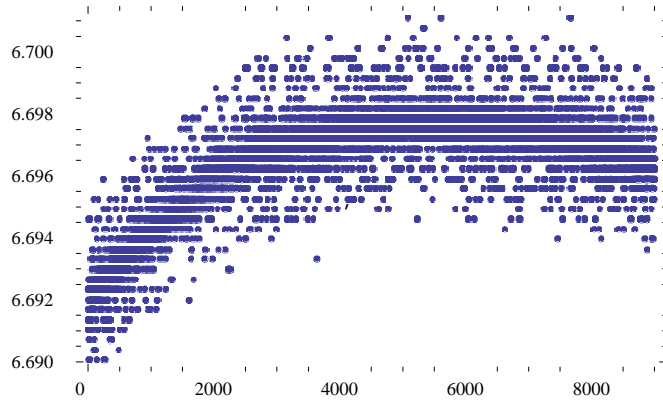
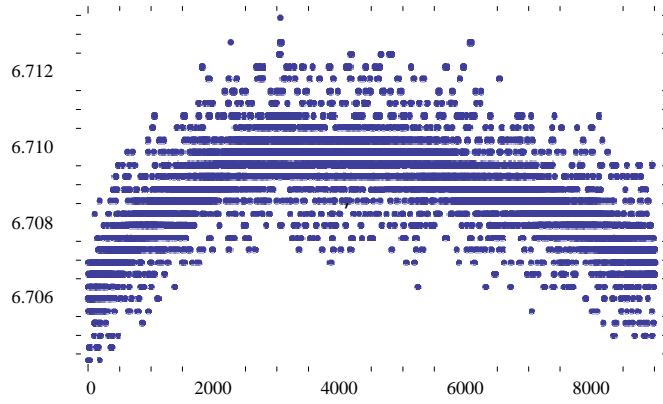




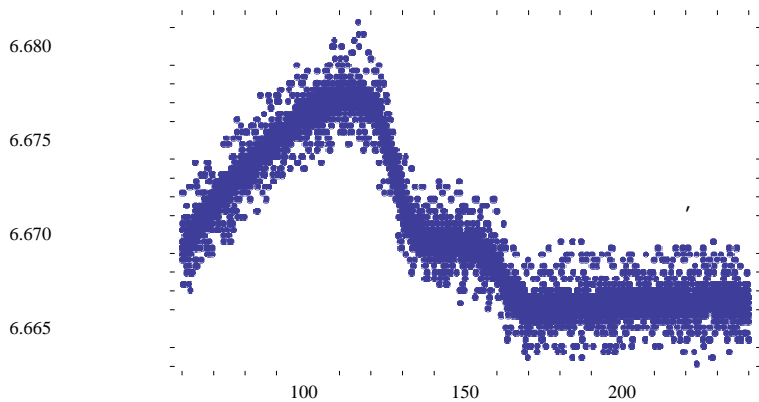
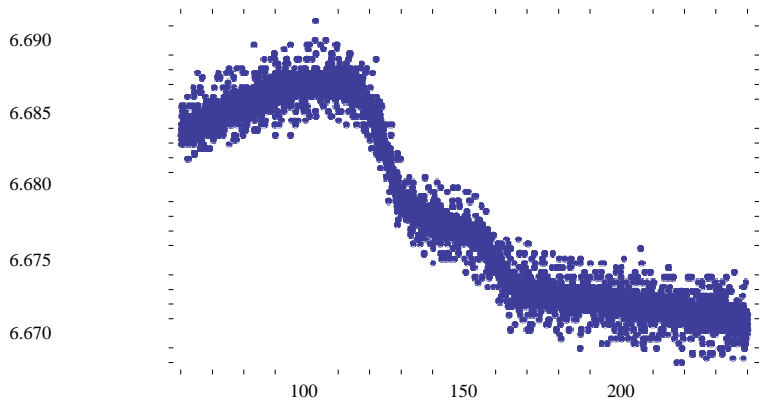


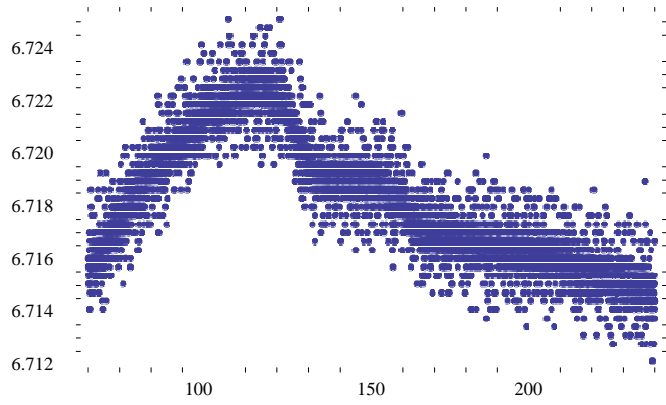
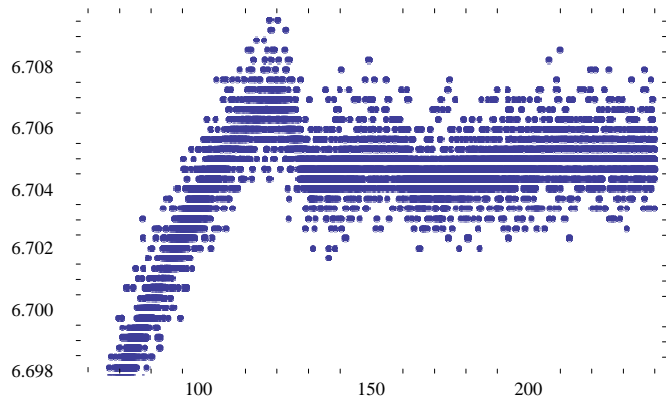
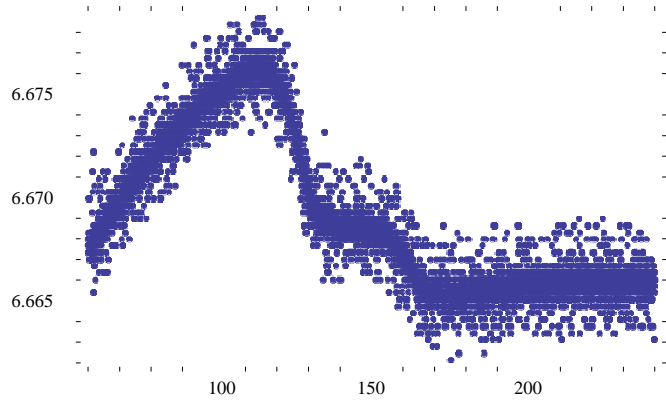


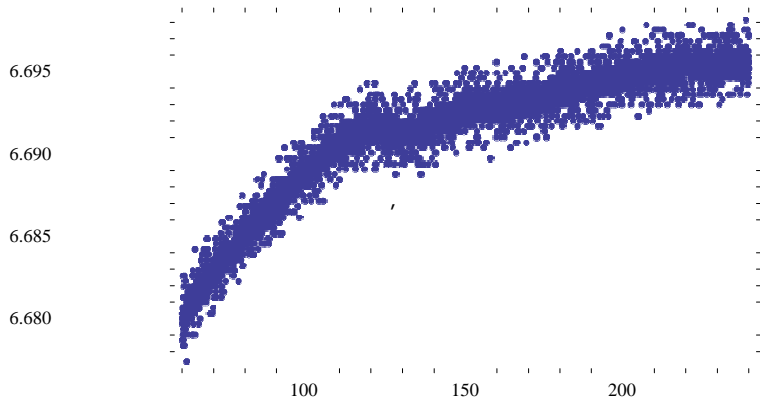
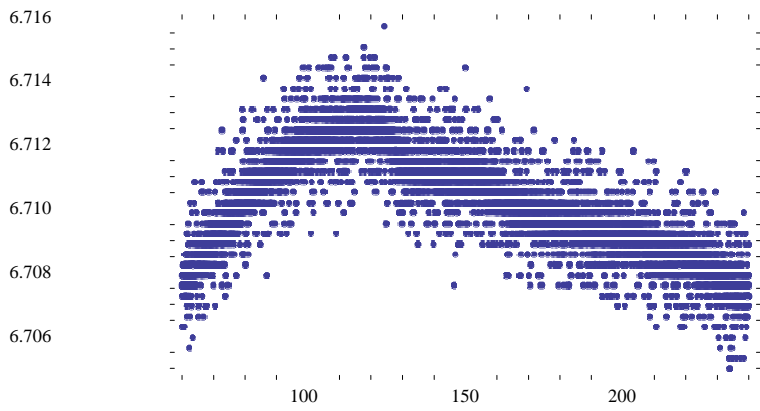
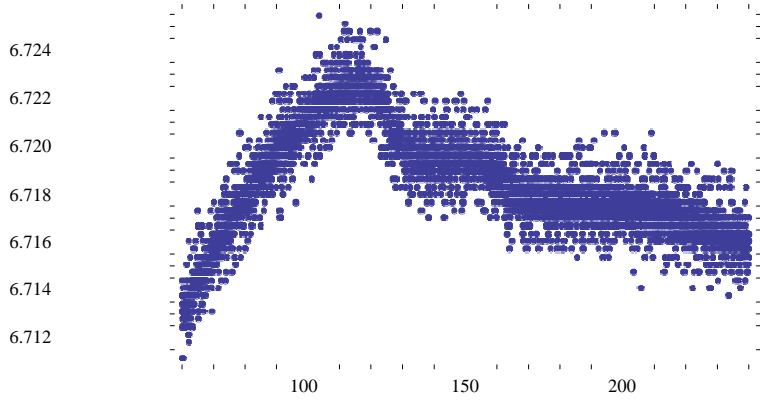


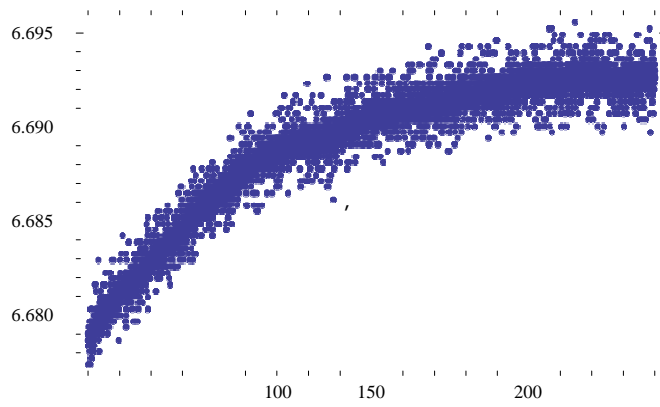
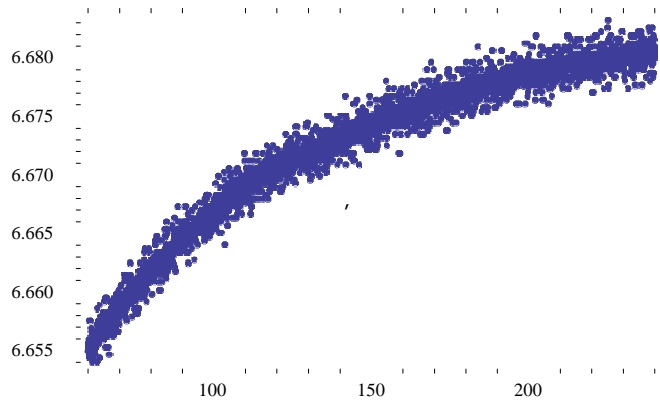
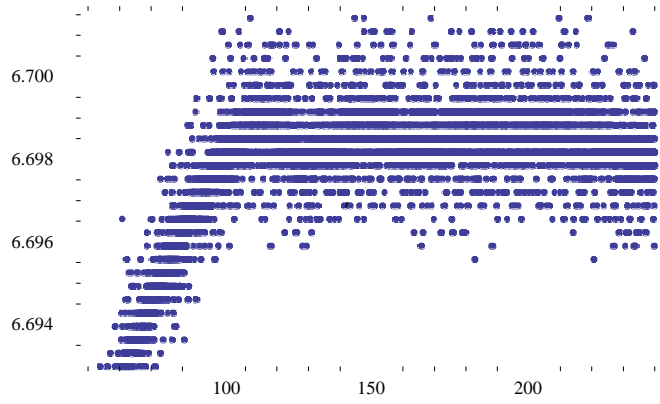


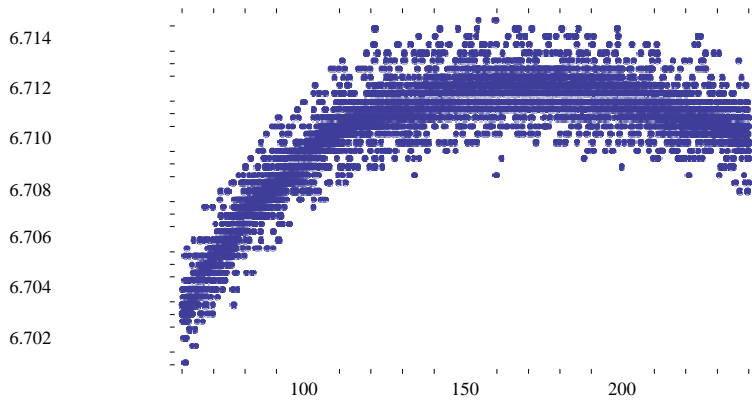
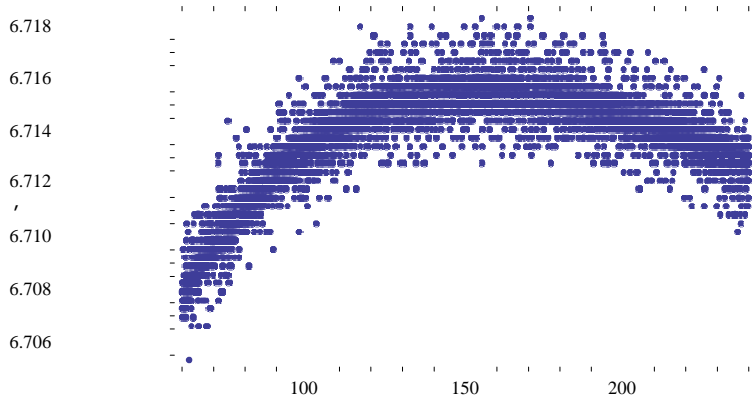
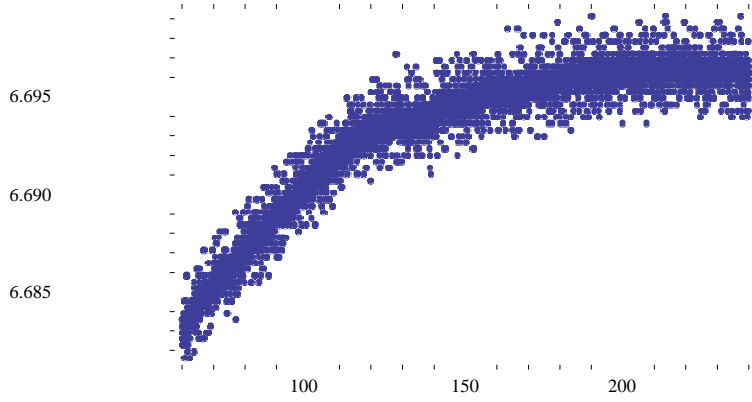
```
inputSteps1 =  
Table[Take[inputDataBig[[j]], {trimFront, trimFront+trimLength}], {j, Length[DAQFiles]};  
  
inputTime1 =  
Table[Take[timeDataBig[[j]], {trimFront, trimFront+trimLength}], {j, Length[DAQFiles]};  
  
inputData1 =  
Table[Take[inputData[[j]], {trimFront, trimFront+trimLength}], {j, Length[DAQFiles]};  
  
p3 = Table[ListPlot[inputData1[[j]], GridLines -> Automatic, Frame -> True], {j, Length[DAQFiles]}
```

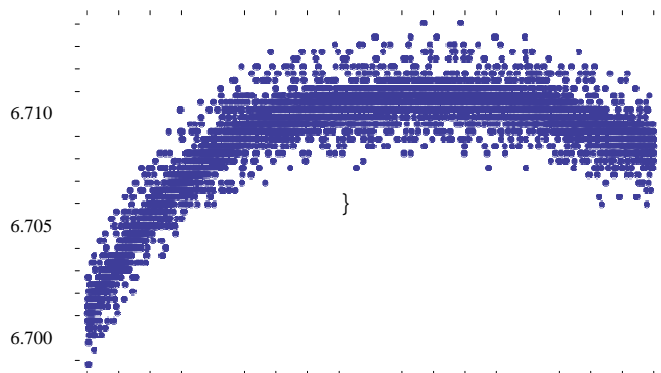
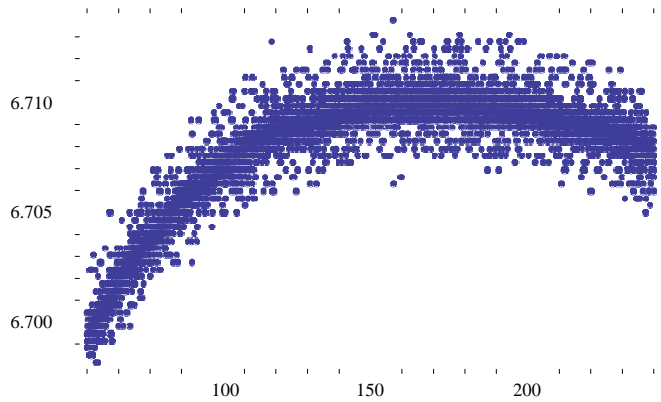
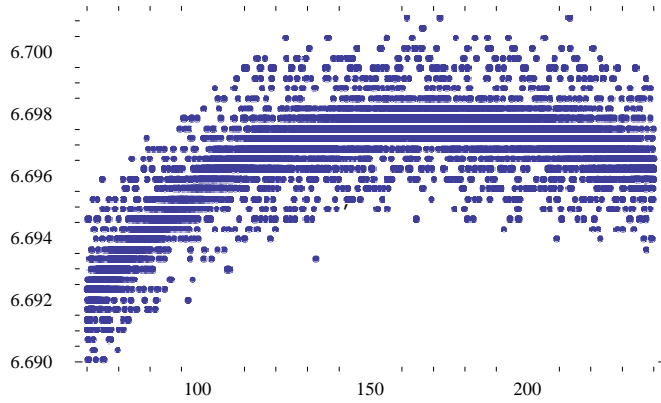
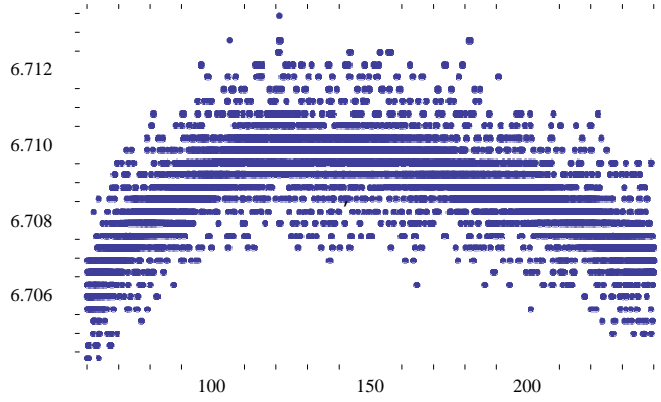










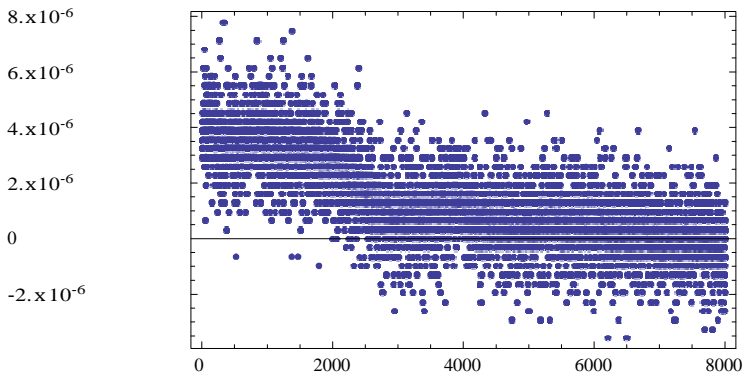


## Take Derivative and Smooth - then find peak maxima

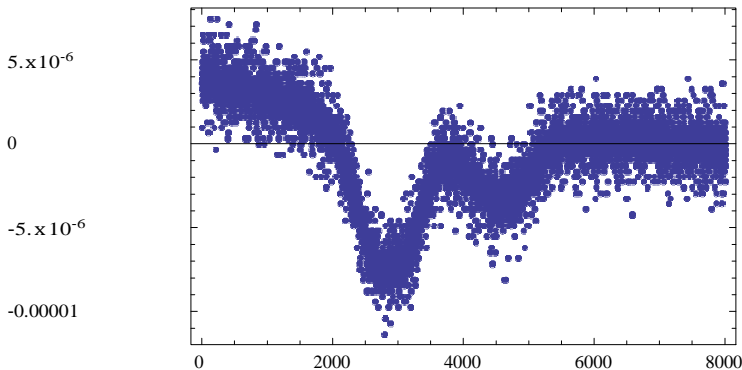
- Derivative and smoothing

```
smoothLength = 1000
1000
quickDerivTab = Table[ListCorrelate[{-1, 1}, inputSteps1[[j]], {j, Length[DAQFiles]}]; smDerivTab =
Table[MovingAverage[quickDerivTab[[j]], smoothLength], {j, Length[DAQFiles]}]; quickTimeTab =
Table[ListCorrelate[{0.5, 0.5}, inputTime1[[j]], {j, Length[DAQFiles]}]; smTimeTab =
Table[MovingAverage[quickTimeTab[[j]], smoothLength], {j, Length[DAQFiles]}];
peakPositions =
{{2750, 4450}, {2900, 4600}, {2850, 4550}, {2800, 4600}, {2850, 4550}, {2850, 4650},
{2900, 4700}, {2750, 4600}, {2650, 4400}, {3300, 4700}, {2900, 4450}, {2600, 4400},
{2900, 4100}, {2550, 4100}, {3100, 4500}, {3900, 6000}, {2900, 4550}, {2600, 4350}}
{{2750, 4450}, {2900, 4600}, {2850, 4550}, {2800, 4600}, {2850, 4550}, {2850, 4650},
{2900, 4700}, {2750, 4600}, {2650, 4400}, {3300, 4700}, {2900, 4450}, {2600, 4400},
{2900, 4100}, {2550, 4100}, {3100, 4500}, {3900, 6000}, {2900, 4550}, {2600, 4350}}
```

```
jj = 12;
ListPlot[smDerivTab[[jj], GridLines -> {peakPositions[[jj], None}, PlotRange -> All, Frame -> True]
```



```
jj = 2;
ListPlot[smDerivTab[[jj], GridLines -> {peakPositions[[jj], None}, PlotRange -> All, Frame -> True]
```



```

Table[ListPlot[smDerivTab[[j]], GridLines -> {peakPositions[[j]], None}, PlotRange ->
All, Frame -> True], {j, Length[DAQFiles]};

stepTimes1 = Table[Table[smTimeTab[[j]][[peakPositions[[j]][[i]]]], {i, 2}], {j, 1, 6}]
{{124.96, 158.96}, {127.96, 161.96}, {126.96, 160.96},
{125.96, 161.96}, {126.96, 160.96}, {126.96, 162.96}}

stepTimes2 = Table[Table[smTimeTab[[j]][[peakPositions[[j]][[i]]]], {i, 2}], {j, 7, 18}]
{{127.96, 163.96}, {124.96, 161.96}, {122.96, 157.96}, {135.96, 163.96},
{127.96, 158.96}, {121.96, 157.96}, {127.96, 151.96}, {120.96, 151.96},
{131.96, 159.96}, {147.96, 189.96}, {127.96, 160.96}, {121.96, 156.96}}

```

## Fit with Erf[x] all the same width (x1 and x2 for 1-6....different spacing)

fitFunct[x\_] =

$$A + B * (x - x2) + B2 * (x - x2)^2 + C1 / 2 * \text{Erf}[(x - x1) / \sqrt{2} / \Sigma] + C2 / 2 * \text{Erf}[(x - x2) / \sqrt{2} / \Sigma]$$

$$\frac{1}{2} A + B(x - x2) + B2(x - x2)^2 + \frac{C1}{2} \frac{x - x1}{\sqrt{2} \Sigma} + \frac{C2}{2} \frac{x - x2}{\sqrt{2} \Sigma}$$

fitFunct[x]

$$\frac{1}{2} A + B(x - x2) + B2(x - x2)^2 + \frac{C1}{2} \frac{x - x1}{\sqrt{2} \Sigma} + \frac{C2}{2} \frac{x - x2}{\sqrt{2} \Sigma}$$

AGuess = Table[(inputData1[[i]][[1]][[2]] + inputData1[[i]][[-1]][[2]]) / 2., {i, 1, 6}]

{6.67741, 6.66832, 6.66669, 6.69932, 6.7162, 6.71539}

BGuess = Table[.000001, {i, 1, 6}]

B2Guess = Table[-.0000001, {i, 1, 6}]

{1. x 10<sup>-6</sup>, 1. x 10<sup>-6</sup>}

{-1. x 10<sup>-7</sup>, -1. x 10<sup>-7</sup>}

CGuess = 0.70 \* Table[(inputData1[[i]][[-1]][[2]] - inputData1[[i]][[1]][[2]]), {i, 1, 6}]

{-0.0086351, -0.00545375, -0.00136344, 0.00749891, 0.000681719, 0.00136344}

stepTimes1

{{124.96, 158.96}, {127.96, 161.96}, {126.96, 160.96},  
{125.96, 161.96}, {126.96, 160.96}, {126.96, 162.96}}

x1Guess = Transpose[stepTimes1][[1]]

{124.96, 127.96, 126.96, 125.96, 126.96, 126.96}

x2Guess = Transpose[stepTimes1][[2]]

{158.96, 161.96, 160.96, 161.96, 160.96, 162.96}

ΣGuess = Table[trimLength / 2000., {i, 1, 6}]

{4.5, 4.5, 4.5, 4.5, 4.5, 4.5}

```

jj = 2; test[x_] =
fitFunct[x] /. {A -> AGuess[[jj]], B -> BGuess[[jj]], B2 -> B2Guess[[jj]], C1 -> CGuess[[jj]],
C2 -> CGuess[[jj]], x1 -> x1Guess[[jj]], x2 -> x2Guess[[jj]], Σ -> ΣGuess[[jj]]}

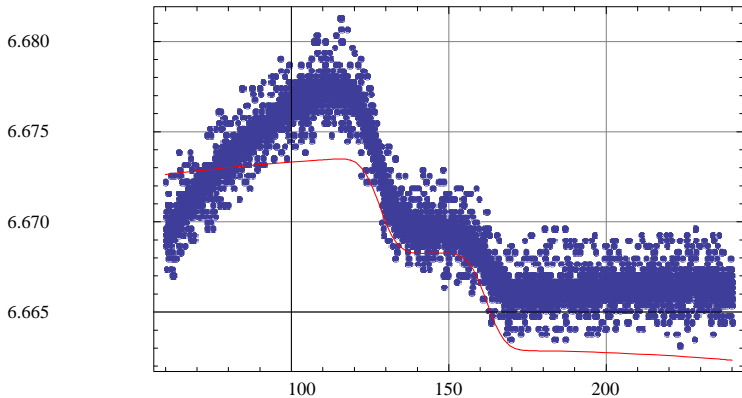
```

$$6.66832 + 1. \times 10^{-6} (-161.96 + x) - 1. \times 10^{-7} (-161.96 + x)^2 - 0.00272687 \operatorname{Erf}[0.157135 (-161.96 + x)] - 0.00272687 \operatorname{Erf}[0.157135 (-127.96 + x)]$$

```

p4 = Plot[test[x], {x, inputData1[[jj]][1][1], inputData1[[jj]][-1][1]}, PlotStyle -> Hue[0]]; Show[p3[[jj]], p4]

```



```

Fits0 = Table[NonlinearModelFit[inputData1[[j]], fitFunct[x], {{A, AGuess[[j]]}, {B, BGuess[[j]]}, {B2, B2Guess[[j]]}, {C1, CGuess[[j]]}, {C2, CGuess[[j]]}, {x1, x1Guess[[j]]}, {x2, x2Guess[[j]]}, {Σ, ΣGuess[[j]]}}, {x}], {j, 10, Length[DAQFiles]}]

```

**TableForm[DAQFiles]**

- 1\_100uMP\_50uMAs\_002.DAQ.dat
- 1\_100uMP\_50uMAs\_003.DAQ.dat
- 1\_100uMP\_50uMAs\_004.DAQ.dat
- 2\_50uMP\_25uMAs\_001.DAQ.dat
- 2\_50uMP\_25uMAs\_002.DAQ.dat
- 2\_50uMP\_25uMAs\_003.DAQ.dat
- 3\_25uMP\_12.5uMAs\_001.DAQ.dat
- 3\_25uMP\_12.5uMAs\_002.DAQ.dat
- 3\_25uMP\_12.5uMAs\_003.DAQ.dat
- 4\_12.5uMP\_6.25uMAs\_001.DAQ.dat
- 4\_12.5uMP\_6.25uMAs\_002.DAQ.dat
- 4\_12.5uMP\_6.25uMAs\_003.DAQ.dat
- 5\_6.25uMP\_3.125uMAs\_001.DAQ.dat
- 5\_6.25uMP\_3.125uMAs\_002.DAQ.dat
- 5\_6.25uMP\_3.125uMAs\_003.DAQ.dat
- 6\_3.125uMP\_1.5625uMAs\_002.DAQ.dat
- 6\_3.125uMP\_1.5625uMAs\_003.DAQ.dat
- 6\_3.125uMP\_1.5625uMAs\_004.DAQ.dat

```

Fits0 =
Table[NonlinearRegress[inputData1[j], fitFunc[x], {{A, AGuess[[j]]}, {B, BGuess[[j]]},
{B2, B2Guess[[j]]}, {C1, CGuess[[j]]}, {C2, CGuess[[j]]}, {x1, x1Guess[[j]]},
{x2, x2Guess[[j]]}, {Σ, ΣGuess[[j]]}}, {x}, RegressionReport -+
{EstimatedVariance, BestFit, BestFitParameters, ParameterCITable}], {j, 1, 6}];

Fits = Join[Table[, {i, 9}], Fits0];

spacing = Mean[(x2 - x1) /. (BestFitParameters /. Fits0)]

35.1717

x1Average = Mean[(x1) /. (BestFitParameters /. Fits0)]

125.488

x2Average = Mean[(x2) /. (BestFitParameters /. Fits0)]

160.66

sigmaAverage = Mean[(Σ) /. (BestFitParameters /. Fits0)]

7.84919

Fits0[[5]]

{EstimatedVariance --- 4.22912 x 10-7,
BestFit --- 6.7212 + 0.0000328559 (-161.095 + x) - 6.90649 x 10-7 (-161.095 + x) -
0.00179478 Erf[0.0828625 (-161.095 + x)] - 0.00329766 Erf[0.0828625 (-125.098 + x)],
BestFitParameters --- {A --- 6.7212, B --- 0.0000328559, B2 --- -6.90649 x 10-7,
C1 --- -0.00659532, C2 --- -0.00358955, x1 --- 125.098, x2 --- 161.095, Σ --- 8.5335},

ParameterCITable ---


|    | Estimate                    | Asymptotic SE              | CI                                                           |
|----|-----------------------------|----------------------------|--------------------------------------------------------------|
| A  | 6.7212                      | 0.0000235442               | {6.72115, 6.72125}                                           |
| B  | 0.0000328559                | 5.31953 x 10 <sup>-7</sup> | {0.0000318131, 0.0000338986}                                 |
| B2 | -6.90649 x 10 <sup>-7</sup> | 4.39118 x 10 <sup>-9</sup> | {-6.99257 x 10 <sup>-7</sup> , -6.82042 x 10 <sup>-7</sup> } |
| C1 | -0.00659532                 | 0.0000559345               | {-0.00670497, -0.00648568}                                   |
| C2 | -0.00358955                 | 0.0000422566               | {-0.00367238, -0.00350672}                                   |
| x1 | 125.098                     | 0.117714                   | {124.868, 125.329}                                           |
| x2 | 161.095                     | 0.21706                    | {160.669, 161.52}                                            |
| Σ  | 8.5335                      | 0.127536                   | {8.2835, 8.7835}                                             |



Length[Fits0]

6

Length[DAQFiles]

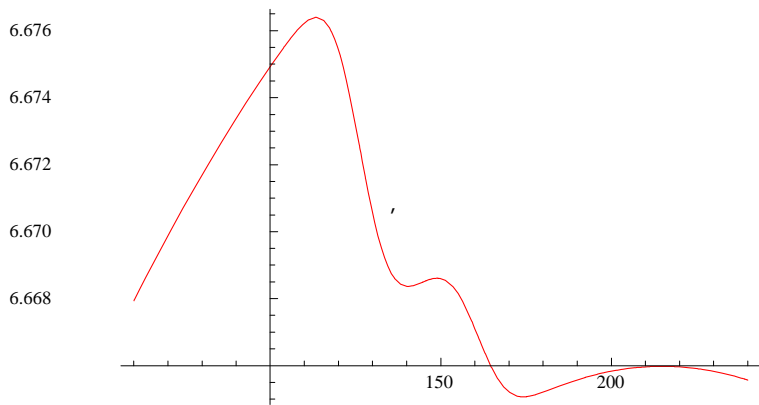
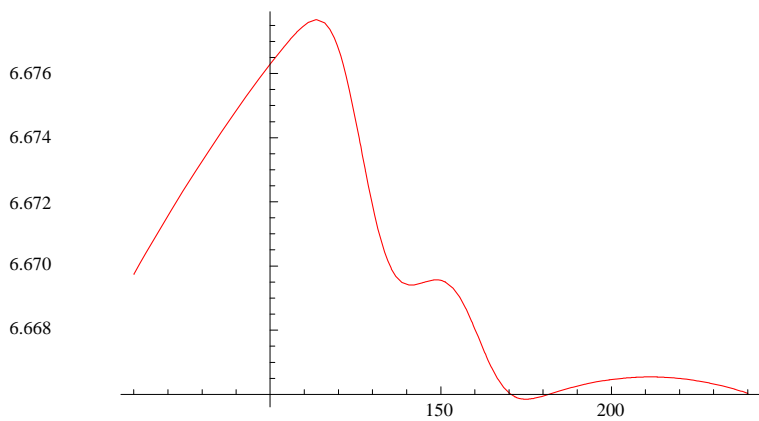
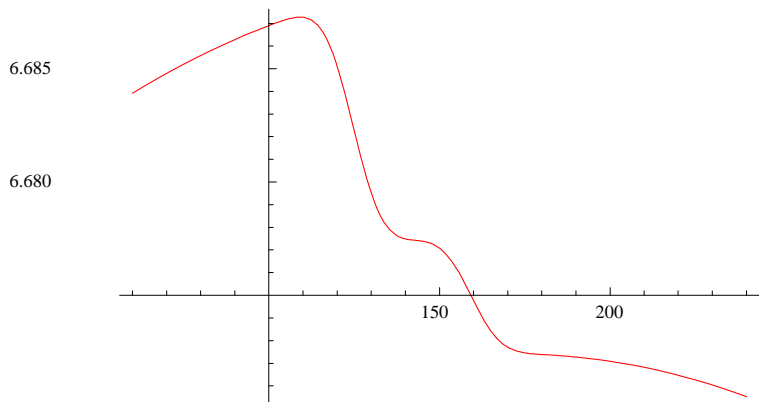
18

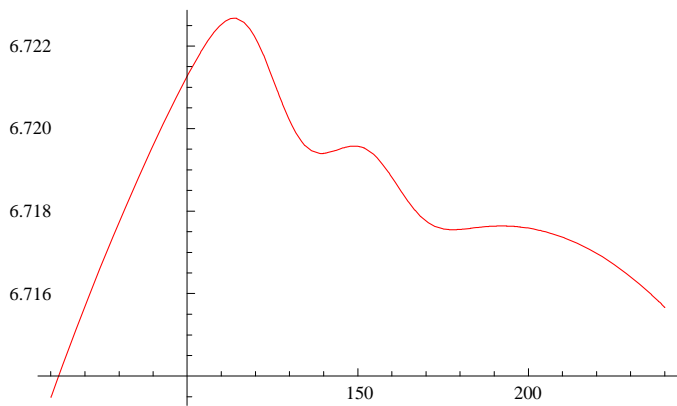
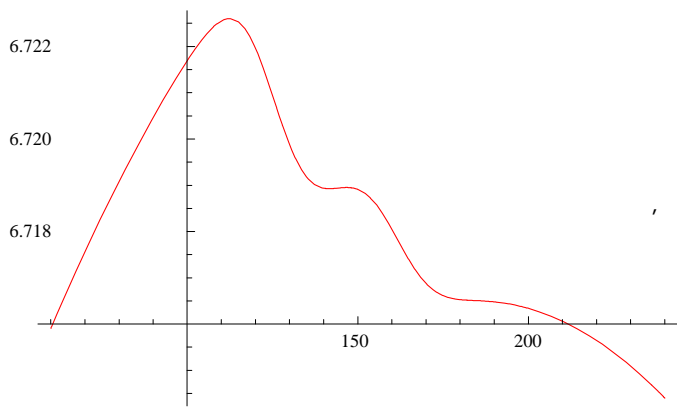
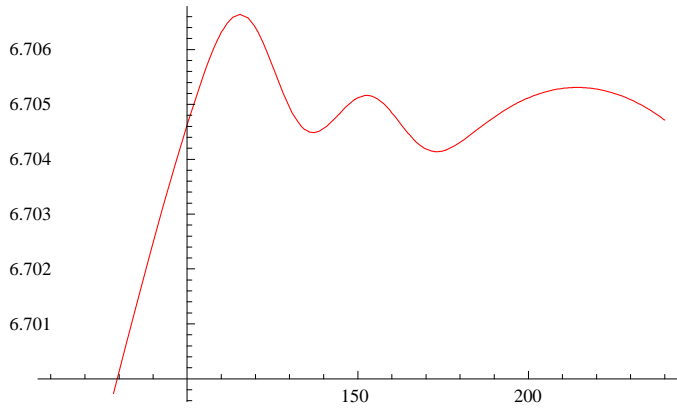
bestFitFunctionOut[x_] = Table[BestFit /. Fits0[[i]], {i, 1, 6}];

bestFitFunctionOut[x];

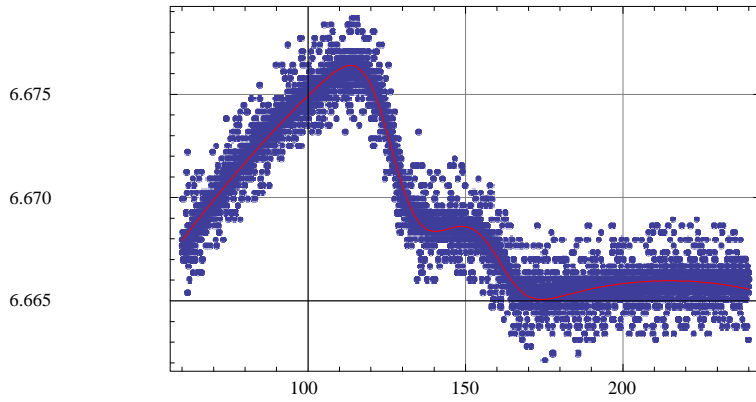
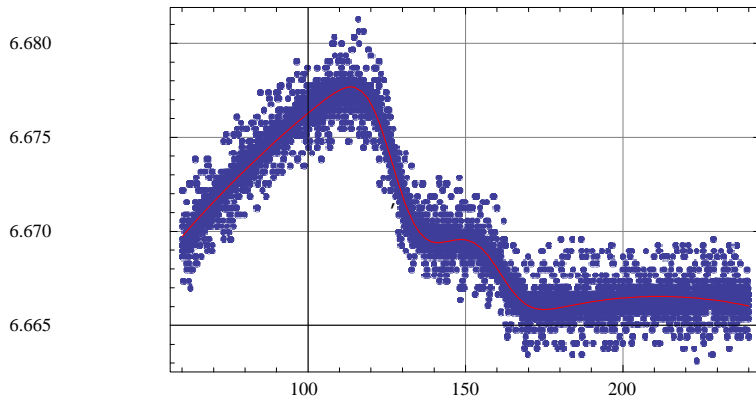
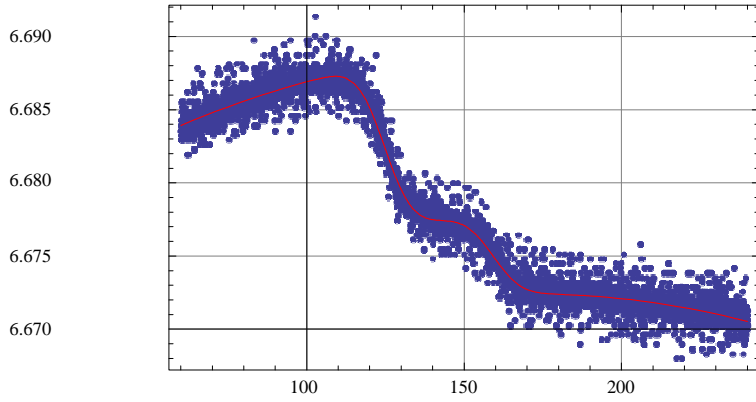
p5 = Table[Plot[bestFitFunctionOut[x][[i]],
{x, inputData1[[i]][[1]][[1]], inputData1[[i]][[-1]][[1]]}, PlotStyle -+ Hue[0]], {i, 1, 6}]

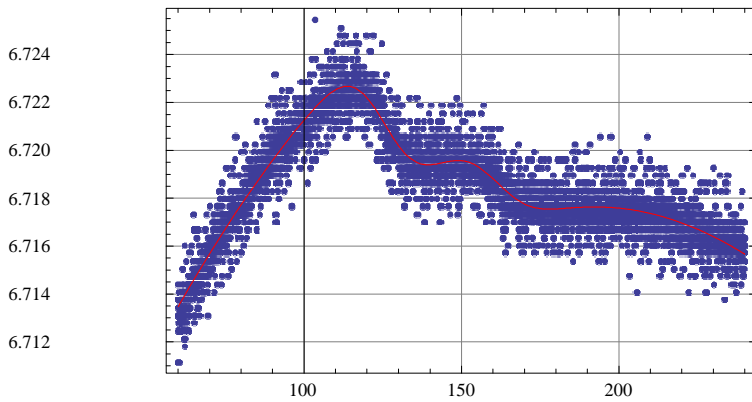
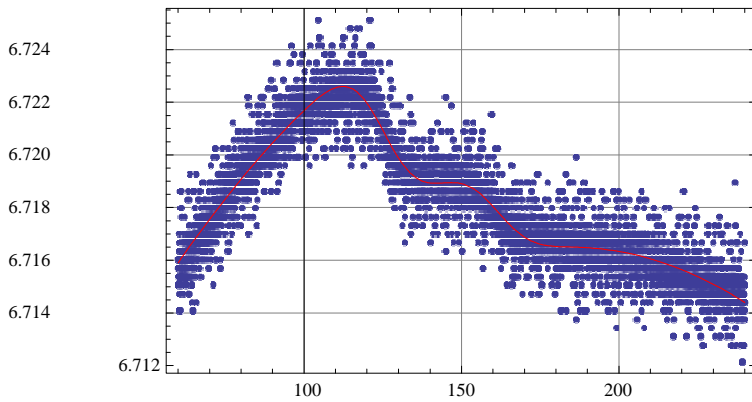
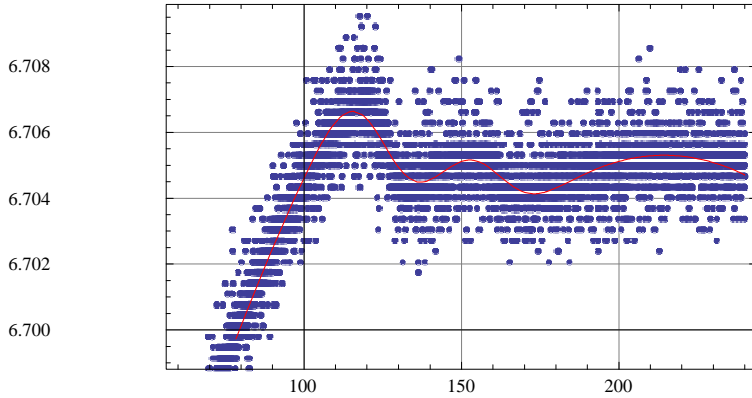
```





Table[Show[p3[[i]], p5[[i]]], {i, 6}]





### Fit with Erf[x] all the same width

```

fitFunct[x_] =
A + B * (x - x2) + B2 * (x - x2)^2 + C1 / 2 * Erf[(x - x1) /           $\sqrt{2} / \Sigma J + C2 / 2 * Erf[(x - x2) / \sqrt{2} / \Sigma J / .$ 
{x1 -+ x1Average, x2 -+ x2Average,  $\Sigma$  -+ sigmaAverage}
A + B (-160.66 + x) + B2 (-160.66 + x) +
1          C2 Erf[0.0900866 (-160.66 + x)] +           $\frac{1}{2} - C1 Erf[0.0900866 (-125.488 + x)]$ 
2
    
```

```

AGuess = Table[(inputData1[[i]][[1]][[2]] + inputData1[[i]][[-1]][[2]]) / 2., {i, 1, 18}]
{6.67741, 6.66832, 6.66669, 6.69932, 6.7162, 6.71539, 6.7076, 6.68861, 6.69348,
6.66783, 6.68568, 6.68991, 6.71019, 6.7063, 6.70646, 6.69396, 6.70321, 6.70484}

BGuess = Table[.000001, {i, 1, 18}]
B2Guess = Table[-.00000001, {i, 1, 18}]
{1. x 10-6, 1. x 10-6,
1. x 10-6, 1. x 10-6, 1. x 10-6, 1. x 10-6, 1. x 10-6, 1. x 10-6, 1. x 10-6, 1. x 10-6}

{-1. x 10-8, -1. x 10-8,
-1. x 10-8, -1. x 10-8, -1. x 10-8, -1. x 10-8, -1. x 10-8, -1. x 10-8, -1. x 10-8, -1. x 10-8}

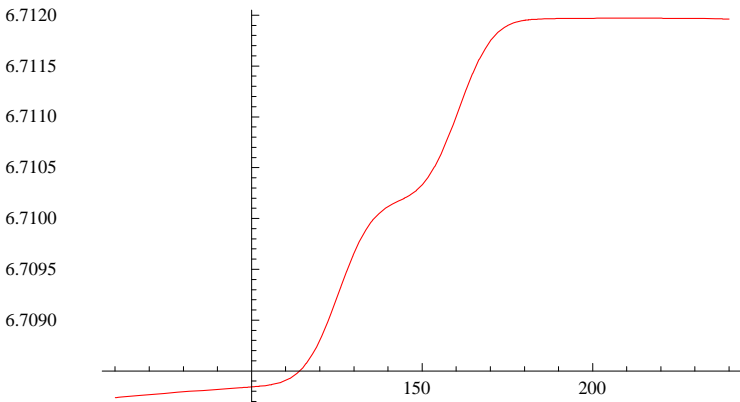
CGuess = 0.3 * Table[(inputData1[[i]][[-1]][[2]] - inputData1[[i]][[1]][[2]]), {i, 1, 18}]
{-0.00370076, -0.00233732, -0.00058433, 0.00321382, 0.000292165, 0.000584331,
-0.000194777, 0.00516158, 0.00262949, 0.00769368, 0.0041877, 0.00379815,
0.00175299, 0.00175299, 0.000292165, 0.00155821, 0.0016556, 0.00223993}

stepTimes2
{{127.96, 163.96}, {124.96, 161.96}, {122.96, 157.96}, {135.96, 163.96},
{127.96, 158.96}, {121.96, 157.96}, {127.96, 151.96}, {120.96, 151.96},
{131.96, 159.96}, {147.96, 189.96}, {127.96, 160.96}, {121.96, 156.96}}

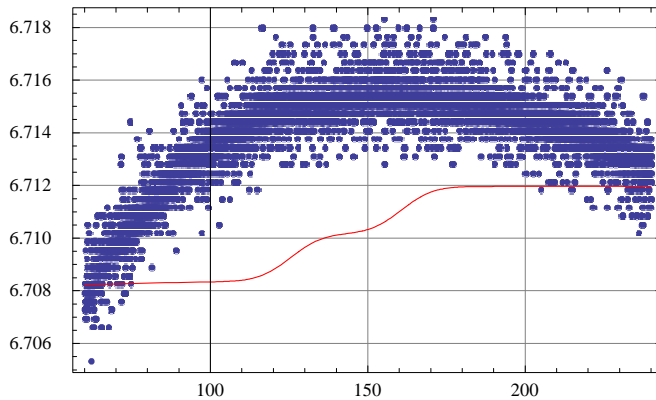
jj = 13;
test[x_] = fitFunct[x] /.
  {A -> AGuess[[jj]], B -> BGuess[[jj]], B2 -> B2Guess[[jj]], C1 -> CGuess[[jj]], C2 -> CGuess[[jj]]}
6.71019 + 1. x 10-6 (-160.66 + x) - 1. x 10-8 (-160.66 + x) +
0.0900866 (-160.66 + x)] + 0.000876496 Erf[0.0900866 (-125.488 + x)]

p4 = Plot[test[x], {x, inputData1[[jj]][1][1], inputData1[[jj]][-1][1]}, PlotStyle -> Hue[0]]

```



```
Show[p3[jj], p4]
```



```
Fits1 = Table[NonlinearRegress[inputData1[j], fitFunc[x], {{A, AGuess[j]}, {B, BGuess[j]},
{B2, B2Guess[j]}, {C1, CGuess[j]}, {C2, CGuess[j]}}, {x}, RegressionReport --
{EstimatedVariance, BestFit, BestFitParameters, ParameterCITable}], {j, 7, 18}]; Fits =
```

```
Join[Fits0, Fits1];
```

```
Fits[[7]]
```

```
{EstimatedVariance --- 3.93815 x 10-7,
```

```
BestFit --- 6.71223 + 0.0000149365 (-160.66 + x) - 5.46275 x 10-7 (-160.66 + x) - 2
0.00100628Erf[0.0900866 (-160.66 + x)] - 0.00172796Erf[0.0900866 (-125.488 + x)],
```

```
BestFitParameters --- {A --- 6.71223, B --- 0.0000149365, B2 --- -5.46275 x 10-7,
```

```
C1 --- -0.00345592, C2 --- -0.00201257},
```

Estimate		Asymptotic SE	CI
A	6.71223	0.00001713	{6.71219, 6.71226}
B	0.0000149365	4.05095 x 10 <sup>-7</sup>	{0.0000141424, 0.0000157305 }
ParameterCITable --- B2 -5.46275 x 10 <sup>-7</sup>	3.6213 x 10 <sup>-9</sup>		{-5.53373 x 10 <sup>-7</sup> , -5.39176 x 10 <sup>-7</sup> }
C1 -0.00345592		0.0000382708	{-0.00353094, -0.0033809}
C2 -0.00201257		0.0000337869	{-0.0020788, -0.00194634}

```
Length[Fits]
```

```
18
```

```
Length[DAQFiles]
```

```
18
```

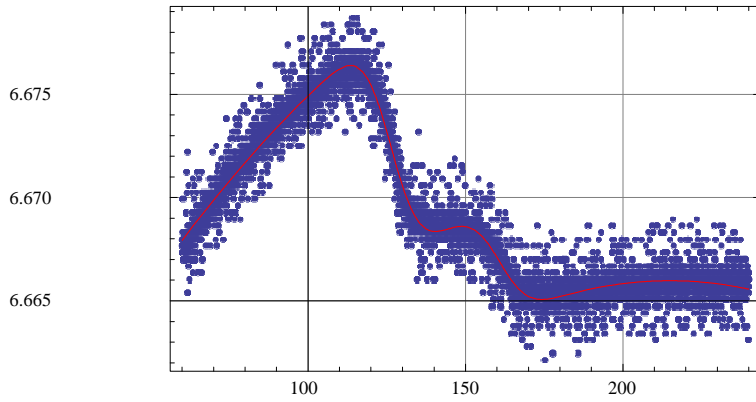
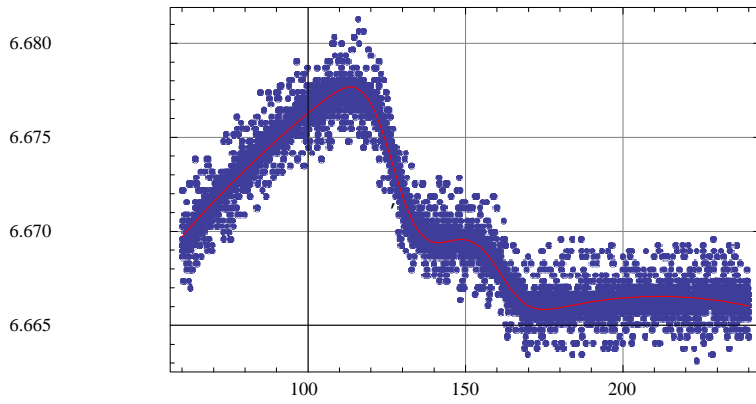
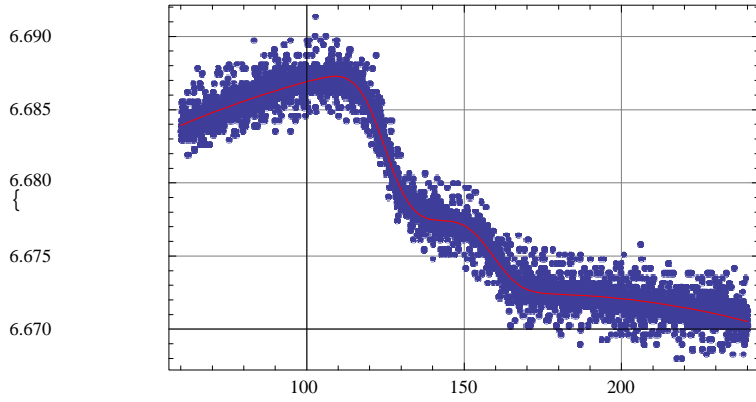
```
bestFitFunctionOut[x_] = Table[BestFit /. Fits[[i]], {i, Length[DAQFiles]}];
```

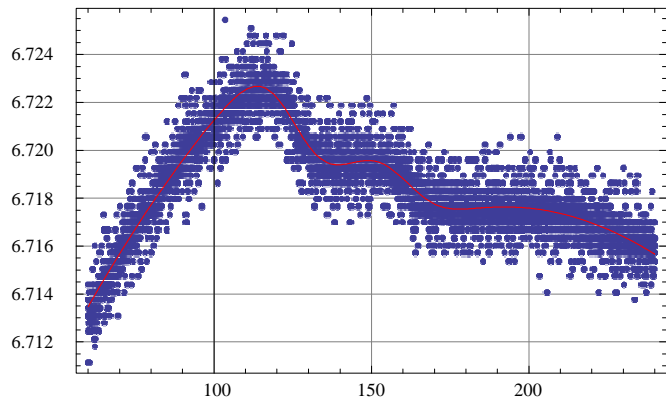
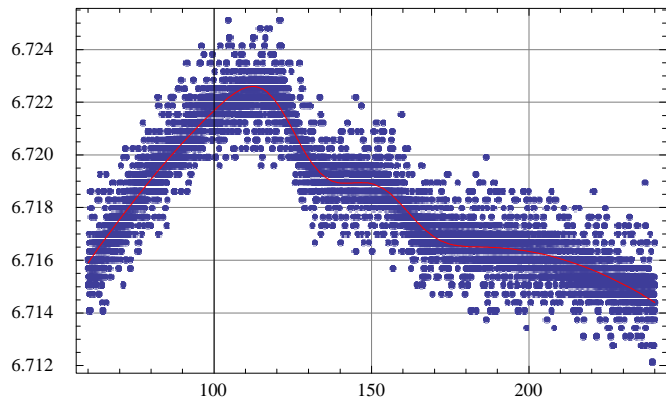
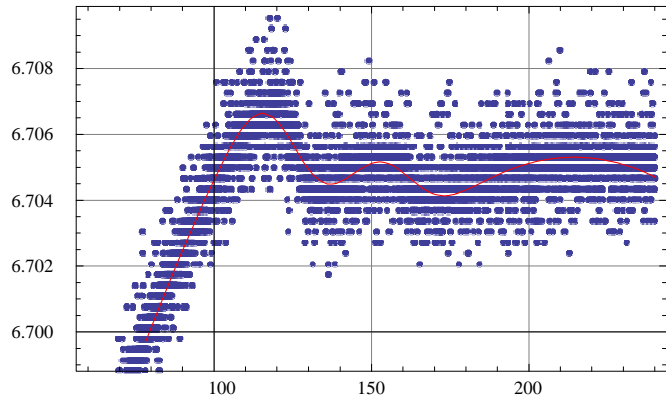
```
bestFitFunctionOut[x];
```

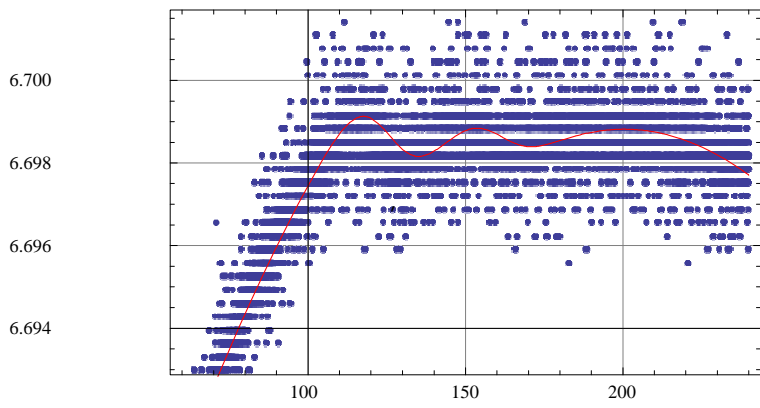
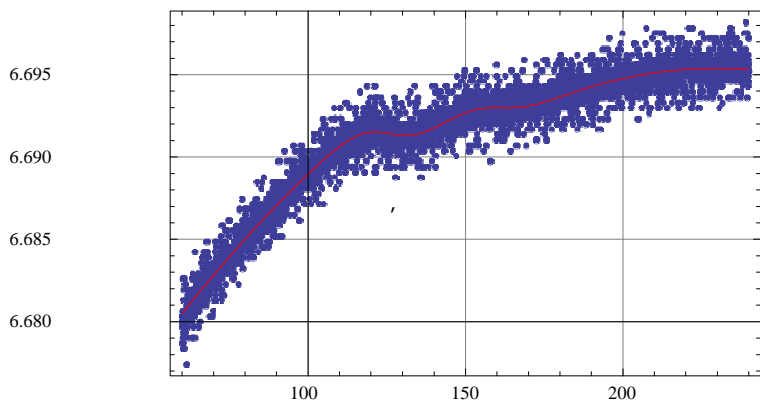
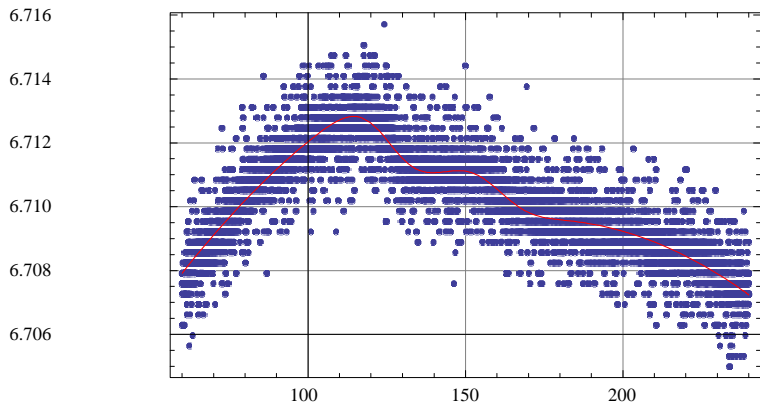
```
p5 = Table[Plot[bestFitFunctionOut[x][[i]], {x, inputData1[[i]][[1]][[1]],
```

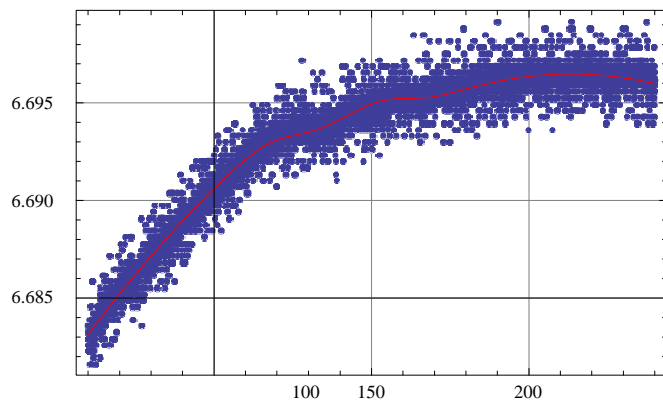
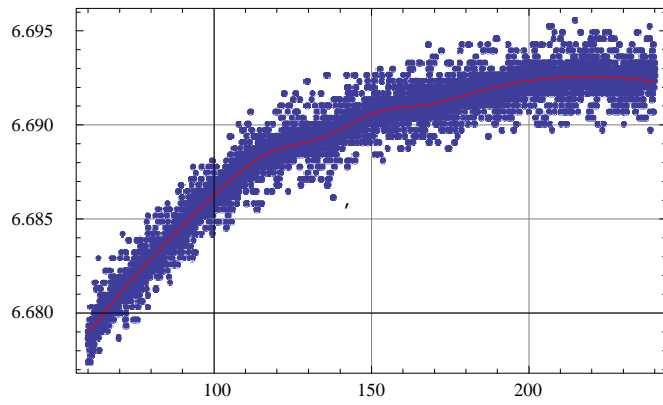
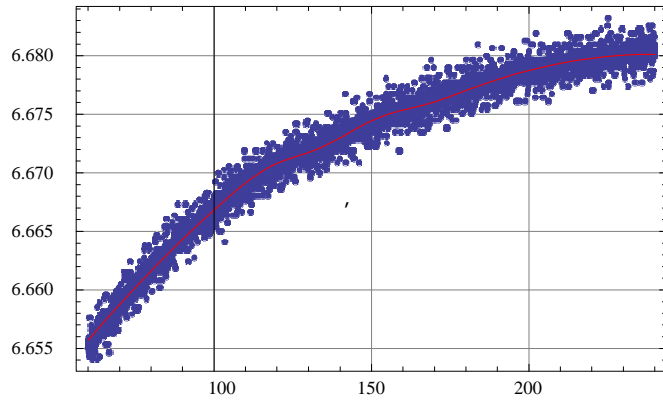
```
inputData1[[i]][[-1]][[1]], PlotStyle --> Hue[0]], {i, 1, Length[DAQFiles]}]; Table[Show[p3[[i]],
```

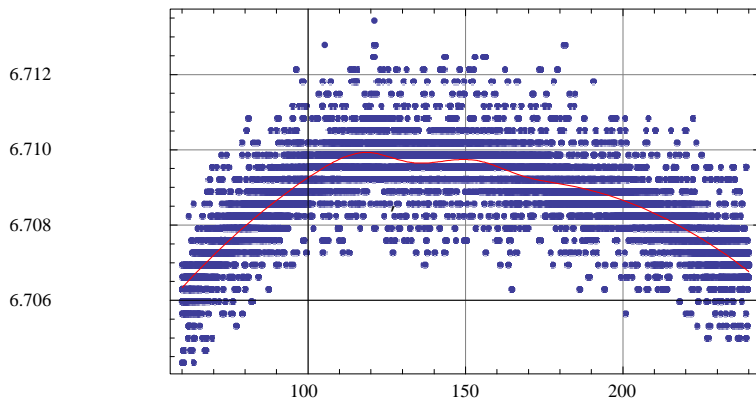
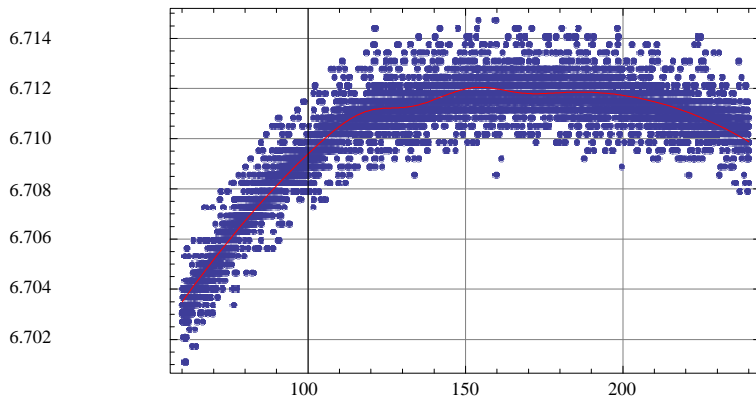
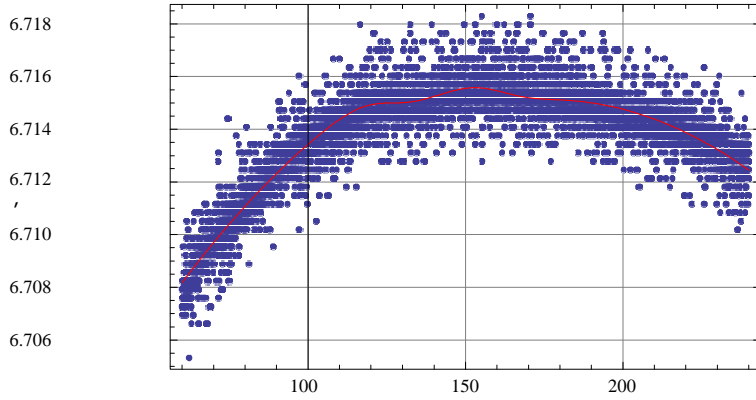
```
p5[[i]], {i, Length[DAQFiles]}]
```

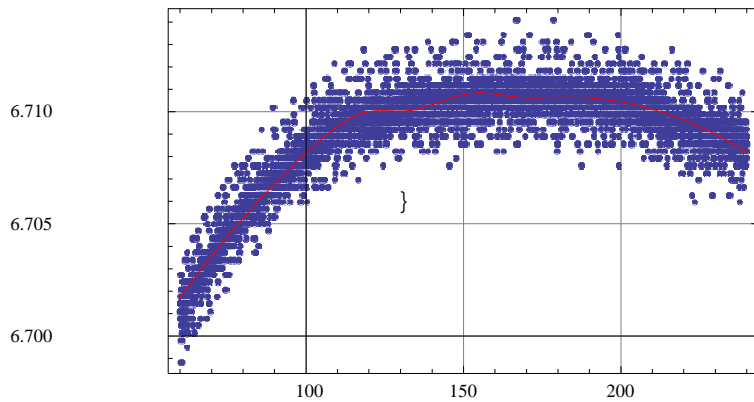
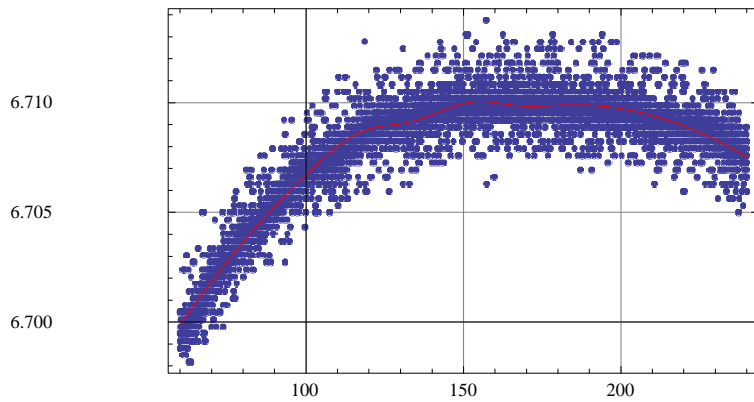
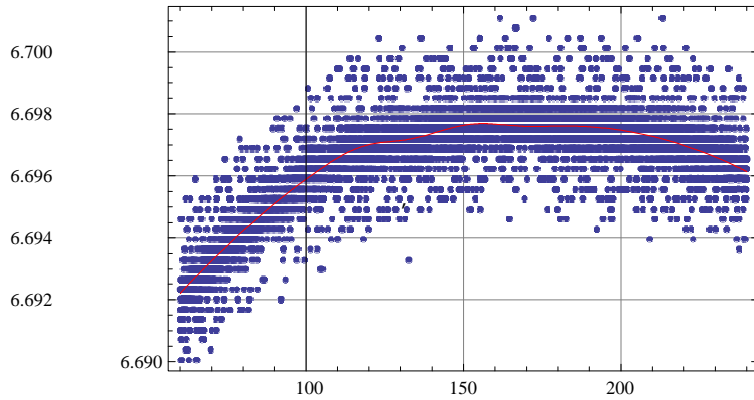












## Results

Phosphate = C1 /. (BestFitParameters /. Fits)

```
{-0.0112418, -0.0117722, -0.0117861, -0.00726962, -0.00659532, -0.00718043,
-0.00345592, -0.00352176, -0.0038112, -0.00228148, -0.00176821, -0.00176654,
-0.00131972, -0.00158538, -0.00117727, -0.000820862, -0.00158291, -0.00187607}
```

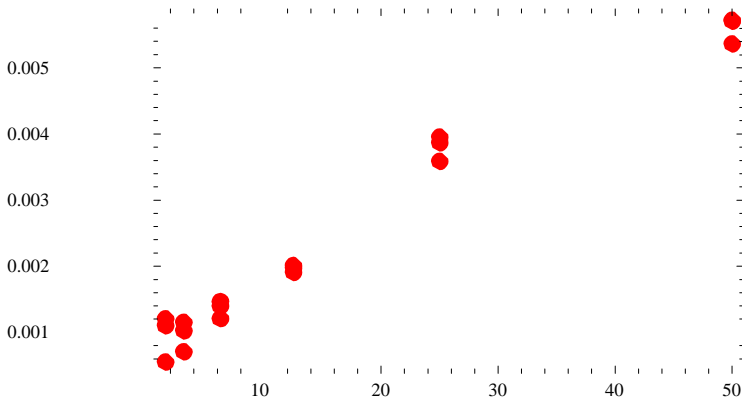
```
ArsenateFromFit = C2 /. (BestFitParameters /. Fits)
```

```
{-0.00536682, -0.00570978, -0.00572319, -0.00395418, -0.00358955, -0.00386768,
-0.00201257, -0.00197393, -0.00190817, -0.00146508, -0.00121101, -0.00140112,
-0.00102689, -0.001154, -0.00071068, -0.000554808, -0.00120706, -0.00110315}
```

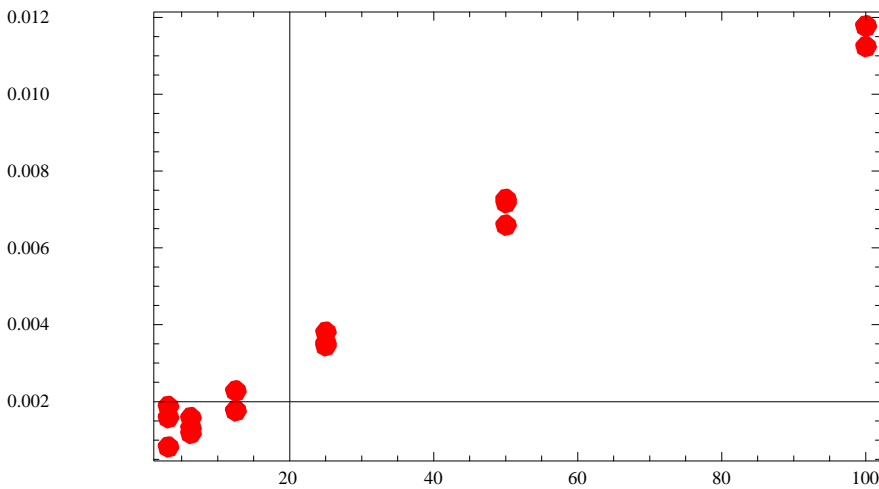
```
ArsenateConcentrations = {50, 50, 50, 25, 25, 25, 12.5, 12.5,
12.5, 6.25, 6.25, 6.25, 3.125, 3.125, 3.125, 1.5625, 1.5625, 1.5625};
```

```
PhosphateConcentrations =
{100, 100, 100, 50, 50, 50, 25, 25, 25, 12.5, 12.5, 12.5, 6.25, 6.25, 6.25, 3.125, 3.125, 3.125};
```

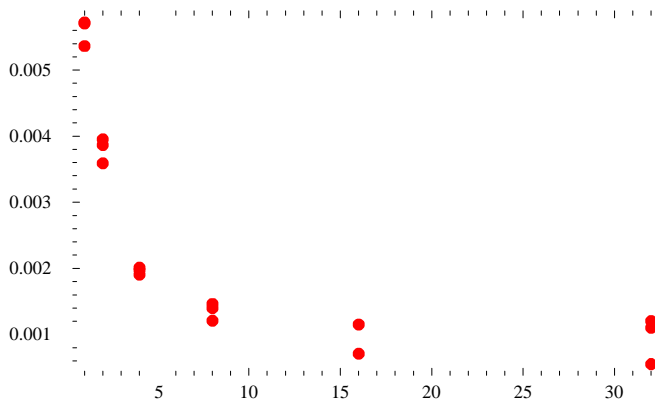
```
p6 = ListPlot[Transpose[{ArsenateConcentrations, (ArsenateFromFit * - 1)}], PlotStyle -+
{Hue[0], PointSize[0.03]}, PlotRange -+ All, Frame -+ True]
```



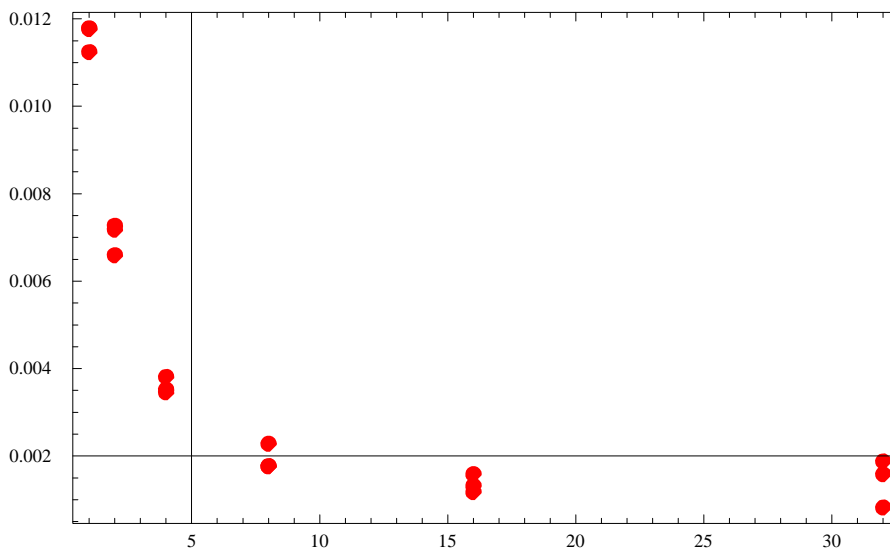
```
ListPlot[Transpose[{PhosphateConcentrations, (Phosphate * - 1)}], PlotStyle -+
{Hue[0], PointSize[0.03]}, PlotRange -+ All, Frame -+ True]
```



```
DilutionFactor = {1, 1, 1, 2, 2, 2, 4, 4, 4, 8, 8, 8, 16, 16, 16, 32, 32, 32};
ListPlot[Transpose[{DilutionFactor, (ArsenateFromFit* - 1)}],
PlotStyle -> {Hue[0], PointSize[0.02]}, PlotRange -> All, Frame -> True]
```



```
ListPlot[Transpose[{DilutionFactor, (Phosphate*-1)}],
PlotStyle -> {Hue[0], PointSize[0.02]}, PlotRange -> All, Frame -> True]
```



```

ArsenateRegress = NonlinearRegress[
Transpose[{ArsenateConcentrations, ArsenateFromFit}], A + B x, {{A, 1}, {B, 1}}, {x}][
ToString[{BestFit, BestFitParameters, ParameterCITable, FitResiduals}]]

{BestFitParameters --- {A --- -0.000794706, B --- -0.000100351},
Estimate
ParameterCITable ---


|   |              | Asymptotic SE              | CI                            |
|---|--------------|----------------------------|-------------------------------|
| A | -0.000794706 | 0.000101412                | {-0.00100969, -0.000579723}   |
| B | -0.000100351 | 4.30306 x 10 <sup>-6</sup> | {-0.000109473, -0.0000912291} |


EstimatedVariance --- 9.5407 x 10-8,



|                       | DF | SumOfSq                    | MeanSq                    |
|-----------------------|----|----------------------------|---------------------------|
| Model                 | 2  | 0.000159149                | 0.0000795746              |
| ANOVA Table --- Error | 16 | 1.52651 x 10 <sup>-6</sup> | 9.5407 x 10 <sup>-8</sup> |
| Uncorrected Total     | 18 | 0.000160676                |                           |
| Corrected Total       | 17 | 0.0000534149               |                           |


AsymptoticCorrelationMatrix ---


|  |           |           |
|--|-----------|-----------|
|  | 1.        | -0.696143 |
|  | -0.696143 | 1.        |


FitCurvatureTable ---


|                       | Max Intrinsic | Curvature |
|-----------------------|---------------|-----------|
|                       |               | 0         |
| Max Parameter-Effects |               | 0         |

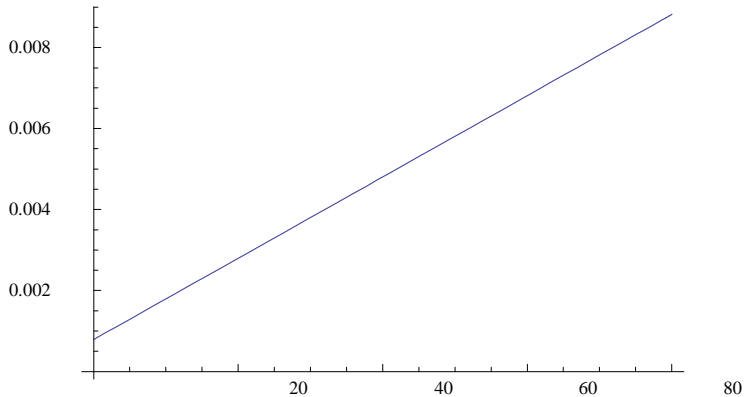

95. % Confidence Region 0.524595
{BestFit, BestFitParameters, ParameterCITable, FitResiduals}]

```

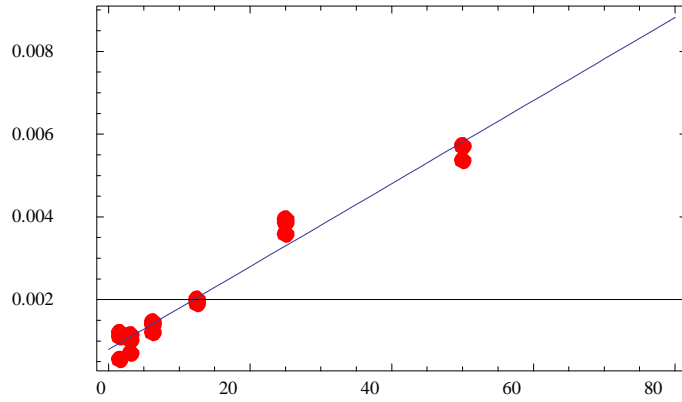
```
lm = LinearModelFit[Transpose[{ArsenateConcentrations, (ArsenateFromFit * -1)}], {x}, {x}]
```

```
FittedModel[ 0.000794706 + 0.000100351 x ]
```

```
p22 = Plot[lm["BestFit"], {x, 0, 80}]
```



```
Show[p6, p22]
```



```
noise1 = StandardDeviation[lm["FitResiduals"]]
```

```
0.000299658
```

```
Solve[(lm["BestFit"] /. x -> 0) == (lm["BestFit"] /. x -> y) - noise1 * 3, y]
```

```
{{y -> 8.95827}}
```

### A.3 Unknown species in tap water

Separations of  $\text{H}_2\text{PO}_4^-$  and  $\text{H}_2\text{AsO}_4^-$  in pH = 3.0 run buffer diluted with tap water show an unknown species that elutes with  $\text{H}_2\text{AsO}_4^-$  (Figure 2.6). To confirm the presence of the unknown, run buffer diluted 2× with tap water and a 100  $\mu\text{mol/L}$   $\text{NaH}_2\text{PO}_4$  sample diluted 2× with tap water (to a final concentration of 50  $\mu\text{mol/L}$   $\text{NaH}_2\text{PO}_4$ ) were separated. The unknown is present in both samples around a time of approximately 310 s, which corresponds to the elution time of  $\text{H}_2\text{AsO}_4^-$ . It is also important to note that some  $\text{H}_2\text{PO}_4^-$  is present in the run buffer sample that is diluted 2-fold with tap water, however the signal is difficult to see because of the large difference in concentration when compared to the 50  $\mu\text{mol/L}$   $\text{H}_2\text{PO}_4^-$  signal.

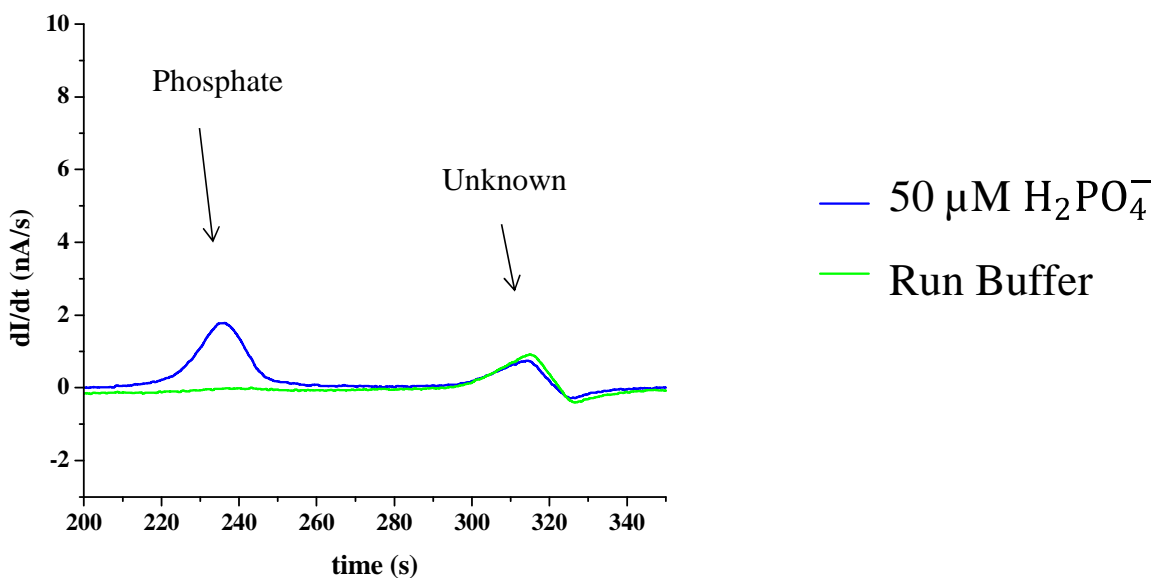


**Figure A.3:** GEMBE separation of run buffer diluted 2× with tap water (green) and of a 100  $\mu\text{M}$   $\text{NaH}_2\text{PO}_4$  sample diluted 2× with tap water (blue). In both separations, an unknown species elutes around 310 s. This unknown elutes with  $\text{H}_2\text{AsO}_4^-$  (Figure 2.6).

## A.4 Repeated separations of Figure 3.1 and 3.2

### A.4.1 (Figure 3.1 repeated):

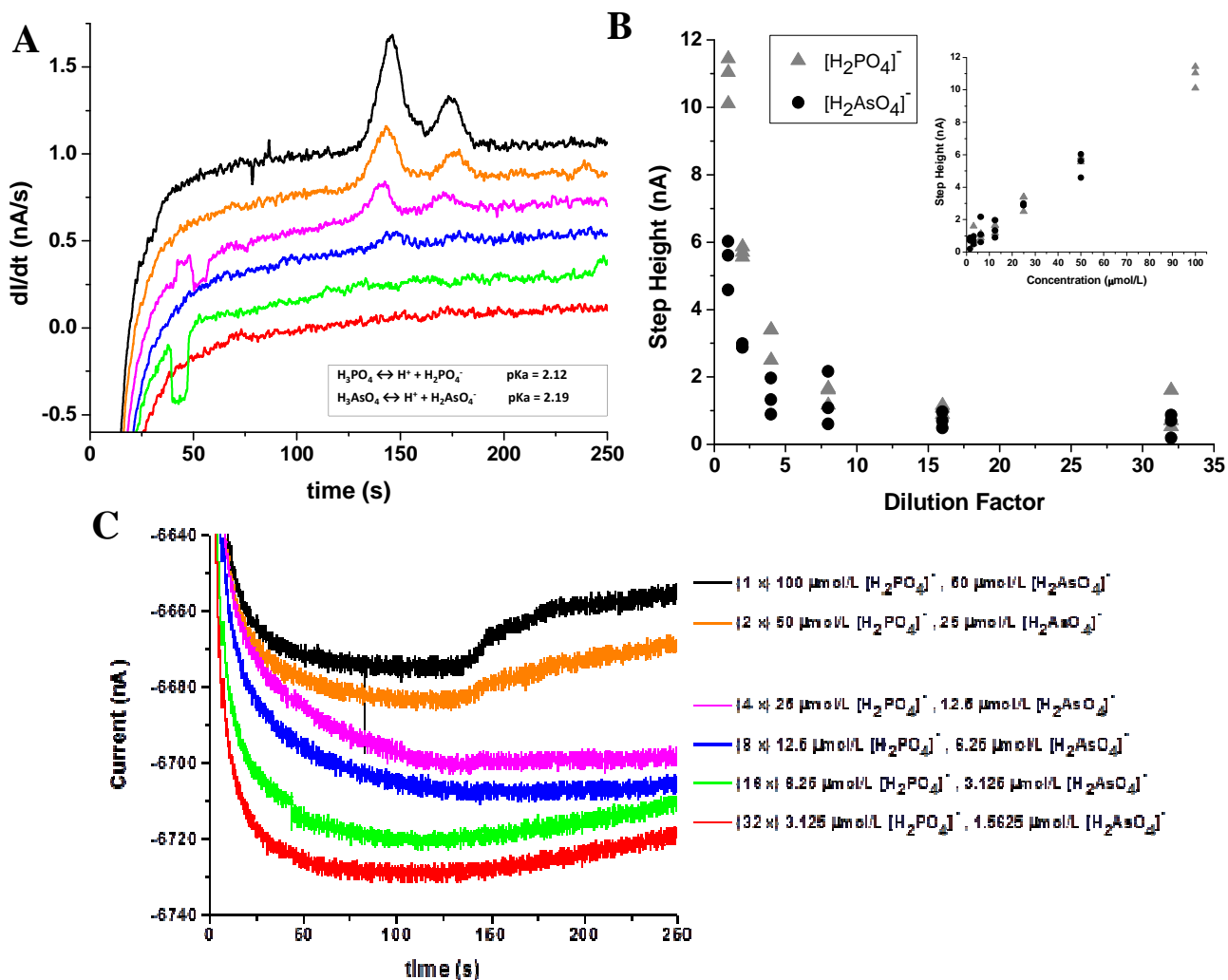


**Figure A.4.1.** GEMBE for samples prepared via a serial 2-fold dilution of 100  $\mu\text{M}$   $\text{NaH}_2\text{PO}_4$  (left peak), 50  $\mu\text{M}$   $\text{Na}_2\text{HAsO}_4$  (right peak). Dilutions were performed with run buffer so that the sample conductivity was the same as the run buffer conductivity. (A) Time derivative of the current vs. time. Dilution factor increases from top to bottom as indicated in (C) from 1× to 32×. (Inset – species of interest). (B) Step height (equivalent to the peak area from panel A) vs dilution factor. As the samples are progressively diluted and as the analyte concentration decreases, the signal decreases. The LOD for  $\text{H}_2\text{AsO}_4^-$  is approximately 12  $\mu\text{mol/L}$  (signal to noise ratio equal to 3). (Inset – step height from (A) vs concentration). (C) Raw current as a function of time data. Step identities are the same as those in (A).

Figure A.4.2 (Figure 3.4 repeated):

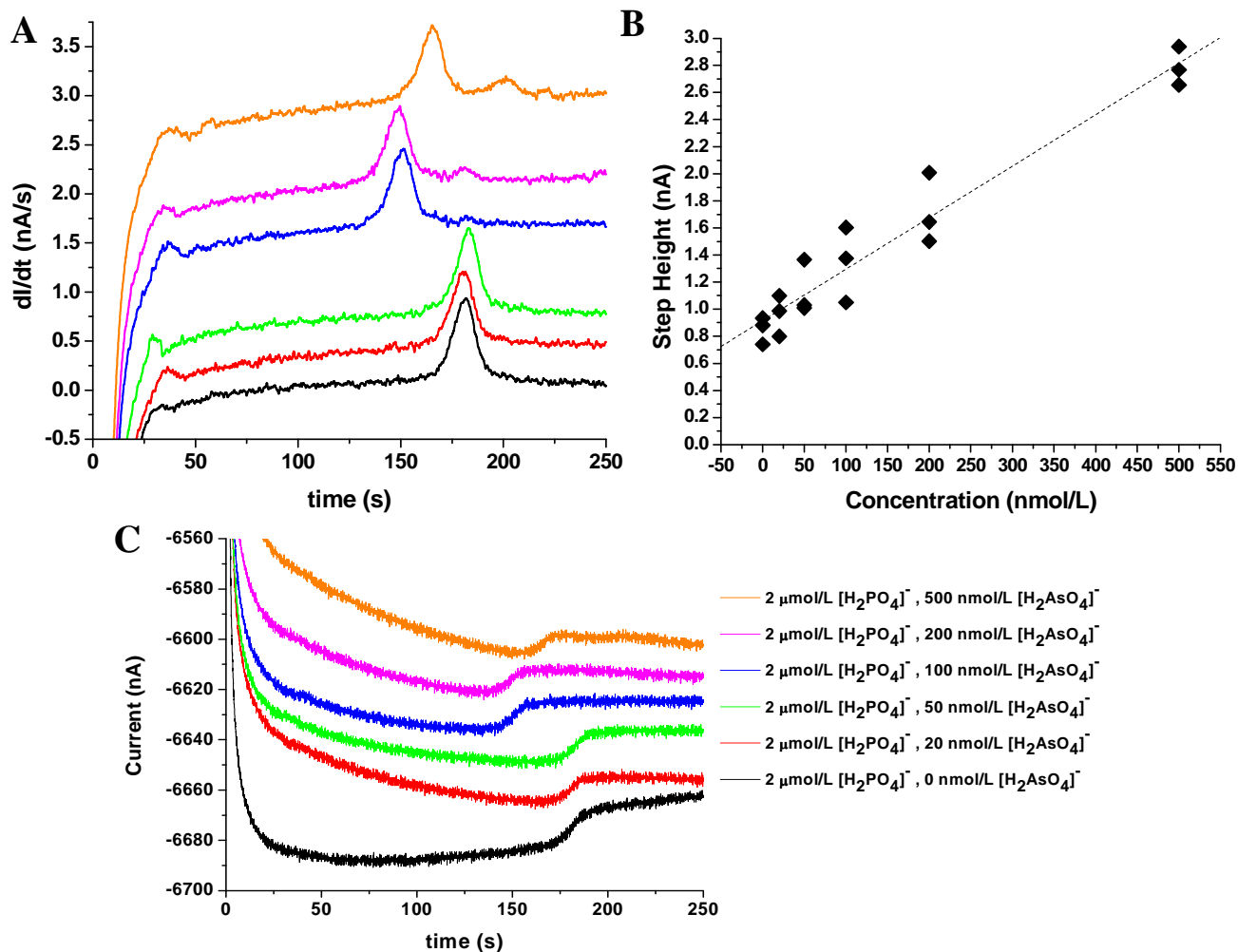


**Figure A.4.2.** FACS-GEMBE data with sample buffer diluted  $10\times$  (with DI water) relative to the run buffer. (A) Time derivative of the current vs. time. Phosphate concentration (left peak) is held constant at  $2 \mu\text{mol/L}$  and arsenate concentration (right peak) is decreased from top to bottom:  $500 \text{ nmol/L}$ ,  $200 \text{ nmol/L}$ ,  $100 \text{ nmol/L}$ ,  $50 \text{ nmol/L}$ ,  $20 \text{ nmol/L}$ ,  $10 \text{ nmol/L}$ ,  $0 \text{ nmol/L}$ . (B) Step height (equal to peak area from A) vs. concentration. The LOD for arsenate is reduced approximately 67 fold from  $10 \mu\text{mol/L}$  (Fig. 2) to  $150 \text{ nmol/L}$ . The dotted line represents a linear least-squares fit to all data points.

## A.5 Calculations

### A.5.1 Limit of detection calculations

Figure 3.1(B): LOD was determined using arsenate data in the concentration range from zero to 50  $\mu\text{mol/L}$ . The slope of the fit line was  $0.100 \text{ nAL}/\mu\text{mol}$ . The standard deviation (SD) of the fit residuals was  $0.300 \text{ nA}$ . The LOD was taken to be  $3 \times \text{SD}/\text{slope}$ .

Figure 3.4(B): LOD was determined using arsenate data in the concentration range from zero to 500  $\text{nmol/L}$ . The slope of the fit line was  $2.760 \text{ nAL}/\mu\text{mol}$ . The standard deviation (SD) of the fit residuals was  $0.132 \text{ nA}$ . The LOD was taken to be  $3 \times \text{SD}/\text{slope}$ .

Figure 3.5: LOD was determined using arsenate data in the concentration range from zero to 500  $\text{nmol/L}$ . The slope of the fit line was  $2.136 \text{ nAL}/\mu\text{mol}$ . The standard deviation (SD) of the fit residuals was  $0.144 \text{ nA}$ . The LOD was taken to be  $3 \times \text{SD}/\text{slope}$ .

### A.5.2 Comparison of Figures 3.1 and 3.2

For FACSI-GEMBE with sample buffer diluted (with DI water)  $16 \times$  relative to run buffer:

Measured conductivity:

$1 \times$  run buffer =  $6.54 \text{ mS/cm}$  (no dilution with DI water)

$16 \times$  run buffer =  $0.796 \text{ mS/cm}$  ( $16 \times$  dilution with DI water)

Calculated conductivity Ratio:  $(6.54 \text{ mS/cm}) / (0.796 \text{ mS/cm}) = 8.21$

Step height (phosphate signal) at final concentration of  $6.25 \mu\text{mol/L}$ :

With FACSI (sample buffer diluted  $16 \times$  with DI water) =  $75.6$

Without FACSI\* (sample buffer equal to run buffer) =  $0.1097 * 6.25 = 0.686$

\*signal extrapolated to low concentration using the slope of the calibration curve (see Figure 2 inset)

Signal enhancement =  $75.6/0.686 = 110.2$

### A.5.3 Limit of detection improvement: run buffer versus tap water

Measured conductivity:

Run buffer: 6.54 mS/cm

Run buffer diluted 10× with tap water: 1.102 mS/cm\*

\*determined from fit of conductivity data for run buffer diluted with tap water (Figure 3.3)

Calculated conductivity ratio:  $(6.54 \text{ mS/cm}) / (1.102 \text{ mS/cm}) = 5.93$

LOD for arsenate without FACSI (samples prepared in run buffer) = 11.6  $\mu\text{mol/L}$   
(Figure 3.1 and A.4.1: 8.96 and 14.2  $\mu\text{mol/L}$ )

LOD for arsenate with FACSI (samples = 9 parts tap water, 1 part run buffer) = 203 nmol/L =  
0.203  $\mu\text{mol/L}$   
(Figure 3.5: 203 nmol/L)

LOD improvement:  $(11.6 \text{ } \mu\text{mol/L}) / (0.203 \text{ } \mu\text{mol/L}) = 57.1\times$  improvement

### A.5.4 Limit of detection improvement: run buffer versus DI water

Measured conductivity:

Run buffer: 6.54 mS/cm

Run buffer diluted 10× with tap water: 1.004 mS/cm\*

\*determined from fit of conductivity data for run buffer diluted with DI water (Figure 3.3)

Calculated conductivity ratio:  $(6.54 \text{ mS/cm}) / (1.004 \text{ mS/cm}) = 6.52$

LOD for arsenate without FACSI (samples prepared in run buffer) = 11.6  $\mu\text{mol/L}$   
(Figure 3.1 and A.4.1: 8.96 and 14.2  $\mu\text{mol/L}$ )

LOD for arsenate with FACSI (samples = 9 parts tap water, 1 part run buffer) = 140 nmol/L =  
0.140  $\mu\text{mol/L}$   
(Figure 3.4 and A.4.2: 143 and 137 nmol/L)

LOD improvement:  $(11.6 \text{ } \mu\text{mol/L}) / (0.140 \text{ } \mu\text{mol/L}) = 82.9\times$  improvement

### A.5.5 Fits for Figure 3.3

DI water fit:

$$\text{Log}(\text{conductivity}) = (8.88 * 10^{-4} * (\text{Log}(\text{concentration}))^2) + (0.812 * \text{Log}(\text{concentration})) - (0.812)$$

Tap water fit:

$$\text{Log}(\text{conductivity}) = (0.062 * (\text{Log}(\text{concentration}))^2) + (0.589 * \text{Log}(\text{concentration})) - (0.609)$$

## A.6 Instrumentation

### A.6.1 Sputter coating

Sputter coating is used to prepare MAP-fabricated structures and PDMS molds for imaging on a scanning electron microscope (SEM). A sputter coater consists of a chamber that can be evacuated and filled with an inert gas, such as argon. Under a specific pressure, the argon atoms will bombard a metal target, such as platinum/palladium, silver, or gold, and a thin metal (~nm, conductive) layer will fall onto a sample placed below the target. A conductive layer is necessary for SEM to prevent charging of the sample, and the thickness of the metal layer can be adjusted by changing the sputter coating time.

### A.6.2 Scanning electron microscopy

Scanning electron microscopy (SEM) is an imaging technique commonly used to take images of structures that require higher resolution than is available with optical microscopy techniques. SEM provides images of the external morphology of structures by directing a focused beam of electrons on to the surface of a sample. Most commonly secondary or backscattered electrons, which result from the interaction between the focused electron beam and

the sample, are collected above, or beside, the sample and an image of the surface is produced. A secondary electron detector was used with the Amray 1820D SEM to obtain the images included in this document. As mentioned previously, a conductive layer is deposited on the surface of samples for SEM imaging to prevent charging of the surface. Without a conductive layer, a buildup of charge can occur, resulting in distorted images. For imaging of PDMS molds, the PDMS is cut along various axes so that SEM images of channel cross-sections and of channel interiors can be obtained.

#### A.6.3 Plasma cleaning

Plasma cleaning is one way of creating a seal between a glass surface and a PDMS surface. An oxygen plasma cleaner uses oxygen gas ions that are excited to higher energy states to remove impurities and contaminants from a surface. In the case of glass and PDMS, a plasma-cleaned surface consists of primarily  $-OH$  groups. When two surfaces are placed in contact with one another, a condensation reaction occurs and  $H_2O$  is eliminated, resulting in a covalent bond between the surfaces. When plasma cleaned PDMS and glass are placed together, heating in an oven can accelerate the release of  $H_2O$ .

#### A.7 SU-8 epoxy resin: addition of rhodamine

Visualization of fabrication by MAP in an acrylate resin is possible due to the change in refractive index that occurs upon polymerization of the acrylate monomers. Perhaps the most important use of this change in refractive index upon polymerization is the ability to locate the fabrication surface of a sample. Unfortunately, the epoxy resin SU-8 does not result in the same change in refractive index. To allow the fabrication surface to be located in SU-8 resin, a small

amount of Rhodamine B dye (0.01 wt %) can be added. When the resulting resin is exposed to a sufficient wavelength of light, fluorescence can be observed. By locating the onset of fluorescence (which will only occur within the resin) the fabrication surface can be located.

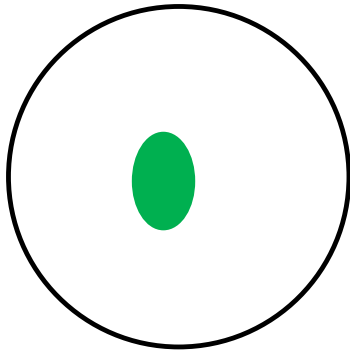
#### A.8 Laser alignment procedures

Some optical components in the laser beam path (Figures 4.9 and 4.10) to the upright microscope and to the inverted microscope are aligned before each use, and others are typically aligned every few months. Before each use, a power meter set to measure 800 nm light is used to measure the power after the pinhole, and before the shutter. The pinhole is typically adjusted before each use, using knobs on the top and side, to maximize the power traveling to the microscope. The optical components that are typically aligned every few months include the majority of the components in Figures 4.9 and 4.10, as well as the optical components inside the laser cavity. To align the laser cavity, the procedure written in the cavity manual is followed, unless an amended procedure has been developed to include the extra steps required to avoid burn spots on damaged optics. The procedures below were compiled on 9/28/12 for alignment of the laser cavity leading to the upright microscope. Alignment of the laser cavity leading to the inverted microscope follows the procedure outlined in the cavity manual.

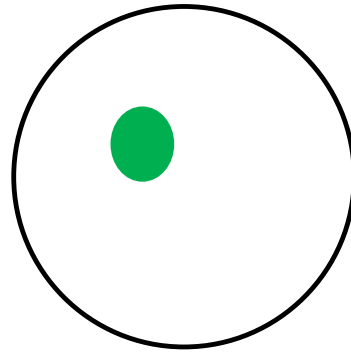
## A.8.1 Upright laser alignment

### Upright Laser Cavity Alignment

1. Check that the Verdi power is set to the value indicated on the white board labeled “Verdi Output”. This value is determined based on the power measured just before the laser beam enters the laser cavity (below).
2. Measure pump power into the cavity; it should be the corresponding value on the white board labeled “Into Upright”.
3. Check positions of the micrometers for the Brewster prism (BP2) and the Birefringence filter. These positions are pre-determined and are indicated on the lid of the laser cavity. For 800 nm, BP2 should be at 16.90, and the birefringence filter should be at 5.91. It is very important that these are set correctly before continuing with the alignment procedure.
4. Check the location of the beam on the pump optics. Unless indicated below, the beam should be centered on all pump optics.



P4



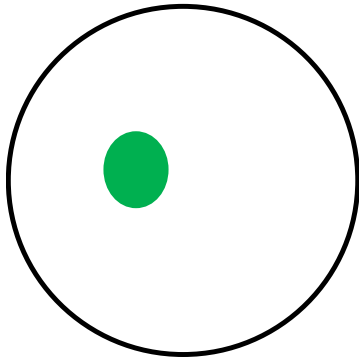
Lens

## Aligning the Auxiliary Cavity

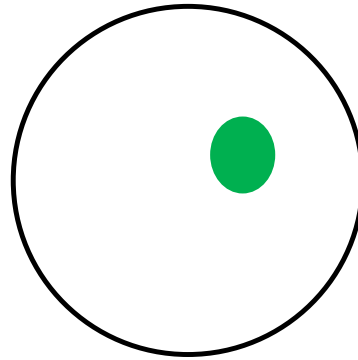
\*Always use a power meter when aligning the laser cavity (placed just before the chirp mirrors). DO NOT rely only on the diode reading.

1. Follow instructions in the laser manual for aligning the auxiliary cavity.
2. Be sure to record the maximum power before switching to the main cavity.
  - a. The beam MUST be lasing at the center of M1, M2, and M3 BEFORE moving into the main cavity.
3. The pump beam should be centered on M8 and M9 (as indicated in the laser manual).
4. The positions of the beam on M1, M2, and M3 will most likely need to be adjusted multiple times in order to maximize the power.
5. Switch to the main cavity by moving BP1 as indicated in the laser manual. (NOTE: you won't always get high power right away.)

\*see the diagram below for mirror and prism locations.



M6



M7

## Aligning the Main Cavity

\*From 9/28/12 – 7/1/14, the positions of M6 and M7 are NOT centered. See below (or Ali's notebook). Deviations from center are a result of burn spots on optics.

1. Adjust M7 to maximize the power in the main cavity.
2. Adjust M5 a small amount to move the beam toward the center of M6. The beam will still be slightly off center. \*
3. Adjust M6 to maximize the power at the new location.
4. Repeat steps 2 and 3 until maximum power is reached. (Remember the direction of movements, and move back if a movement of M5/M6 decreases the power.)
5. Adjust the position of the beam on M7 with M6. Move M6 so the beam moves toward the center of M7. The beam will still be slightly off center.\*
6. Follow the same procedure as steps 2 and 3, using M6 and M7 instead of M5 and M6.
7. Adjust the position of M1 slightly to maximize the power.
8. Replace the slit, and adjust its position to recover the maximum power (from step 7). Record this power.
9. Close the slit half way, switch to ML on the diode display. Check that beam is mode-locked on the diode display, visually (after chirp mirrors), and with the spectrometer (to make sure the beam looks gaussian). Record this power. (NOTE: the diode display may not display "CW", but it is important to check the beam because this is not always correct.)
10. Measure the power after the first pinhole in the beam path. Maximize the power here using the fine controls on the pinhole. Record this power.
11. Check beam alignment on the table to the black box microscope, and to the upright microscope.

## A.9 Sample calculations for acrylate resin preparation

$$0.1608 \text{ g TPO-L} = 0.03 \times x$$

$$x = 5.36$$

$$\underline{-0.1608 \text{ g TPO-L}}$$

$$5.1992 \text{ g monomer}$$

$$\text{SR-499} = 561 \text{ g/mol}$$

$$\text{SR-368} = 423 \text{ g/mol}$$

$$\text{SR-499} + \text{SR-368} = 984 \text{ g/mol}$$

$$(y \text{ mol}) \times (984 \text{ g/mol}) = 5.1992 \text{ g monomer}$$

$$y = 0.0052837398 \text{ mol}$$

$$\text{SR-499} = y \times 561 \text{ g/mol} = 2.9642 \text{ g needed}$$

$$\text{SR-368} = y \times 423 \text{ g/mol} = 2.2350 \text{ g needed}$$

## A.10 Functionalizing glass coverslips or slides

Glass slides or coverslips are functionalized with 3-acryloxypropyl trimethoxysilane (Gelest, Morrisville PA) to promote adhesion of the acrylate polymer structures fabricated using MAP. First, glass slides or coverslips are cleaned by sonication for 5 minutes in a beaker of acetone, followed by isopropanol, and finally DI water. The glass slides or coverslips are then baked in a 95 °C oven for 1 hour, or until all slides are dry. The surface of the glass is cleaned further by oxygen plasma cleaning for 2 to 3 minutes and then placed in a 93% ethanol, 5% DI water, 3% 3-acryloxypropyl trimethoxysilane solution and stirred for 24 hours. The slides or coverslips are then transferred to a beaker of ethanol and stirred for 1 hour. Finally, the slides or

coverslips are removed from the ethanol and baked until dry in a 95 °C oven. For storage, the slides or coverslips are layered with kim wipes in a plastic Petri dish.

## A.11 Sample fabrication programs

### A.11.1 Inverted microscope orientation

The description in Table A.11.1 is for programs to be read by the LabView program “Fabricate Prior” on the computer that communicates with the inverted microscope set-up. For any fabrication program to be used on the inverted microscope set-up, the first three lines as well as the final line are unique. Table A.11.1 includes descriptions of the commands that fill each spot.

	A1	B1	C1	D1	E1
1	2- define fabrication speed ( $\mu\text{m/s}$ )	$x$ speed	$y$ speed	$z$ speed	
2	0 - do nothing	0	$x$ (start)	$y$ (start)	$z$ (start)
3	1- start fabrication (open shutter)	0	$x$ (1)	$y$ (1)	$z$ (1)
4	...	...	...	...	...
5	0	0	$x$ (i)	$y$ (i)	$z$ (i)
6	-1 – end fabrication (close shutter)	0	$x$ (end)	$y$ (end)	$z$ (end)

**Table A.11.1:** Descriptions of the commands for writing a fabrication program to use on the inverted microscope. All  $x$ ,  $y$ , and  $z$  coordinates are in  $\mu\text{m}$ .

### A.11.2 Upright microscope orientation

The description in Table A.11.2 is for programs to be read by the LabView program “Fabricate2.vi” (using the “Bridge” format) on the computer that communicates with the upright microscope set-up. Table Ax includes descriptions of the commands that fill each spot. On the front panel of the LabView program, the stage speed and fabrication time are entered. The fabrication length in the program that is being read by LabView must correspond to the speed

and time input on the front panel. For example, at a stage speed of 5,000  $\mu\text{m/s}$  and a fabrication time of 600 ms, the fabrication length in the program should be 3000  $\mu\text{m}$ . The inclusion of acceleration time is discussed in Section 4.3.

	A1	B1	C1	D1
1	number of layers – number of times the program will be repeated at increasing “dz” values – defines the height of the structure	dz – the spacing in $z$ between layers	bridge – the number of membrane layers	total number of lines in the program (not including line 1)
2	$x(1)$	$y(1)$	$x(2)$	$y(2)$
3	$x(3)$	$y(3)$	$x(4)$	$y(4)$
4	...	...	$x(\text{end})$	$y(\text{end})$

**Table A.11.2:** Descriptions of the commands for writing a fabrication program to use on the upright microscope. All  $x$ ,  $y$ , and  $z$  coordinates are in  $\mu\text{m}$ .

#### A.12 Teflon coating glass slides or PDMS molds

The two methods of applying an anti-stick coating to a MAP fabricated master structure that are commonly employed are solution coating, which aims to create a covalent bond between unreacted acrylate molecules on the surface of the master structure, and vacuum coating, which deposits a layer of anti-stick coating on the entire surface of the master structure by placing it in a desiccator with a small volume ( $< 1$  mL) of a silane solution and evacuating the desiccator. The procedures for each of these methods are outlined below. Figure A.12.1 shows SEM images of master structures that were molded after a deposition time greater than 45 minutes was employed (step 6). If too much anti-stick coating is deposited, the curing process of the PDMS is inhibited.

### Solution anti-stick coating

1. Make an acrylate replica or master structure. This method works best on acrylate replicas cured for 40 seconds under a UV lamp.
2. Place the structure in a 30 mL beaker of 20% ethylene diamine in ethanol for 30 minutes while stirring.
3. Rinse the structure in a 30 mL beaker of ethanol for 1 minute.
4. Combine the following in a 30 mL beaker:
  - a. 4.5 g hexafluorobenzene
  - b. 0.03 g perfluorooctadecanoic acid
  - c. 1 drop of methanol
  - d. 16 mL of ethanol
5. Stir the structure in the solution from 4 for 1.5 hours.
6. Rinse the structure in a 30 mL beaker of ethanol for 1 minute.

### Desiccator anti-stick coating

1. Bake the MAP fabricated master structure at 95 °C for ~15 minutes, and allow it to cool.
2. Add 1 to 2 mL of dimethylchlorosilane to a watch glass using a glass pipette.
3. Place the watch glass and master structure in a vacuum desiccator and turn on the vacuum. Let the chamber evacuate for ~10 minutes.
4. Close the vacuum valve and leave the contents under vacuum for 30-45 minutes.\*
5. The master structure is ready to be molded with PDMS.

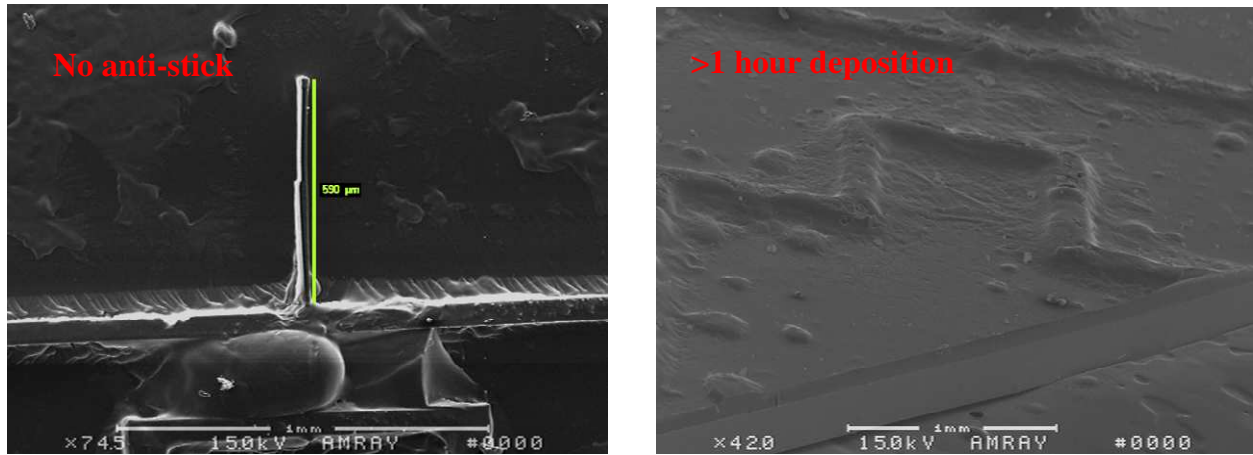


**Figure A.12.1:** SEM images of master structures after molding with no anti-stick coating (left) and after over-deposition of anti-stick coating (left). Without anti-stick coating, the PDMS is not completely removed from the acrylate structure, and is more likely to get stuck between channels. With too much anti-stick, the master structure remains sticky and the PDMS does not cure close to the surface, even after a 24 hour PDMS cure time.

## A.13 Elliptical block LabView program

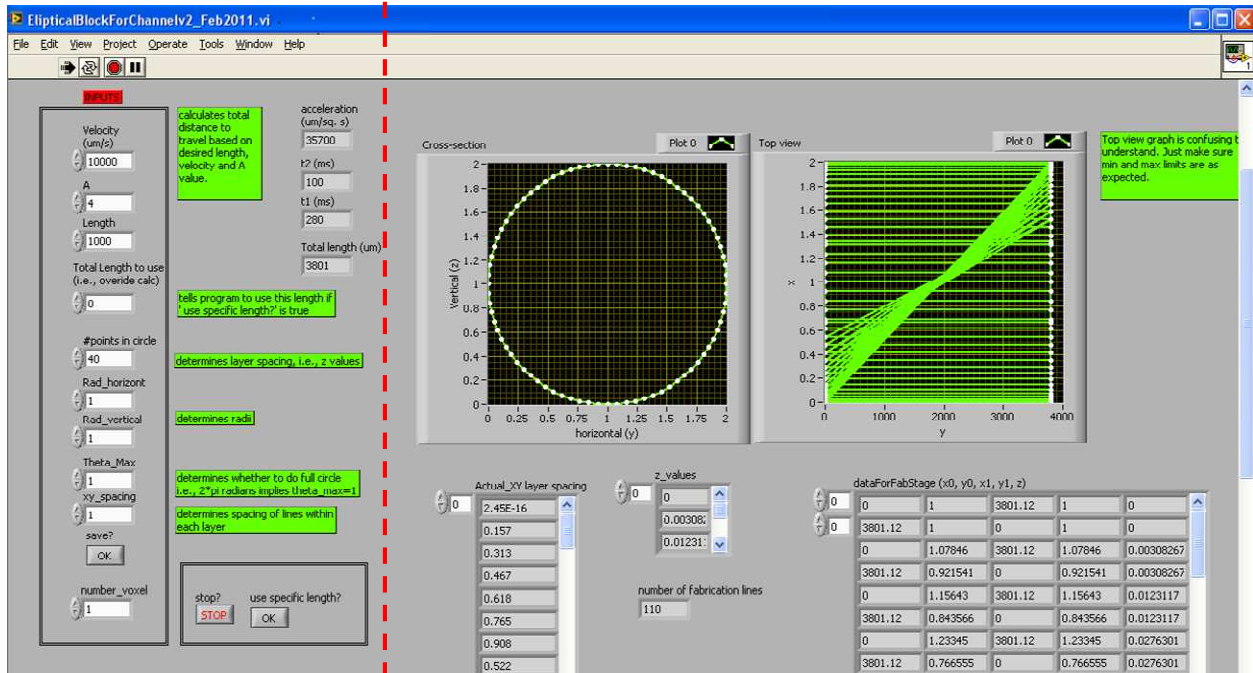


**Figure A.13.1:** Figures A.13.2 and A.13.3 are parts of this image. The front panel of the elliptical block program has been cut so that text can be more easily read. In A.13.2 and A.13.3 clarifications for parts of the front panel are given.

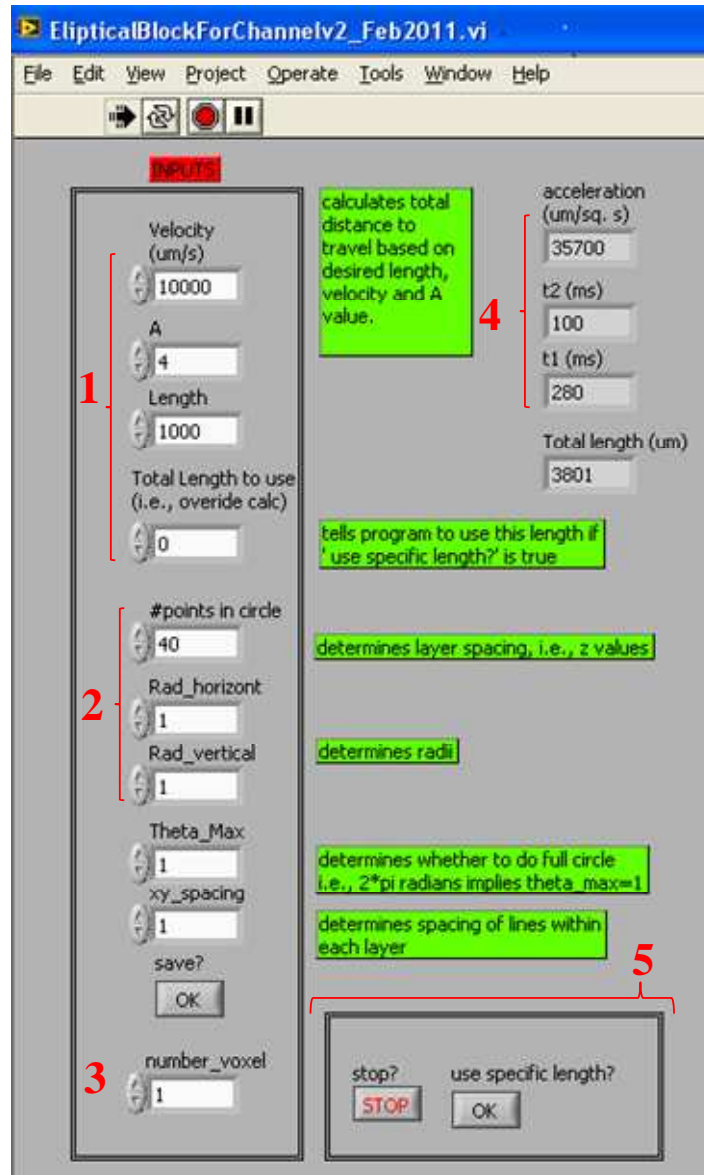


**Figure A.13.2:** The left half of the front panel of the elliptical block program. The input values are described in green text boxes where necessary. 1: The first two values are input here as they are on the front panel of the upright microscope program. The length and override length allow the program to incorporate acceleration time based on pre-determined values, or ignore acceleration time respectively. 2: These values are the most important for creating a program to fabricate a circular channel. In general, “Rad\_horizont” should be twice “Rad\_vertical” to take the voxel dimensions into consideration. 3: the number of voxels per point of fabrication. 4: These values are relevant if override length is not used. 5: “Stop” will save the program as a text file and “use specific length” uses the override length input in 1.

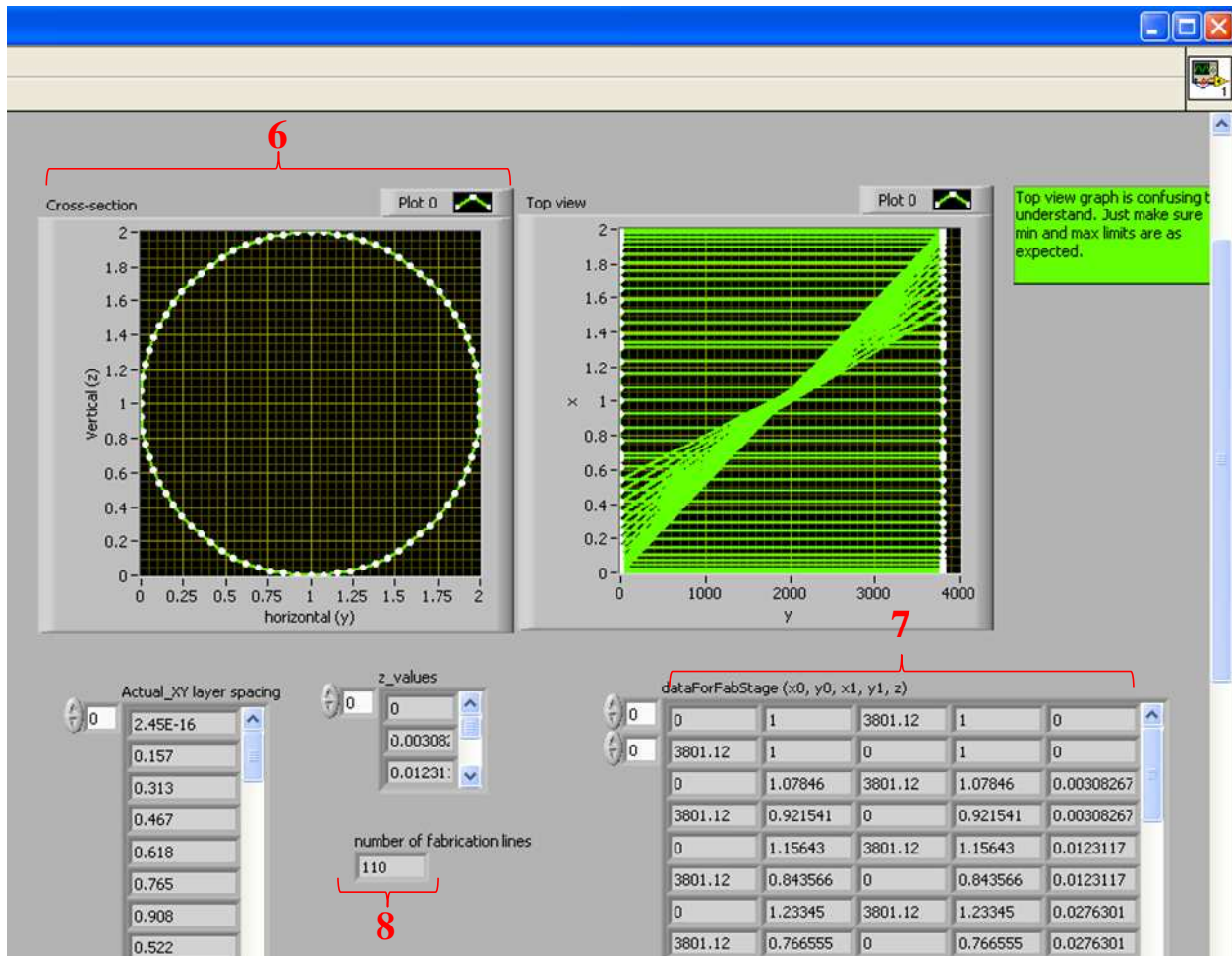


**Figure A.13.3:** The right half of Figure A.13.1. 6: this plot shows the dimensions of the calculated circle, and does not necessarily reflect exactly what the fabricated cross-section will look like. 7: The type of text file that is saved. This can be adjusted in the block diagram depending on which program is used to fabricate (ie. inverted microscope or upright microscope). 8: The total number of lines in the fabrication program. This value is in position 1-D1 in Table A.11.2.

## References

- (1) Whitesides, G. M. *Nature* **2006**, *442*, 368-373.
- (2) Roman, G. T.; Kennedy, R. T. *Journal of Chromatography A* **2007**, *1168*, 170-188.
- (3) Lin, C. C.; Tseng, C. C.; Chuang, T. K.; Lee, D. S.; Lee, G. B. *Analyst* **2011**, *136*, 2669-2688.
- (4) Kim, S.; Kim, H. J.; Jeon, N. L. *Integrative Biology* **2010**, *2*, 584-603.
- (5) Rosenfeld, L.; Lin, T.; Derda, R.; Tang, S. K. Y. *Microfluidics and Nanofluidics* **2014**, *16*, 921-939.
- (6) Bayraktar, T.; Pidugu, S. B. *International Journal of Heat and Mass Transfer* **2006**, *49*, 815-824.
- (7) Hetsroni, G.; Mosyak, A.; Pogrebnyak, E.; Yarín, L. P. *International Journal of Heat and Mass Transfer* **2005**, *48*, 1982-1998.
- (8) Wang, H. Z.; Iovenitti, P.; Harvey, E.; Masood, S. *Smart Materials & Structures* **2002**, *11*, 662-667.
- (9) Niu, X. Z.; Lee, Y. K. *Journal of Micromechanics and Microengineering* **2003**, *13*, 454-462.
- (10) Hsiao, K. Y.; Wu, C. Y.; Huang, Y. T. *Chemical Engineering Journal* **2014**, *235*, 27-36.
- (11) Weibel, D. B.; Kruithof, M.; Potenta, S.; Sia, S. K.; Lee, A.; Whitesides, G. M. *Analytical Chemistry* **2005**, *77*, 4726-4733.
- (12) Koplik, J.; Banavar, J. R.; Willemsen, J. F. *Physical Review Letters* **1988**, *60*, 1282-1285.
- (13) Bodoia, J. R.; Osterle, J. F. *Applied Scientific Research* **1961**, *10*, 265-276.
- (14) Dolnik, V.; Liu, S. R.; Jovanovich, S. *Electrophoresis* **2000**, *21*, 41-54.
- (15) Woolley, A. T.; Mathies, R. A. *Analytical Chemistry* **1995**, *67*, 3676-3680.
- (16) Xu, B.; Feng, X. J.; Xu, Y. Z.; Du, W.; Luo, Q. M.; Liu, B. F. *Analytical and Bioanalytical Chemistry* **2009**, *394*, 1911-1917.

- (17) Timerbaev, A. R. *Electrophoresis* **2010**, *31*, 192-204.
- (18) Pumera, M. *Chemical Communications* **2011**, *47*, 5671-5680.
- (19) Tegenfeldt, J. O.; Prinz, C.; Cao, H.; Huang, R. L.; Austin, R. H.; Chou, S. Y.; Cox, E. C.; Sturm, J. C. *Analytical and Bioanalytical Chemistry* **2004**, *378*, 1678-1692.
- (20) Shackman, J. G.; Munson, M. S.; Ross, D. *Analytical Chemistry* **2007**, *79*, 565-571.
- (21) Ross, D.; Kralj, J. G. *Analytical Chemistry* **2008**, *80*, 9467-9474.
- (22) Ross, D.; Romantseva, E. F. *Analytical Chemistry* **2009**, *81*, 7326-7335.
- (23) Strychalski, E. A.; Henry, A. C.; Ross, D. *Analytical Chemistry* **2009**, *81*, 10201-10207.
- (24) Strychalski, E. A.; Henry, A. C.; Ross, D. *Analytical Chemistry* **2011**, *83*, 6316-6322.
- (25) Flanigan, P. M.; Ross, D.; Shackman, J. G. *Electrophoresis* **2010**, *31*, 3466-3474.
- (26) Sikorsky, A. A.; Fourkas, J. T.; Ross, D. *Analytical Chemistry* **2014**, *86*, 3625-3632.
- (27) Geiger, M.; Hogerton, A. L.; Bowser, M. T. *Analytical Chemistry* **2012**, *84*, 577-596.
- (28) Breadmore, M. C.; Thabano, J. R. E.; Dawod, M.; Kazarian, A. A.; Quirino, J. P.; Guijt, R. M. *Electrophoresis* **2009**, *30*, 230-248.
- (29) Breadmore, M. C.; Dawod, M.; Quirino, J. P. *Electrophoresis* **2011**, *32*, 127-148.
- (30) Wen, Y. Y.; Li, J. H.; Ma, J. P.; Chen, L. X. *Electrophoresis* **2012**, *33*, 2933-2952.
- (31) Mala, Z.; Gebauer, P.; Bocek, P. *Electrophoresis* **2011**, *32*, 116-126.
- (32) Beckers, J. L.; Bocek, P. *Electrophoresis* **2000**, *21*, 2747-2767.
- (33) Breadmore, M. C.; Shallan, A. I.; Rabanes, H. R.; Gstoettenmayr, D.; Keyon, A. S. A.; Gaspar, A.; Dawod, M.; Quirino, J. P. *Electrophoresis* **2013**, *34*, 29-54.
- (34) Breadmore, M. C. *Electrophoresis* **2007**, *28*, 254-281.

- (35) Burgi, D. S.; Chien, R. L. *Analytical Chemistry* **1991**, *63*, 2042-2047.
- (36) Almeda, S.; Arce, L.; Valcarcel, M. *Electrophoresis* **2008**, *29*, 3074-3080.
- (37) Kim, J.; Chun, M. S.; Choi, K.; Chung, D. S. *Electrophoresis* **2009**, *30*, 1046-1051.
- (38) Blanco, E.; Casais, M. D.; Mejuto, M. D.; Cela, R. *Analytica Chimica Acta* **2009**, *647*, 104-111.
- (39) Zhang, C. X.; Thormann, W. *Analytical Chemistry* **1996**, *68*, 2523-2532.
- (40) Sommer, G. J.; Hatch, A. V. *Electrophoresis* **2009**, *30*, 742-757.
- (41) Shimura, K. *Electrophoresis* **2009**, *30*, 11-28.
- (42) Meighan, M. M.; Staton, S. J. R.; Hayes, M. A. *Electrophoresis* **2009**, *30*, 852-865.
- (43) Shackman, J. G.; Ross, D. *Electrophoresis* **2007**, *28*, 556-571.
- (44) Ivory, C. F. *Separation Science and Technology* **2000**, *35*, 1777-1793.
- (45) Wang, Q. G.; Tolley, H. D.; LeFebvre, D. A.; Lee, M. L. *Analytical and Bioanalytical Chemistry* **2002**, *373*, 125-135.
- (46) Kelly, R. T.; Woolley, A. T. *Journal of Separation Science* **2005**, *28*, 1985-1993.
- (47) Chacron, M. J.; Slater, G. W. *Physical Review E* **1997**, *56*, 3446-3450.
- (48) Frumin, L. L.; Peltek, S. E.; Zilberstein, G. V. *Physical Review E* **2001**, *64*, 1-5.
- (49) Pel, J.; Broemeling, D.; Mai, L.; Poon, H. L.; Tropini, G.; Warren, R. L.; Holt, R. A.; Marziali, A. *Proceedings of the National Academy of Sciences of the United States of America* **2009**, *106*, 14796-14801.
- (50) Righetti, P. G.; Bossi, A. *Journal of Chromatography B* **1997**, *699*, 77-89.
- (51) Righetti, P. G. *Electrophoresis* **2006**, *27*, 923-938.
- (52) Harrison, D. J.; Manz, A.; Fan, Z. H.; Ludi, H.; Widmer, H. M. *Analytical Chemistry* **1992**, *64*, 1926-1932.
- (53) Ryzolova, M.; Preisler, J.; Brabazon, D.; Macka, M. *Trends in Analytical Chemistry* **2010**, *29*, 339-353.

- (54) Felhofer, J. L.; Blanes, L.; Garcia, C. D. *Electrophoresis* **2010**, *31*, 2469-2486.
- (55) Huang, X. H. C.; Quesada, M. A.; Mathies, R. A. *Analytical Chemistry* **1992**, *64*, 967-972.
- (56) Huang, X. H. C.; Quesada, M. A.; Mathies, R. A. *Analytical Chemistry* **1992**, *64*, 2149-2154.
- (57) Mathies, R. A.; Huang, X. C. *Nature* **1992**, *359*, 167-169.
- (58) Savitzky, A.; Golay, M. J. E. *Analytical Chemistry* **1964**, *36*, 1627-1639.
- (59) Kuban, P.; Nguyen, H. T. A.; Macka, M.; Haddad, P. R.; Hauser, P. C. *Electroanalysis* **2007**, *19*, 2059-2065.
- (60) Nguyen, H. T. A.; Kuban, P.; Pham, V. H.; Hauser, P. C. *Electrophoresis* **2007**, *28*, 3500-3506.
- (61) Mudhoo, A.; Sharma, S. K.; Garg, V. K.; Tseng, C. H. *Critical Reviews in Environmental Science and Technology* **2011**, *41*, 435-519.
- (62) Munson, M. S.; Danger, G.; Shackman, J. G.; Ross, D. *Analytical Chemistry* **2007**, *79*, 6201-6207.
- (63) Meighan, M. M.; Vasquez, J.; Dziubcynski, L.; Hews, S.; Hayes, M. A. *Analytical Chemistry* **2011**, *83*, 368-373.
- (64) Meighan, M. M.; Keebaugh, M. W.; Quihuis, A. M.; Kenyon, S. M.; Hayes, M. A. *Electrophoresis* **2009**, *30*, 3786-3792.
- (65) Greenlee, R. D.; Ivory, C. F. *Biotechnology Progress* **1998**, *14*, 300-309.
- (66) Kennedy, C. D. *Biochemical Education* **1990**, *18*, 35-40.
- (67) Ross, D.; Locascio, L. E. *Analytical Chemistry* **2002**, *74*, 2556-2564.
- (68) Jovin, T. M. *Annals of the New York Academy of Sciences* **1973**, *209*, 477-496.
- (69) Li, L. J.; Fourkas, J. T. *Materials Today* **2007**, *10*, 30-37.
- (70) LaFratta, C. N.; Fourkas, J. T.; Baldacchini, T.; Farrer, R. A. *Angewandte Chemie-International Edition* **2007**, *46*, 6238-6258.
- (71) Kim, Y.; Salhany, J. *Spectroscopy* **2011**, *26*, 24-29.

- (72) Supatto, W.; Truong, T. V.; Debarre, D.; Beaurepaire, E. *Current Opinion in Genetics & Development* **2011**, *21*, 538-548.
- (73) Kumi, G.; Yanez, C. O.; Belfield, K. D.; Fourkas, J. T. *Lab on a Chip* **2010**, *10*, 1057-1060.
- (74) LaFratta, C. N.; Baldacchini, T.; Farrer, R. A.; Fourkas, J. T.; Teich, M. C.; Saleh, B. E. A.; Naughton, M. J. *Journal of Physical Chemistry B* **2004**, *108*, 11256-11258.
- (75) LaFratta, C. N.; Li, L. J.; Fourkas, J. T. *Proceedings of the National Academy of Sciences of the United States of America* **2006**, *103*, 8589-8594.
- (76) Maruo, S.; Nakamura, O.; Kawata, S. *Optics Letters* **1997**, *22*, 132-134.
- (77) Dawood, F.; Qin, S. J.; Li, L. J.; Lin, E. Y.; Fourkas, J. T. *Chemical Science* **2012**, *3*, 2449-2456.
- (78) Mendonca, C. R.; Correa, D. S.; Baldacchini, T.; Tayalia, P.; Mazur, E. *Applied Physics Materials Science & Processing* **2008**, *90*, 633-636.
- (79) Sun, X. H.; Yan, J. L.; Yang, X. R.; Wang, E. K. *Electrophoresis* **2004**, *25*, 3455-3460.
- (80) Li, J. X.; Zhang, M. Y.; Wang, L. M.; Li, W. H.; Sheng, P.; Wen, W. J. *Microfluidics and Nanofluidics* **2011**, *10*, 919-925.
- (81) Brun, M.; Chateaux, J. F.; Deman, A. L.; Pittet, P.; Ferrigno, R. *Electroanalysis* **2011**, *23*, 321-324.